

**RAPID, RELIABLE TISSUE FRACTIONATION ALGORITHM
FOR COMMERCIAL SCALE BIOREFINERIES**

by

Rahul Reddy Kancharla



A dissertation
submitted in partial fulfillment
of the requirements for the degree of
Doctor of Philosophy in Electrical and Computer Engineering
Boise State University

May 2022

© 2022

Rahul Reddy Kancharla

ALL RIGHTS RESERVED

BOISE STATE UNIVERSITY GRADUATE COLLEGE

DEFENSE COMMITTEE AND FINAL READING APPROVALS

of the dissertation submitted by

Rahul Reddy Kancharla

Dissertation Title: RAPID, RELIABLE TISSUE FRACTIONATION ALGORITHM FOR COMMERCIAL SCALE BIOREFINERIES

Date of Final Oral Examination: 11 November 2021

The following individuals read and discussed the dissertation submitted by student Rahul Reddy Kancharla, and they evaluated the presentation and response to questions during the final oral examination. They found that the student passed the final oral examination.

Dr. Elisa H. Barney Smith, Ph.D	Chair, Supervisory Committee
William A. Smith	Member, Supervisory Committee
Dr. Joshua J. Kane, Ph.D	Member, Supervisory Committee
Dr. Jennifer Smith, Ph.D	Member, Supervisory Committee
Dr. Nader Rafla, Ph.D	Member, Supervisory Committee
Dr. Bryon Donohoe, Ph.D	(External) Member, Supervisory Committee

The final reading approval of the dissertation was granted by Dr. Elisa H. Barney Smith, Ph.D, Chair of the Supervisory Committee. The dissertation was approved by the Graduate College.

ACKNOWLEDGEMENTS

Earning a doctorate is a long and arduous process - it certainly cannot be achieved by a single person without the support of many people. First and foremost, I'd like to express my sincerest gratitude to my mentor and guide, Dr. Elisa H. Barney Smith, for her immense cooperation through my doctoral program. Without her timely advice, motivation, and immense knowledge I would have never accomplished this task.

I'd also like to express my sincerest gratitude to my other mentors and my committee members William A. Smith and Dr. Joshua J. Kane from Idaho National Laboratory, for being patient with me and providing knowledgeable advice through my doctoral program. I'd also like to thank my other committee members Dr. Nader Rafla, Dr. Jennifer Anne Smith, and the Department of Electrical and Computer Engineering at Boise State University for all their support and encouragement. Lastly, I'd like to express my deep sense of thanks to my friend Kennedy Courtney who has been my first reviewer while writing this dissertation.

This research was supported by the United States Department of Energy (DOE), Office of Energy Efficiency and Renewable Energy (EERE), and Bioenergy Technologies Office (BETO), under Award No. DE-AC07-05ID14517. The views expressed in the article do not necessarily represent the views of the United States Department of Energy or the United States Government.

ABSTRACT

Increasing demand, limited supply, and the impact on the environment raise significant concerns about the consumption of fossil fuels. Because of this, global economies are facing two significant energy challenges: i) securing the supply of reliable and affordable energy and ii) achieving the transformation to a low-carbon, high-efficiency, and sustainable energy system. Recently, there has been growing interest in developing portable transportation fuels from biomass in order to reduce the petroleum consumption in the transportation sector - a major contributor to greenhouse gas emission. A cost-effective conversion process to produce biofuels from lignocellulosic biomass material relies not just on the material quality, but also on the biorefinery's ability to measure the quality of the source biomass. The quality of the feedstock is crucial for a commercially viable conversion platform. This research mainly focuses on developing sensing techniques using 3D X-ray imaging to study quality factors like material composition, ash content and moisture content which affect the conversion efficiency, equipment wear, and product yield in the bioethanol production in a real-time or near real-time basis.

TABLE OF CONTENTS

ACKNOWLEDGEMENTS	iv
ABSTRACT	v
LIST OF TABLES	xi
LIST OF FIGURES	xiii
LIST OF ABBREVIATIONS	xxii
1 Introduction and Motivation	1
1.1 Aim of the Dissertation	5
1.2 Dissertation Organization	6
2 Anatomical Tissue Characterization in Corn Stover Bales with Computed Tomography	10
2.1 Corn Stover as a Feedstock to the Biorefinery	10
2.1.1 Characteristics of Corn Stover Biomass	11

2.1.2	Literature review on biomass compositional analysis	15
2.2	Background on X-ray Tomography or Computed Tomography	17
2.3	Discussion	22
3	Quantitative Comparison of 3D Skeletonization Algorithms	23
3.1	Skeletonization Algorithms	24
3.1.1	Fundamentals on Skeletonization	24
3.1.2	Morphological Thinning Implementation	27
3.1.3	Euclidean Distance Transform based Implementation	28
3.2	Degradation Models	29
3.2.1	Surface Roughness	30
3.2.2	Surface Protuberances	31
3.3	Comparative Analysis Metrics	32
3.4	Experiments & Results	34
3.5	Discussion	37
4	Anatomical Tissue Characterization in Corn Stover Bales with 3D Image Analysis Techniques	47

4.1	Pre-processing	49
4.2	Detection and Volume Estimation of Ash Content	51
4.3	Detection and Volume Estimation of Corn Cobs	53
4.3.1	Results	55
4.4	Discussion	56
5	The Sparse View Image Reconstruction Problem	59
5.1	Evaluation of Image Reconstruction Methods	63
5.1.1	Analytical Reconstruction Methods	63
5.1.2	Iterative Reconstruction Methods	64
5.2	Two-Projection Method	71
5.3	Computation Times	80
5.4	Discussion	82
6	Numerical Evaluation of Tissue characterization in a Corn Stover Bale with 3D Image Analysis Techniques in a Sparse View Framework	85
6.1	Detection of Rocks and Metal Contaminants in a Corn Stover Bale	86
6.2	Detection of Soil Clumps in a Corn Stover Bale	91

6.3	Detection of various Corn Stover Fractions	93
6.4	Discussion	95
7	Assessing the Framework for X-ray Tomography at a Commercial Scale Biorefinery	98
7.1	Beer-Lambert's Law and X-ray Photon Absorption Parameter Esti- mation	100
7.1.1	Beer-Lambert's Law	100
7.1.2	Bulk Density	101
7.1.3	Linear Attenuation	103
7.2	Bulk Density Behavior with Moisture and Soil Content	105
7.3	Linear Attenuation Behavior with Moisture and Soil Content	107
7.4	Integration of X-ray Tomography into the Feedstock Supply Chain of the Biorefinery	108
7.4.1	Scanning the Truck Load	111
7.4.2	Scanning a Single Bale	114
7.5	Discussion	117
8	Conclusion and Future Directions	120

REFERENCES 127

LIST OF TABLES

4.1	Volume of rocks extracted from the test bale	52
4.2	Volume of soil clumps extracted from the test bale	53
4.3	Volume of corn cobs extracted from the test bales	56
5.1	Reconstructed images based on iterative reconstruction methods using 71 projections	67
5.2	Reconstructed images based on iterative reconstruction methods using 11 projections	68
5.3	Reconstructed images based on iterative reconstruction methods using 2 projections	69
5.4	Quantitative analysis with simple phantom with angle separation 90-degree	75
5.5	Offset factor at each angular separation	80
5.6	Quantitative analysis with simple phantom with volume: 148672 voxels	81
6.1	Quantitative analysis with synthetic smooth pebble data	89

6.2	Quantitative analysis with synthetic rough gravel data	90
6.3	Quantitative analysis with a real rock sample	90
6.4	Quantitative analysis with clumped soil sample covering 0.32% of the total volume	92
7.1	Elemental mass composition of corn stover	104
7.2	Elemental mass composition of moisture content	104
7.3	Elemental mass composition of soil content	105

LIST OF FIGURES

1.1	Greenhouse gas emissions from the transportation sector between 1990-2019 [4].	3
2.1	Amounts of (a) Glucan and (b) Xylan recovered with various pre-treatment methods for each corn stover fraction [22]	12
2.2	A bar rake being used to create a corn stover windrow [23].	13
2.3	(a) Square bale dropped off from the end of a baler, (b) Round corn stover bales in the field [23].	14
2.4	Principles of photon-matter interaction. (a) No interaction, (b) Photoelectric absorption, (c) Compton scattering and (d) Rayleigh scattering [42].	19
2.5	Geometry of CBCT [43]	22
3.1	(a) The MAT skeleton M of the shape O with contour S , (b) Examples of maximally inscribed circles (red), a medial atom (X, r) , and circles which are neither maximal nor inscribed, thus not contributing to M (green), (c) Approximate reconstruction of O by the union of circles [47].	25

3.2	(a) 2D skeleton example, (b) 3D Surface skeleton example, (c) 3D curve skeleton example [47].	27
3.3	(a) Original image, (b) Partially thinned image, (c) completely thinned image	28
3.4	(a) Original image, (b) Euclidean Distance Map, (c) Skeleton extracted using SSM	29
3.5	Spurious branch generated in the presence of surface noise.	30
3.6	A cylinder phantom used in the experiments.	30
3.7	A section of the (a) phantom cylinder, (b) surface with Gaussian noise after thresholding, (c) surface after morphological closing operation.	31
3.8	A section of the (a) cylinder phantom, cylinder phantoms with protuberances of diameter of (b) 8 voxels, (c) 10 voxels, and (d) 14 voxels.	32
3.9	Evaluation of morphological thinning based skeletonization method with surface roughness degradation model. Box and whisker plot showing the (a) average deviation, (b) missing/added nodes, and (c) spurious branches.	39
3.10	Evaluation of distance field based skeletonization method with surface roughness degradation model. Box and whisker plot showing the (a) average deviation, (b) missing/added nodes, and (c) spurious branches.	40

3.11	Evaluation of morphological thinning based skeletonization method with protuberances of diameter 8 voxels. Box and whisker plot showing the (a) average deviation, (b) missing/added nodes, and (c) spurious branches.	41
3.12	Evaluation of morphological thinning based skeletonization method with protuberances of diameter 10 voxels. Box and whisker plot showing the (a) average deviation, (b) missing/added nodes, and (c) spurious branches.	42
3.13	Evaluation of morphological thinning based skeletonization method with protuberances of diameter 14 voxels. Box and whisker plot showing the (a) average deviation, (b) missing/added nodes, and (c) spurious branches.	43
3.14	Evaluation of distance field based skeletonization method with protuberances of diameter 8 voxels. Box and whisker plot showing the (a) average deviation, (b) missing/added nodes, and (c) spurious branches.	44
3.15	Evaluation of distance field based skeletonization method with protuberances of diameter 10 voxels. Box and whisker plot showing the (a) average deviation, (b) missing/added nodes, and (c) spurious branches.	45

3.16	Evaluation of distance field based skeletonization method with protruberances of diameter 14 voxels. Box and whisker plot showing the (a) average deviation, (b) missing/added nodes, and (c) spurious branches.	46
4.1	CT setup used to extract the radiographs of corn stover bale with (a) detector (b) mini-round corn stover bale (c) X-ray Source.	48
4.2	Work flow diagram representing the different stages of the tissue characterization in a corn stover bale.	49
4.3	Example (a) raw 2D reconstructed slice, (b) reconstructed slice after thresholding, (c) reconstructed slice after preprocessing.....	50
4.4	3D reconstruction using (a) raw 2D reconstructed slices, (b) reconstructed slices after thresholding, (c) reconstructed slices after preprocessing.	51
4.5	(a) 2D image of X-ray reconstructed data with rocks highlighted with red circle and soil clumps are highlighted with blue circle, and (b) histogram showing the intensity distribution of the 2D image.	52
4.6	3D reconstruction of the bale with (a) rocks, (b) soil clumps where contaminants are shown in alternate colors.	53
4.7	Example (a) corn cob, (b) skeleton of the corn cob represented with graphs, (c) cyclic loop extracted from the graph.	54

4.8	2D cross-sectional image of cyclic loop with arrows pointing the two distances which we measure	56
4.9	A corn cob with the plane at its initial position and planes at the ends of the cob where the intersectional radius decreased by more than 10%.	57
4.10	(a) baleset # 1, (b) corn cobs extracted from baleset #1, (c) baleset # 2 (d) corn cobs extracted from baleset #2. Note that one of the three cobs at the bottom of (b) has lost much of its material.	58
5.1	Schematic illustration of data acquisition in (a) conventional CT framework and (b) sparse view CT framework.	60
5.2	(a) Phantom used for the evaluation, (b) A 2D phantom used for qualitative analysis.	61
5.3	Geometry of CBCT [43]	62
5.4	(a) A 2D phantom. 2D phantom reconstruction with FDK using (b) 359 projections, (c) 274 projections, (d) 179 projections, (e) 89 projections, (f) 71 projections, (g) 23 projections, (h) 11 projections, (i) 3 projections.	64
5.5	(a) Pearson correlation coefficient, (b) computation time in seconds versus number of projections for the FDK algorithm.	65

5.6	(a) Pearson correlation coefficient, (b) computation time in seconds versus number of iterations for OS-SART, SART-TV, CGLS, MLEM algorithms using 71 projections.	71
5.7	(a) Pearson correlation coefficient, (b) computation time in seconds versus number of iterations for OS-SART, SART-TV, CGLS, MLEM algorithms using 11 projections.	71
5.8	(a) Pearson correlation coefficient, (b) computation time in seconds versus number of iterations for OS-SART, SART-TV, CGLS, MLEM algorithms using 2 projections.	72
5.9	Architecture of the two-projection method. (a) The phantom represented in 3D volume, (b) the 2D X-ray projections taken at two tomographic angles, (c) the extrapolated volume for each projection back in 3D, (d) the aligned extrapolated volumes, (e) the intersection of the two aligned volumes.	73
5.10	(a) 2D cross-section slice from the rock phantom, (b) Estimated 2D cross-section slice from the rock phantom with 90-degree separation. .	75
5.11	Reconstructed square encloses the object circle.	76
5.12	(a) 2D Phantom. Projections with (b) 15 degree, (c) 30 degree, (d) 45 degree, (e) 60 degree, (f) 90 degree, and (f) 135 degree separation.	78
5.13	Circle inscribed in a rhombus.	79
5.14	Fan beam X-ray acquisition geometry.	79

5.15	Reconstructed volume of a sphere with 15 degree separation without proper padding.	81
5.16	Time complexity with increase in input dimensions for OS-SART, CGLS, MLEM & the proposed two projection method.	82
6.1	An X-ray projection through a corn stover bale showing the four rocks (a) before thresholding, and (b) after thresholding.	87
6.2	Architecture of the rocks and metal contamination detection in a sparse view framework using two-projection method where (a) shows the synthetic rock sample represented in 3D volume with red color, (b) shows the 2D X-ray projections taken at two tomographic angles, (c) shows the rocks segmented using thresholding, (d) shows the volume extrapolated into 3D, (e) shows the aligned extrapolated volumes, (f) shows the intersection of the two aligned volumes.	88
6.3	(a) Smooth pebble rock sample and (b) Rough gravel rock sample . . .	89
6.4	A 3D corn stover bale volume with rocks represented with a color red.	91
6.5	A 3D corn stover bale volume with soil clumps represented with orange color.	92
6.6	MLEM based reconstruction using 3 projections with (a) 5 iterations, (b) 10 iterations, (c) 30 iterations, and (d) 100 iterations, and reconstruction using 5 projections with (e) 5 iterations, (f) 10 iterations, (g) 30 iterations, and (h) 100 iterations.	94

6.7	A 3D volume of upper and lower stalks after corn cob and stalk node extraction.	95
6.8	A 3D volume of leaves and husks appear as isolated voxels.	96
6.9	A 3D volume representation of a corn stover bale with brown color representing cobs and stalk nodes, green color for upper stalks and lower stalks, and red color represents the leaves and husks.	97
7.1	A 2D surface plot showing the change in bulk density of a bale with respect to change in moisture content and soil content. Higher quantities of soil & moisture increases the bulk density.	106
7.2	Variation of bulk density with (a) soil content, (b) moisture content. . .	107
7.3	Linear attenuation coefficient with 15% moisture content and soil contents 5%, 10%, 15% and 20% versus peak voltage.	109
7.4	Linear attenuation coefficient with 25% moisture content and soil contents 5%, 10%, 15% and 20% versus peak voltage.	110
7.5	Linear attenuation coefficient with 35% moisture content and soil contents 5%, 10%, 15% and 20% versus peak voltage.	111
7.6	Advanced feedstock supply chain at a biorefinery [68]. At stages 4 and 12 (circled) techniques developed in this work can be applied. . .	112

7.7	Fractional X-ray transmission (I/I_0) with 15% moisture content and soil contents 5%, 10%, 15% and 20% with 6ft thickness of the material versus peak voltage.	113
7.8	Fractional X-ray transmission (I/I_0) with 25% moisture content and soil contents 5%, 10%, 15% and 20% with 6ft thickness of the material versus peak voltage.	114
7.9	Fractional X-ray transmission (I/I_0) with 35% moisture content and soil contents 5%, 10%, 15% and 20% with 6ft thickness of the material versus peak voltage.	115
7.10	Fractional X-ray transmission (I/I_0) with 15% moisture content and soil contents 5%, 10%, 15% and 20% with 3ft thickness of the material versus peak voltage.	116
7.11	Fractional X-ray transmission (I/I_0) with 25% moisture content and soil contents 5%, 10%, 15% and 20% with 3ft thickness of the material versus peak voltage.	117
7.12	Fractional X-ray transmission (I/I_0) with 35% moisture content and soil contents 5%, 10%, 15% and 20% with 3ft thickness of the material versus peak voltage.	118

LIST OF ABBREVIATIONS

ABE – Acetone-Butanol-Ethanol

ANN – Artificial Neural Networks

BETO – Bioenergy Technologies Office

CBCT – Cone-Beam Computed Tomography

CGLS – Conjugate Least Squares

CT – Computed Tomography

CUDA – Compute Unified Device Architecture

EM – Electromagnetic

FBP – Filtered Back Projection

FDK – Feldkamp, Davis and Kress

FOV – Field Of View

FT-NIR – Fourier Transform Near Infrared

GDP – Gross Domestic Product

GE – Greenhouse Gas Emission

GHG – Greenhouse Gases

GPU – Graphics processing unit

GWP – Global Warming Potential

HFC – Hydro fluorocarbons

MAT – Medial Axis Transform

MC – Moisture Content

MLEM – Maximum Likelihood Expected Maximization

NIR – Near Infrared

NIST – National Institute of Standards and Technology

NREL – National Renewable Energy Laboratory

NSI – North Star Imaging

OS-SART – Ordered Subset - Simultaneous Algebraic Reconstruction

PLS – Partial Least Squares

SART-TV – Simultaneous Algebraic Reconstruction - Total Variation

SC – Soil Content

SSM – Skeleton Strength Map

RAM – Random Access Memory

TIGRE – Tomographic Iterative GPU-based Reconstruction

USDOE – United State Department of Energy

XAAMDI – X-Ray Attenuation and Absorption for Materials of Dosimetric Interest

CHAPTER 1

INTRODUCTION AND MOTIVATION

Concerns over the depletion of fossil fuels, energy security, and global climate change have prompted the development of sustainable renewable energy alternatives to fossil-based fuels. Currently, fossil fuels play a significant role in reaching daily energy demands like fueling our cars, growing our food, and heating our homes [1]. In the United States, fossil fuels account for 80% of the total energy consumption [2]. Among fossil fuel sources, petroleum is a significant contributor accounting for 35% of total energy consumption, followed by natural gas at 34% and coal at 10% [2].

Consumption of these fossil fuels releases the stored carbon and other greenhouse gases (GHG) into the atmosphere. The buildup of GHG's like carbon dioxide (CO_2), methane (CH_4), nitrous oxide (N_2O), and hydrofluorocarbons (HFCs) trap the heat and cause the Earth's atmosphere to warm, resulting in climate change [3]. Among the others, CO_2 is the primary GHG emitted through human activities. In 2019, CO_2 accounted for 80% of all U.S. GHG emissions from human activities. Though other GHG's like CH_4 and N_2O are more potent at warming the planet, their lifetime is shorter relative to CO_2 . Because of its long lifetime, CO_2 has long term detrimental effects, and researchers are fervently looking for fuel alternatives

to reduce carbon emissions.

Among human activities, transportation is the most significant contributor of GHG emissions, accounting for 35% of the total U.S. CO_2 emissions and 28% of total GHG emissions [4]. The majority of the fuel used in the transportation sector is petroleum-based (90%), which includes gasoline and diesel [4, 5]. Figure 1.1 shows the GHG emissions from the transportation sector between 1990-2019 in million metric tons of CO_2 equivalent. CO_2 equivalent is a metric measure used to compare the emissions from various GHGs based on global warming potential (GWP) by converting amounts of other gases to the equivalent amount of CO_2 with the same global warming potential. The figure shows that there has been a significant increase in GHG emissions since 1990. With the rapidly developing nations, it is estimated that the demand for petroleum will further increase by 50% by 2025 [6], which will result in higher emissions. With increasing demand, it is essential to diversify the energy sources in the transportation sector to reduce the dependency on petroleum.

Recently there has been a lot of interest in developing portable transportation fuels produced from biomass, known as “biofuels”. The biofuels present a promising and sustainable pathway to meet the fossil-based fuel demand in the transportation sector [7]. Biomass generally refers to any renewable organic matter that stores sunlight in the form of chemical energy, such as plants, agricultural residues, municipal wastes, and algae [7]. Since biomass’s combustion releases carbon dioxide that was captured through the photosynthesis process during its life cycle, biomass is considered a carbon-neutral energy source compared to fossil fuels created millions of years ago.

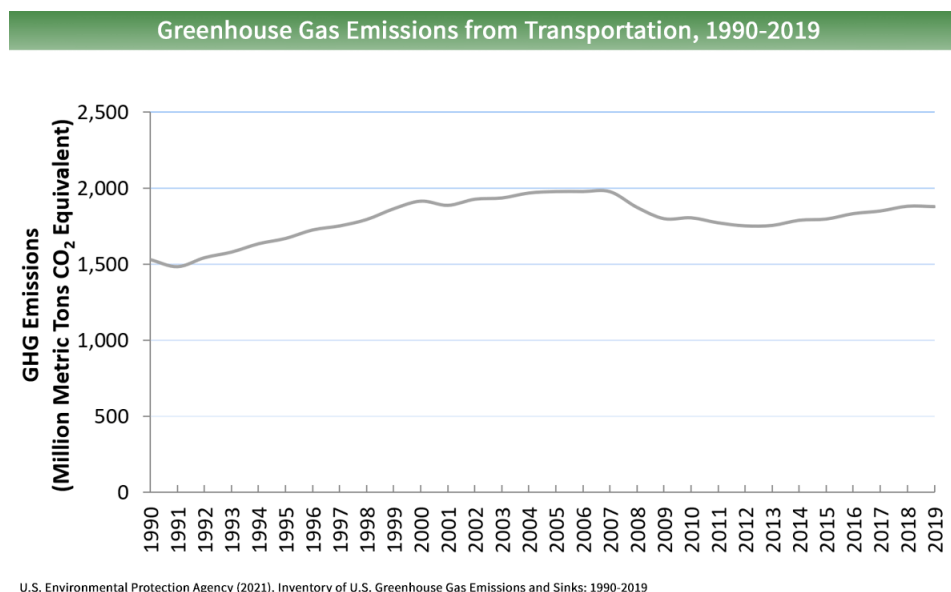


Figure 1.1: Greenhouse gas emissions from the transportation sector between 1990-2019 [4].

Currently, bioethanol and biodiesel dominate the global biofuel market. In 2020, 5% of the U.S. transportation sector demand was met by biofuels [8], where ethanol's share is about 4% and biodiesel accounted for 1% [8]. The biofuel output is expected to increase by 25% between 2019-24, to reach 190 billion L [9]. Currently, biofuels like bioethanol and biodiesel are widely used as blending agents with gasoline to increase the octane and cut down carbon monoxide and other smog-causing emissions [10]. Much work is going underway to increase the usage of "drop-in" fuels, fuels suitable for use at high blend shares (like biobutanol) or unblended without technical modifications to engines or fueling infrastructure.

Generally, biofuels like bioethanol or biobutanol are produced from biomass through a biochemical conversion process. The biochemical process typically relies on sugar fermentation, such as the ABE (Acetone-butanol-ethanol) process, which

uses bacteria such as *Clostridium acetobutylicum* to convert sugars into alcohols and ketones [10, 11]. Currently, the biofuels industry mainly utilizes sugar crops (sugarcane, sugarbeet), starch crops (corn, sorghum), and oil-seed crops (soybean, canola) for biofuel production. The main downside with these feedstocks is that they compete with food supply [12]. Over the past decade, the U.S. Department of Energy's Bioenergy Technologies Office (USDOE-BETO) focused on developing next-generation fuels based on non-food (terrestrial cellulosic and algae-based) resources [7]. The next-generation biofuels will primarily come from cellulose, found in the cell walls of stalks and wood, compared to the sugar found in food resources like corn. The billion-ton study [13] published by the Department of Energy states that the United States has a future potential of producing one billion tons of sustainable biomass, mainly composed of crop residues, wood residues, and energy crops annually without severe climate and food shortages.

These biomass materials (crop residues, wood residues, and energy crops) are inherently heterogeneous, have variable composition and conversion properties, and often contain soil, and other exogenous contaminants detrimental to the handling and conversion process [14, 15]. Most of the analytical techniques used to study biomass quality are destructive, sampling-intensive, and time-consuming. To ensure the sustainability of the biofuels, the biorefinery (a facility that integrates biomass conversion processes and equipment to produce fuels, power, and value-added chemicals from biomass) should be technologically equipped to rapidly and non-destructively analyze the incoming biomass and provide feedback that can be used to adapt processing conditions to meet the feedstock conditions.

1.1 Aim of the Dissertation

In this work, we focus on developing a sensing framework using 3D X-ray tomography to study the biomass feedstock quality. This work focuses on extracting information about the quality of corn stover bales. Since corn is one of the most abundant crops in the U.S., the infrastructure to collect the stover is readily available. Because of that, corn stover is one of the initial biomass sources adapted to produce cellulosic ethanol in the U.S. [16]. However, the harvest methods mainly focus on collecting the corn, and the corn stover is left in the field, sometimes for days, before being collected and stored. The entire process from harvesting to storage conditions adds many unwanted variables that need to be understood before converting to biofuels at the biorefinery. Chapter 2 provides a comprehensive report on these unwanted variables.

This dissertation tackles three main research problems:

1. Develop 3D segmentation tools to segment and estimate the volume of different anatomical fractions present in the lignocellulosic biomass, specifically corn stover, using 3D X-ray tomography.
2. Reconstruct a 3D volume image of corn stover bales with a limited number of X-ray projections.
3. Generalize the X-ray tomography's framework to be able to scale up to a commercial-scale biorefinery.

1.2 Dissertation Organization

The chapters in this dissertation are divided into three main topics: 3D segmentation techniques for tissue characterization (Chapters 2, 3, 4), tissue characterization in the sparse-view framework (Chapters 2, 5 and 6), and X-ray tomography framework at a commercial biorefinery (Chapter 7). Chapter 8 concludes the dissertation and proposes future work. The contents of each chapter are summarized as follows:

Chapter 2: Anatomical Tissue Characterization and Computed Tomography

This chapter provides a comprehensive report on the different tissue fractions in the corn stover bale. The conversion properties of different tissue fractions are discussed to show the importance of knowing the contents of a bale. The chapter also talks about the detrimental factors like moisture content, soil-derived ash content, rocks and metal contaminants present in the bale, and how they affect the conversion at a biorefinery. At the end, a detailed description of how X-ray imaging works and the technical background for computed tomography (CT) is discussed.

Chapter 3: Quantitative Comparison of 3D Skeletonization Algorithms

3D skeletons are widely used as shape descriptors with a broad spectrum of applications in shape matching, recognition, animation, retrieval, and compression [17]. Through decades of research, there is now a multitude of algorithms. However, quantitative comparison of different skeletonization algorithms is still

an open problem. This chapter discusses the two surface degradation models and three metrics designed to evaluate the performance of the 3D skeletonization algorithms.

Chapter 4: Anatomical Tissue Characterization of Corn Stover Bales using 3D Image Analysis

This chapter presents 3D segmentation strategies to segment and estimate the volumetric content information of the different tissue contents – rocks, soil clumps and cobs – present in a corn stover bale. This chapter shows the performance of a histogram directed thresholding technique to segment and estimate the volume of rocks and soil clumps present in a bale. In the second half of this chapter, 3D skeletons are used as shape descriptors to extract and segment the corn cobs present in a corn stover bale. The algorithms presented in this work rely only on 3D shape and texture information to extract the volume of corn cobs. The corn cob extraction work presented in this chapter formed the basis of the work published in "Anatomical Fraction Segmentation in the Biomass Bales" [18].

Chapter 5: The Sparse View Image Reconstruction Problem

This chapter explores the 3D image reconstruction problem using fewer X-ray projections than used in commercial CT technology. This chapter shows the performance of several analytical and iterative reconstruction methods that use fewer X-ray projections. This chapter also presents a simple and computationally less expensive two-projection method. The results with a simple phantom show that the two-projection method can be used for simple application tasks, where the application only requires detecting and estimating the volume without extracting

any complicated features about the target object.

Chapter 6: Numerical Evaluation of Tissue characterization in a Corn Stover Bale with 3D Image Analysis Techniques in a Sparse View Framework

This chapter presents several strategies for segmenting and classifying the different corn stover fractions in the corn stover bale. The work shows the performance of the two-projection method proposed in chapter 5 to provide a 3D volume representation of higher density materials like rocks and soil clumps with adequate accuracy. Similarly, the work also shows the performance of a statistical reconstruction method, MLEM, to reconstruct the volume of more complex problems like the corn cobs and stalk nodes using 5 X-ray projections.

Chapter 7: Assessing the Framework for X-ray Tomography at a Commercial Scale Biorefinery

This chapter interprets the performance of X-ray tomography at the biorefinery by identifying and studying the behavior of X-ray photon absorption parameters, such as the linear attenuation coefficient (μ), bulk density (ρ), and the elemental composition of the bale. In this work, the feedstock supply chain of the biorefinery is clearly described, followed by an analysis of the performance of X-ray tomography when integrating into the feedstock supply chain.

Chapter 8: Conclusion and Future Directions

The research work presented in this dissertation helps advance the sensing technology framework for the quality assessment of biomass feedstock at a commercial-scale biorefinery. An extensive discussion of each problem is presented in each

chapter. This chapter provides a generalized discussion of the research problems solved in the dissertation. The second half of the chapter provides future directions for tissue characterization with CT going forward.

CHAPTER 2

ANATOMICAL TISSUE CHARACTERIZATION IN CORN STOVER BALES WITH COMPUTED TOMOGRAPHY

This chapter explores the state of the art relevant to the work presented in this dissertation. The objectives of this chapter are two-fold. First, a short introduction to corn stover as a feedstock and its harvest logistics is presented, followed by discussing the various characteristics and unwanted variables added to the bales during harvesting, packing, and storing that affect the biofuel conversion process. Then a brief literature review of the biomass compositional analysis techniques is provided. Second, the basics of 3D X-ray imaging are introduced, followed by an in depth discussion of the fundamentals of CT.

2.1 Corn Stover as a Feedstock to the Biorefinery

Corn stover is a significant non-food biomass used as a feedstock to bioenergy and bio-based products. Corn stover refers to the stalks, leaves, cobs, and husks left in the field after grain harvest. The United States is estimated to produce 200 to 250 million dry tons of corn stover/year [19, 20, 21]. Because of its abundance and availability of collection infrastructure, corn stover has become the first non-food

biomass adapted to be used as a feedstock in bioenergy and bio-based products. Much research has been done on the biochemical processes to estimate and convert the bioethanol from corn stover. However, several unwanted variables are added to the corn stover bale during harvest, collection, and storage, which can cause significant damage to the equipment and reduce overall yield if left unprocessed.

2.1.1 Characteristics of Corn Stover Biomass

Corn stover is mainly comprised of stalks, leaves, cobs, and husks. These materials are recalcitrant to bio-degradation. The sugar content present in the corn stover fractions is not directly available for fermentation. The main constituents of the corn stover are cellulose, hemicellulose, and lignin. In order to convert the corn stover fractions biologically, a pretreatment procedure is required to break down the complex polymer structures. During the pretreatment, the cellulose and hemicellulose are broken down into glucan and xylan. These Glucan and Xylan are then fermented to produce bioethanol.

A lot of research has been done to optimize the pretreatment procedure. Each tissue fraction responds differently at the pretreatment and acid hydrolysis steps resulting in the variation in the amount of glucan and xylan available for conversion with different fractions of the corn stover [22]. Figure 2.1 shows the glucan and xylan content recovered from various corn stover fractions with different pretreatment procedures. If each fraction is not processed appropriately, the overall ethanol yield is affected. Thus, having prior knowledge about the volumetric content of different anatomical fractions present in the corn stover bale at the preprocessing or screening stage can help optimize the conversion process, achieve

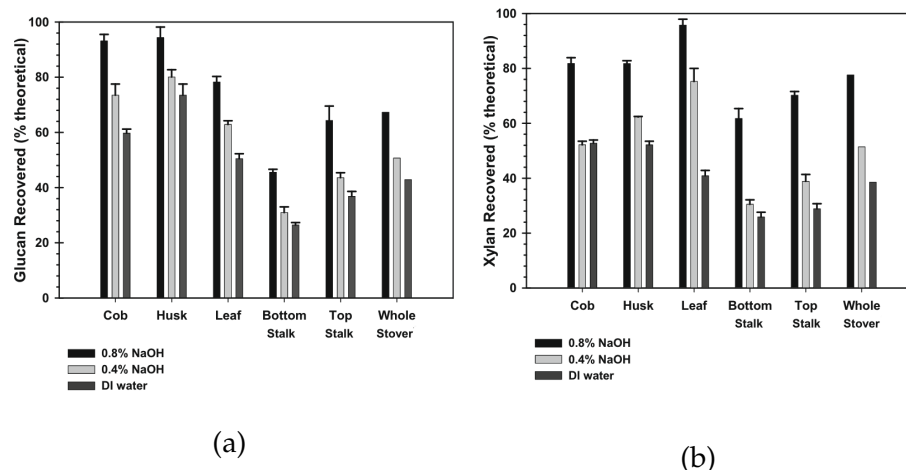


Figure 2.1: Amounts of (a) Glucan and (b) Xylan recovered with various pretreatment methods for each corn stover fraction [22]

a high yield and determine the payout for the bale.

Generally, corn stover harvesting occurs within a few days to a few weeks after the grain harvest. The corn stover harvest process mainly comprises windrowing, bailing the stover, and moving it to storage sites. Windrowing refers to placing corn stover materials into rows of an appropriate size suitable for the bailing. Windrowing or creating corn stover rows is typically done by chopping the stalks after the grain harvest. Once this is done, a bar or wheel rake is used to gather the stover into a single row (see figure 2.2). Then the corn stover is baled to create high-density packages that can be transported efficiently. During the bailing process, a machine picks up and packs the loose windrowed stover materials in the form of a rectangular or cylindrical bales (see figure 2.3).

Depending upon how the windrowing and bailing are completed, the corn stover harvesting is classified into two categories: single-pass and multi-pass. In single-pass harvesting, both windrowing and baling processes are done together.



Figure 2.2: A bar rake being used to create a corn stover windrow [23].

The corn stover is collected directly off the combine's back before it hits the ground and is converted into bales. In multi-pass harvesting, the windrower places the corn stover materials into rows on the ground during the first pass. During the second pass, the baler picks up and packs the materials into bales. More soil contamination is observed with multi-pass than single-pass harvesting since corn stover materials are left on the ground between steps.

Soil contamination, also referred to as soil-derived ash content, influences the pretreatment procedure and affects the disposal costs at the conversion facility. It also affects the overall value of the delivered lot of biomass. High ash contents can cause problems like slagging, fouling, and corrosion in the thermochemical process. Similarly, presence of soil-derived ash content during the ethanol conversion process can cause the displacement of the fermentable carbohydrate, increasing the overall operation costs. Because of this, ash content receives special attention. The



Figure 2.3: (a) Square bale dropped off from the end of a baler, (b) Round corn stover bales in the field [23].

amount of soil entering must be minimized to maintain the feedstock's quality in combustion or liquid fuel conversion [24]. Likewise, rocks and metal contaminants are also observed in the corn stover bales. If these are left unprocessed, they can cause significant damage to the grinding equipment and cause sparks that can lead to a fire hazard [25].

Like ash content, the moisture content present in the lignocellulosic biomass is another quality measure that affects the overall ethanol yield and cost of the production process. High moisture content increases the chance for biological degradation. Biological degradation reduces the carbohydrate content that will be available for fermentation. Moisture content determination at the biorefinery helps to determine the storage conditions needed between arrival and conversion. If the moisture content in the biomass bale is greater than 35%, it can affect the grinding equipment, which can drastically increase the preprocessing cost. It is essential to include a sensing framework to provide volumetric content information about the soil-derived ash content, rocks, metal contaminants, and moisture content along with the corn stover tissue fractions.

2.1.2 Literature review on biomass compositional analysis

Different components of the lignocellulosic biomass behave differently during the biomass conversion process. Knowledge of the biomass composition is important to optimize or modify the operational conditions at the biorefinery to increase yields, decrease fouling, extend catalyst life, etc. Wet chemical analysis methods are popular and are the earlier methods developed for determining the biomass composition. Classical wet chemical analysis methods employ a two-step sulphuric acid hydrolysis, and have been in use for over a century. Initially adopted from the pulp and paper industry, there have been significant improvements in the adopted methods over time [26, 27]. The NREL had defined a set of procedures to study the biomass composition with wet chemical methods [28]. Standard wet chemical analysis methods provide reliable information on the biomass composition. However, these are very time consuming and labor-intensive; it takes somewhere around 20 to 30 staff hours split between several different staff members over two weeks to analyze 6 to 10 samples. Moreover, wet chemical analysis methods are expensive, approximately \$800 - \$2000 per sample [29]. Over the years, development in the wet chemical analysis methods has increased the number of samples that can be tested in reduced time, but it still has a long way to go [30]. Similarly, the ash and moisture can be studied using dry analysis methods. Each sample is dried in an oven and the weight difference before and after is considered as moisture net weight. Ash is calculated by burning the sample and then calculating the net weight.

Quantitative spectroscopy is another non-destructive technique adapted over

the years to study the biomass composition. It is considered a fast and reliable alternative to traditional analytical methods for determining the sample's chemical composition. In 1988, Wessman et al. used airborne near-infrared spectroscopy in agricultural food industries to study the lignin content. Similar work was proposed by Rodriguez et al. in 2001 [31] to use near-infrared spectroscopy in fruit juices. Later, Hames et al. used the near-infrared (NIR) spectroscopy and partial least squares (PLS) multivariate regression analysis to develop a calibration model to predict the chemical composition of the feedstock (corn stover) and ethanol yield in the acid pre-treated and enzymatic hydrolysis process [32].

Fourier Transform-NIR spectroscopy has been popular, because it provides a higher resolution and brings higher wave number accuracy to the chemometrics. Griffiths and De Haseth in 1986 achieved higher resolution without compromising the signal-to-noise ratio [33]. There were several models proposed in the past which take into account the moisture content and ash content to get the true heating value. In 2005 Lestander and Rhén [34] proposed a model which uses NIR spectroscopy in correlation with a biorthogonal Partial Least Squares approach to determine the moisture and ash content, and then corrected for the heating value. In 2006 Jensen et al. [35] proposed a model which accounts for the moisture content by considering the dielectric properties of water. In the same year Samuelsson et al. [36] discussed two other approaches for the moisture content determination: xylene distillation and freeze drying. Nystrom and Dahlquist [37] used X-ray spectroscopy to determine the moisture content in wood chips. Huang et al. [38] proposed two models to determine the heating value by just considering ash content. This work involved the use of Artificial Neural Networks (ANN), a method

used earlier by Patel et al. [39]. In 2012 similar to [34] Everard et al. [40] using the work produced by Sanderson et al. [41] in 1996, proposed a model to predict the heating value by using visible and infrared spectroscopy by understanding the moisture content and ash content.

2.2 Background on X-ray Tomography or Computed Tomography

The discovery of X-rays in 1895 by the German scientist Wilhelm Rontgen prompted the evolution of the non-invasive radiation imagery field. With its significant advantage in medical imaging, it quickly attracted a lot of audience attention. In 1917 Wilhelm Johann Radon developed a transformation technique to reconstruct the 3D image from X-ray projections using a finite number of line integrals. Using Radon's theory the first CT scanner was invented in 1972 by Allan M. Cormack and Sir Godfrey Newbold Hounsfield. Because of its huge demand in medical and industrial applications, there was a significant development in the reconstruction technique and CT scan acquisition techniques. This is still subject to active research to obtain a high-quality reconstruction with minimal exposure and cost.

Now, X-ray tomography or computed tomography (CT) is a widely adopted non-destructive analysis technique used in clinical visualization. In X-ray tomography or CT, the target material or the object is irradiated with X-rays from several angles, circling the object to get a large number of radiographic projections. The X-ray projections are then reconstructed using a mathematical algorithm to represent the target object with a cross-sectional slice image. Multiple 2D cross-sectional slices are then stacked together to produce a 3D representation of the object. X-rays

can penetrate through any matter, and the amount of penetrating X-ray photons is material-dependent. This ability to penetrate through matter is the reason for wide adaptation in clinical and industrial visualization. This section aims to briefly introduce how X-rays interact with matter, the underlying physics, and a brief introduction of cone-beam computed tomography (CBCT).

Fundamentals of X-ray Interaction

X-rays belong to the set of electromagnetic (EM) rays with wavelengths from 0.01 nm to 10 nm , which follow the rules of electromagnetic radiation. EM waves have radiant energy which passes through spaces in the form of waves or photons. Similar to visible light, X-rays lose a certain amount of energy as they pass through the material. The reduction in the radiant energy is referred to as attenuation. Several physical effects of X-rays contribute to attenuation, including a change of the photon count, photon direction, or photon energy.

Generally, X-rays interact with matter in two ways: absorption and scattering. The first phenomenon, absorption, is also popularly known as the photoelectric effect. Here a valence electron from the outer shell absorbs the energy from the incident photons and the valence electron gets ejected with a kinetic energy equal to the binding energy. Figure 2.4a shows the phenomenon when there is no interaction. Figure 2.4b illustrates the phenomenon of photoelectric absorption. Another property that is observed is scattering. In scattering, two types of phenomena can be observed: Compton scattering and Rayleigh scattering. With Compton scattering, photons collide with the loosely bonded outer shell electron. Some photon energy is transferred to the electron, and the collision impact deflects the incident

photon. Figure 2.4c shows the Compton scattering effect. Rayleigh scattering is mainly observed with low X-ray energies. In this scattering phenomenon, the photon collides with the electron and vibrates with the energy and frequency the same as the photon. Figure 2.4d shows the Rayleigh scattering. Because of the absorption and scattering phenomena, the incident photon loses some energy, and the rest transmits through the object, called attenuation. With a linear attenuation coefficient or mass attenuation coefficient, these attenuation properties can be studied.

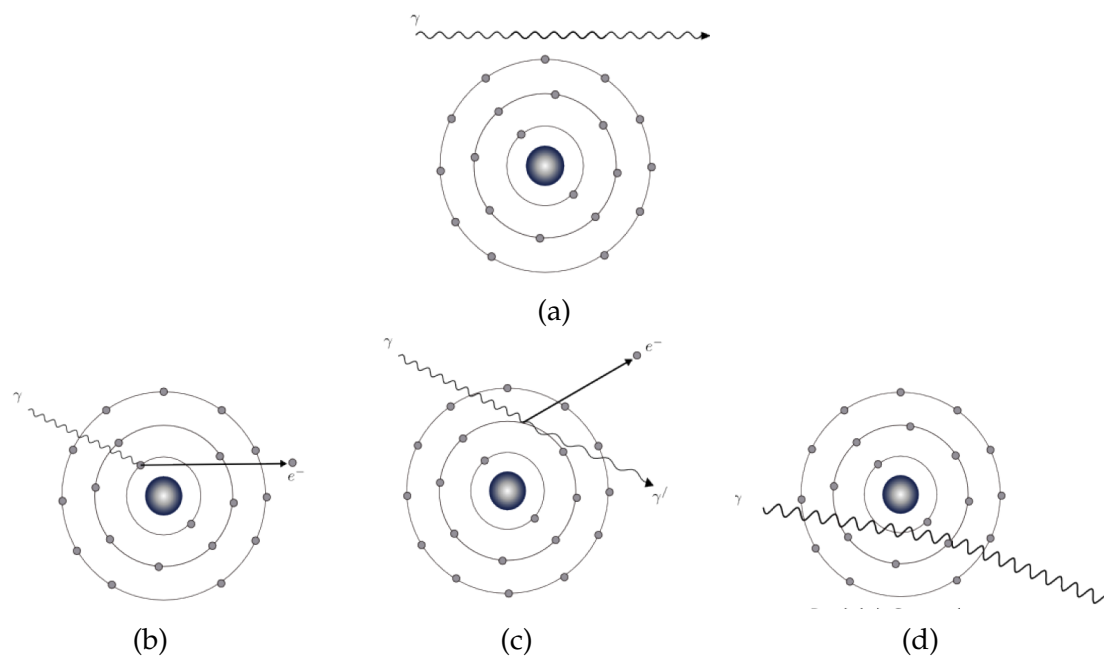


Figure 2.4: Principles of photon-matter interaction. (a) No interaction, (b) Photoelectric absorption, (c) Compton scattering and (d) Rayleigh scattering [42].

Underlying Physics of X-ray Interaction

As the incident X-ray beam passes through the material, because of the attenuation the radiation intensity decreases. The relation to the attenuation can be

defined using an ordinary linear and homogeneous first order differential equation with a constant coefficient

$$\frac{dI}{I} = -\mu dx. \quad (2.1)$$

Here μ is a proportional constant, which is also known as the material attenuation coefficient. I is the intensity of the incident radiation, dx is the thickness of the material. The material attenuation coefficient (μ) provides information regarding the contributions of both absorption and scattering phenomenon for a given material. Applying an integral on both sides of equation 2.1 gives

$$\int_0^x \frac{dI(x)}{I(x)} dx = - \int_0^x \mu dx \quad (2.2)$$

$$\log I(x) - \log I(0) = -\mu x. \quad (2.3)$$

By taking an exponential on both sides, equation 2.3 can be written as

$$I(x) = I(0).e^{-\mu x}. \quad (2.4)$$

This equation 2.4 is well-known as the Beer-Lambert formula.

Geometry of Cone Beam Computed Tomography

A conventional CT scanner is composed of four main components: (i) an X-ray tube for generating X-ray beams, (ii) an X-ray detector to measure the extent of signal attenuation, (iii) a set of mechanical axes for positioning the object, and (iv) a computer for data acquisition, reconstruction, and subsequent analysis. The most common CT scanner is a flat detector circular scanning trajectory system with

cone beam acquisition, known as Cone Beam Computed Tomography (CBCT) as in figure 2.5. In figure 2.5, a 3D object sits in the middle of the XYZ coordinate system, where the x-axis (\vec{OX}) is aligned with the source, S and the geometric center of the detector is at the tomographic angle $\theta = 0$. The detector has a planar geometry and rotates with the source around the z-axis (\vec{OZ}). If we represent the attenuation of X-ray photons as they pass through the 3D object with $f(\vec{r})$, where $\vec{r} = (x, y, z)$. Then each pixel in the detector at every tomographic angle is measured by

$$p(\theta, u, v) = p_0 \int_0^\infty e^{f(\vec{r}_0(\theta) + \alpha \hat{\gamma})} d\alpha, \quad (2.5)$$

where p_0 is the incident energy without attenuation, $\vec{r}_0(\theta) = (R \sin \theta, R \cos \theta, 0)$ is the source location, and $\alpha \in [0, \sqrt{D^2 + u^2 + v^2}]$. R represents the source to the center of rotation distance and D represents the source to detector distance. $\hat{\gamma}$ denotes the line direction between the source and detector coordinates (u, v) as in

$$\hat{\gamma} = \frac{\vec{d}(u, v, \theta) - \vec{r}_0(\theta)}{|\vec{d}(u, v, \theta) - \vec{r}_0(\theta)|}, \quad (2.6)$$

where $\vec{d}(u, v, \theta)$ represents the detector pixel corresponding to a given tomographic angle θ . Equation 2.5 represents the Beer's law for CBCT. The measured projection is a path integral of x-ray attenuation over the X-ray path [43].

While the planar array circular CBCT was just discussed, other geometries also exist like helical CT [44], parallel CT [45]. Similarly, circular arrays instead of planar arrays are also used in several applications. Changing the mathematics based on the specified geometry is not complex.

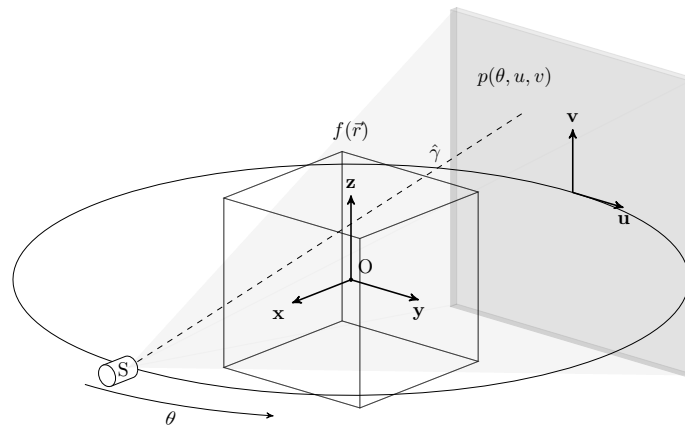


Figure 2.5: Geometry of CBCT [43]

2.3 Discussion

This chapter mainly aimed to provide a brief introduction to corn stover as feedstock and necessity to know the knowledge about the different contents of the bale to the interested audience. This chapter also presents a brief overview of the background related to the X-ray tomography or CT.

CHAPTER 3

QUANTITATIVE COMPARISON OF 3D SKELETONIZATION ALGORITHMS

As broadly discussed in chapter 2, providing quantitative information about the quality of the corn stover bales during the preprocessing stage helps optimize the conversion process. In this research, a new way of characterizing corn cobs in a corn stover bale is achieved using shape descriptors called skeletons, which will be presented in chapter 4. 3D skeletons are shape descriptors with a broad spectrum of applications in shape matching, recognition, animation, retrieval, and compression [17]. Skeletons provide a medial axial representation of an object. For 2-D objects, the skeleton is represented with a 1-D curve. For 3-D objects, the skeleton is represented with a combination of 2-D surfaces and 1-D curves (known as surface skeletons) or as a set of only 1-D curves (known as curve skeletons). Decades of research contributed to the development of a multitude of skeletonization algorithms. These skeletonization algorithms have differences in both the theoretical aspects (e.g., definition for curve skeletons) and practical aspects (e.g., spatial discretization (voxel or mesh)) [46]. The underlying assumptions or approximations incorporated in the skeletonization algorithms generate different skeletons for the same object in the presence of boundary noise. This causes chal-

lenges to the users of skeletons to determine which skeletonization algorithm to use for their respective application.

Currently, the evaluation of the 3D skeletonization algorithms is mainly done using quality metrics that are solely based on manual inspection [47]. The quantitative comparison of 3D skeletonization algorithms is still an open challenge. This chapter discusses the fundamentals of skeletonization algorithms, the implementation of two skeletonization algorithms, and two surface degradation models. It then presents different metrics to compare 3D skeletonization algorithms quantitatively and evaluate the skeletonization algorithms.

3.1 Skeletonization Algorithms

This section will introduce the fundamentals of skeletonization, and implementations of two 3D skeletonization algorithms developed during this dissertation. The two skeletonization algorithms are based on morphological thinning and the Euclidean distance transform.

3.1.1 Fundamentals on Skeletonization

Skeletons are shape descriptors with a broad spectrum of applications in shape matching, recognition, animation, retrieval, and compression [17]. Skeletons provide a medial axis representation of an object. Blum laid a foundation for skeletonization algorithms [48]. He defined a skeleton as being formed from the locus of centers of maximally inscribed circles (for 2D objects) or balls (for 3D objects)

of an object O (see Figure 3.1). The radius of each maximally inscribed circle R is also included in combination with circle centers M , to form a Medial Axis Transform, i.e., $MAT(O) = (M, R)$. A pair $(X, r) \in MAT(O)$ is called a medial atom. These medial atoms form the medial axis of the object O , which is also known as the skeleton of the object O . Underlying limitations such as the upper bound of maximally inscribed balls hinder the practical implementation of using this approach to create skeletons.

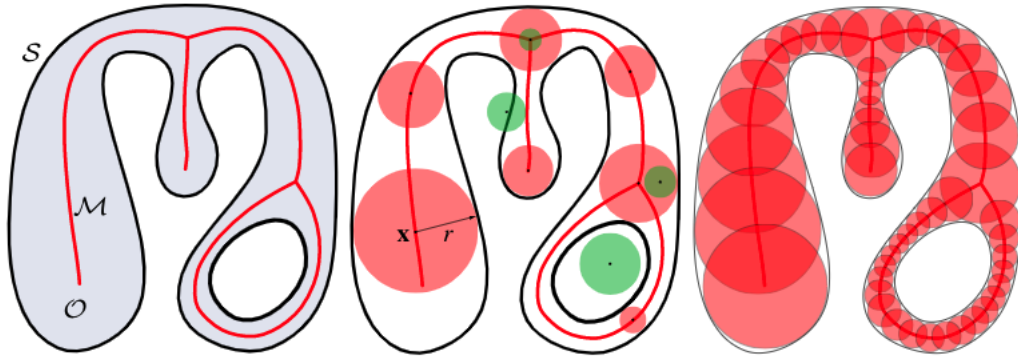


Figure 3.1: (a) The MAT skeleton M of the shape O with contour S , (b) Examples of maximally inscribed circles (red), a medial atom (X, r) , and circles which are neither maximal nor inscribed, thus not contributing to M (green), (c) Approximate reconstruction of O by the union of circles [47].

Over the years two variants of maximally inscribed circles or balls have become popular and are predominantly accepted in image processing and computer vision applications [47]. The first variant is the Grass Fire Analogy. This starts by treating object O as a patch of grass field. The boundary of O is $\delta(O)$. A fire is set along the boundary $\delta(O)$. The fire will propagate isotropically towards the interior of the object O . The Grass Fire Analogy states that where two fire-fronts meet is considered to be a quench point. The set of quench points forms the skeleton of

the object O [47].

The second variant is the Maxwell set, which is based on the distance transform. For an object $O \subset \mathbb{R}^3$ with boundary $\delta(O)$, we first define the distance transform, $DT_{\delta(O)} : \mathbb{R}^3 \rightarrow \mathbb{R}^+$

$$DT_{\delta(O)}(x \in O) = \min_{y \in \delta(O)} \|x - y\|. \quad (3.1)$$

The surface skeleton S_O , also called a medial surface, is defined as

$$S_O = \{x \in O \mid \exists f_1, f_2 \in \delta(O), f_1 \neq f_2, \|x - f_1\| = \|x - f_2\| = DT_{\delta(O)}(x)\}. \quad (3.2)$$

Here f_1 and f_2 are called contact points with the surface of the maximally inscribed ball in O with center at x , also called feature transform points. When $O \in \mathbb{R}^2$ this will yield a 2D skeleton, also known as the medial axis, and when $O \in \mathbb{R}^3$ it will return a curve skeleton.

For 2D objects the skeleton is represented with a 1D curve. For 3D objects it is represented with a combination of 2D surfaces and 1D curves (known as surface skeletons) or as a set of only 1-D curves (known as curve skeletons). Figure 3.2 shows examples of 2D skeletons and variants of 3D skeletons. Skeletonization algorithms can be widely classified into four different categories: Geometric Approaches, Distance Field Methods, General Field Methods, and Thinning or erosion. Algorithms that use geometric approaches represent an object boundary by a discrete set of points in a continuous space. These algorithms are based on Voronoi diagrams or other continuous geometric approaches [49]. The Voronoi

edges determine the symmetry structures in an object. Distance Field methods find the skeleton by determining quench points or singularities in $DT_{\delta O}(x)$ [50]. Generic field methods are similar to distance field methods except they use fields smoother than the distance transform [46]. Thinning, or erosion, is a sequential approach where the algorithm removes boundary pixels or voxels layer by layer while preserving the connectivity [46]. There are several implementations in 2D in most image processing libraries. With 3D there are several limitations. For this dissertation I implemented two 3D skeletonization algorithms in MATLAB and Python, which can be categorized into morphological thinning and distance field methods, which are described next.

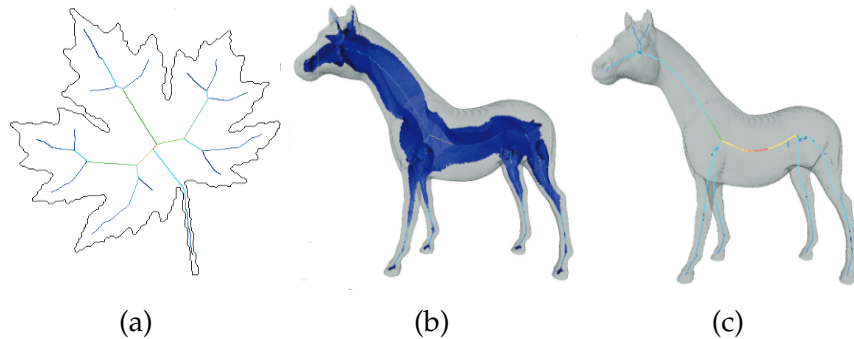


Figure 3.2: (a) 2D skeleton example, (b) 3D Surface skeleton example, (c) 3D curve skeleton example [47].

3.1.2 Morphological Thinning Implementation

The first 3D skeletonization algorithm we use is based on morphological thinning. This is the thinning algorithm by Lee et al. [51]. The morphological thinning approach discussed here iteratively removes voxels from the surface of the volume while preserving the topology of the 3D object. In this approach, the Euler characteristics with decision trees are used to solve the skeletonization problem. Euler

characteristics are one way to represent the topological space. The global formula defines the 3D Euler characteristics

$$X(s) = O(s) - H(s) + C(s), \quad (3.3)$$

where $O(s)$, $H(s)$, $C(s)$ are connected objects, holes (tunnels in 3D), and cavities. Euler characteristics are prominently used in topological thinning, a branch of 3D skeletonization techniques based on decision trees. To reduce the complexity of the problem (i.e., calculating $X(s)$), the authors solved the problem locally by using the edge, face, and vertex information in a given small neighborhood. The main drawback with this approach is that the locally computed Euler characteristics do not provide any information about the occupant in a given topological space. It only tells when a voxel/pixel in the given neighborhood is removed, whether it affects the overall topology.

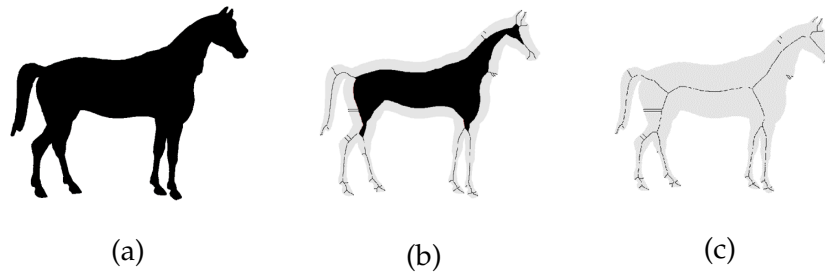


Figure 3.3: (a) Original image, (b) Partially thinned image, (c) completely thinned image

3.1.3 Euclidean Distance Transform based Implementation

The second skeletonization algorithm is based on Euclidean distance maps. The algorithm presented in this work is similar to the work presented by Latecki et

al. in [52]. This approach determines the critical points for the skeleton using a skeleton strength map (SSM). The skeleton strength map is calculated from the gradient vector flow. The gradient vector flow is estimated from the Euclidean distance map using the approach shown in [53]. In the Euclidean distance map, the distance from any voxel p to its nearest boundary increases when moved towards the center. One of the main disadvantages with distance transform-based approaches is that the resulting skeletons can be more than one voxel thick.

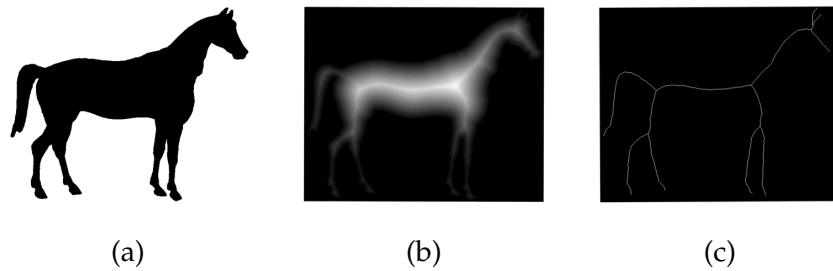


Figure 3.4: (a) Original image, (b) Euclidean Distance Map, (c) Skeleton extracted using SSM

3.2 Degradation Models

As mentioned in section 3.1.1, a skeleton needs to provide a medial axis representation of the object while capturing the topology of the underlying object. The underlying assumptions or approximations incorporated into the skeletonization algorithms make skeletons sensitive to boundary noise. The surface degradation can lead to issues like the generation of a spurious branch (see figure 3.5) or a change in the topology captured by the skeleton. In this section, we present two surface degradation models used to compare the skeletonization algorithms quantitatively. Using these two models, the surface noise can be controlled to provide

a quantitative comparison of the effect the noise has on the skeletons. Figure 3.6 shows the phantom cylinder used for all the experiments in this chapter. The rest of this section discusses the two surface degradation models in depth.

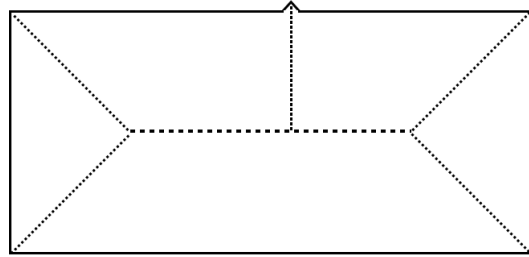


Figure 3.5: Spurious branch generated in the presence of surface noise.



Figure 3.6: A cylinder phantom used in the experiments.

3.2.1 Surface Roughness

The first degradation model is designed to create roughness on the surface of the 3D object. To create the roughness, noise following a Gaussian distribution with mean 0 and standard deviation σ is added to every voxel of the object O and surrounding air. The volume with noise is then thresholded, followed by

a morphological closing operation with a spherical structuring element with a diameter of 3 voxels. The morphological closing operation helps remove any isolated voxels left after thresholding and keeps only the regions directly connected to the cylinder. The degradation model incorporates the concept of Noise Spread described by McGillivary et al. [54]. Here Noise Spread defines how far from the original surface is affected by the noise. The threshold is always set to 0.5, making the noise spread directly related to the σ of the Gaussian noise. Figure 3.7a shows a section of the phantom cylinder without any noise. Figure 3.7b shows the section of the phantom with Gaussian noise on the surface after applying the threshold. Figure 3.7c shows the section from the phantom cylinder showing the surface roughness after the morphological closing operation.

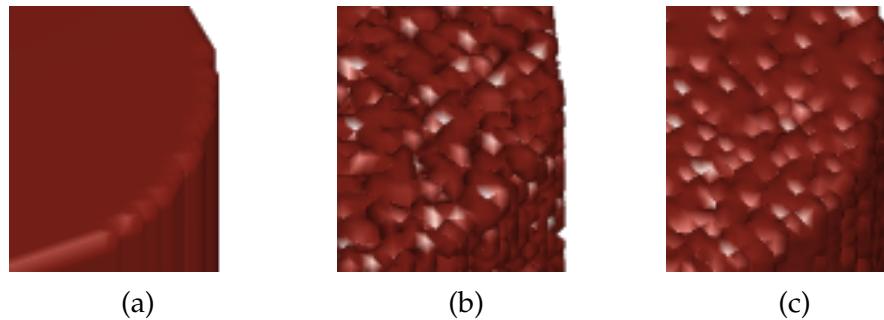


Figure 3.7: A section of the (a) phantom cylinder, (b) surface with Gaussian noise after thresholding, (c) surface after morphological closing operation.

3.2.2 Surface Protuberances

The second degradation model adds protuberances on the surface of the object. This model randomly selects a set of points on the surface and adds a sphere with a given radius centered at the point selected. This noise can be varied by changing the density of the protuberances, or the size (diameter) of the protuberances. When

experimenting with the surface protuberances degradation model, three types of protuberances are considered by changing the noise sphere's diameter. These three scenarios help to examine the effect that the diameter of the protuberance has on the skeleton. Figure 3.8a shows a section of the cylinder without any noise. Figure 3.8b, c, and d shows the same section of the phantom cylinder with the surface covered with protuberances with diameters 8, 10, and 14 voxels.

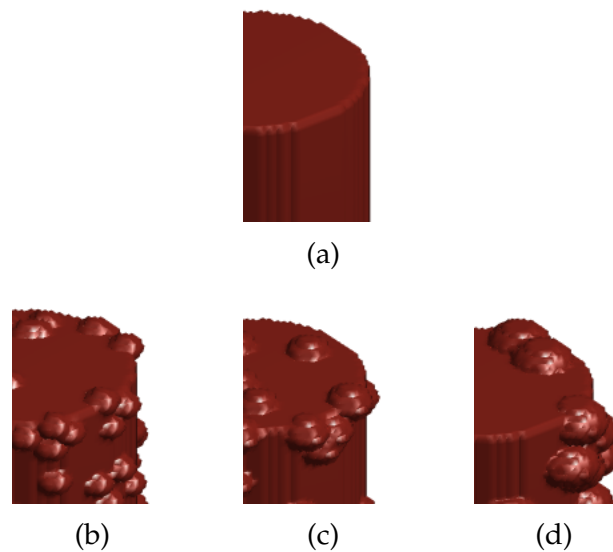


Figure 3.8: A section of the (a) cylinder phantom, cylinder phantoms with protuberances of diameter of (b) 8 voxels, (c) 10 voxels, and (d) 14 voxels.

3.3 Comparative Analysis Metrics

The skeletons created for surfaces without noise can be quantitatively compared with those created for surfaces with noise to see the effect the noise has on the skeletons generated. This section describes a set of three metrics through which the skeletons are compared quantitatively. First, one-to-one correspondence between the noise-free skeleton and noisy skeleton is established by using a dy-

dynamic time warping algorithm [55]. Then each metric is calculated between the corresponding skeleton nodes. The rest of the section defines each metric used in this dissertation for quantitative comparison of the skeletonization algorithms.

Mean Deviation

The mean deviation tells how far a skeleton node has deviated from its initial location in the presence of noise. The mean deviation is calculated by taking the average of the Euclidean distance between corresponding skeleton nodes. The mean deviation excludes any spurious branches generated because of the noise by using a simple thresholding technique. This metric helps to understand how the skeleton's path is changing in the presence of surface degradations.

Number of Added/Missing Nodes

The change in the number of skeleton nodes indicates a significant change in the topology between the original and noisy skeleton. This simple metric indicates any significant change in the topology of the skeleton. When the deviation between the number of skeleton nodes is minimal, it mainly indicates a deviation in the path or discontinuous paths in the skeleton. A significant change in this metric tells about the presence of branches. This metric is calculated by taking the difference between the number of skeleton nodes in the original skeleton and the noisy skeleton.

Number of Spurious Branches

Spurious branches are one of the main issues with many skeletonization algorithms. Figure 3.5 shows an example spurious branch generated in the presence of boundary noise. To determine a spurious branch the graph structure of the skeleton is extracted. A branch is determined when the distance between two nodes is approximately equal to the radius of the cylinder. In all the experiments, the phantom cylinder radius is small, so the complexity of the problem is simple. In the future, the branch estimation algorithm needs to incorporate other parameters to work with other complex structures.

3.4 Experiments & Results

In sections 3.1, 3.2, and 3.3 of this chapter, two implementations of the skeletonization methods, two surface noise models, and three quantitative metrics are described. To evaluate the two skeletonization algorithms, we calculate each metric for the two degradation models. With the surface roughness model, the standard deviation σ of the Gaussian noise is varied to observe the performance with an increase in the noise. Similarly, with the surface protuberances model the total percentage of surface points to become centers of the spheres is varied to observe the performance of skeletonization algorithms. When comparing results, the total percentage of surface area covered with protuberances is calculated to relate each metric with increase in the the surface area affected with noise. For each set of parameters the experiments are repeated ten times to provide an average estimate across the noise instances. All the comparison results are represented using box

and whisker plots. The box's top and bottom edges represent the 75th percentile and 25th percentile of the total data. The central mark in each box represents the median. The maximum and minimum values are represented with the whiskers, excluding any outliers. The outliers are represented using the '+' symbol.

Figures 3.9 and 3.10 outline the behavior of both morphological thinning and distance field based skeletonization algorithms with the surface roughness degradation model. Figures 3.9a and 3.10a show the box and whisker plot for the average deviation of the skeleton node observed with an increase in noise. From the figures it can be observed that as σ of the Gaussian noise increased, the mean deviation observed also increased, which tells that the path of the original skeleton has been modified with the increase in noise conditions. In comparison, the distance field-based skeletonization algorithm provides better performance; than the morphological thinning algorithm; change in the path of the original skeleton is only observed from moderate σ values i.e., greater than 1.5. Likewise, figures 3.9b and 3.10b show the number of missed/added skeleton nodes with increase in the σ of the Gaussian noise. Figures 3.9c and 3.10c show the increase in spurious branches with increase in σ of the Gaussian noise. Both algorithms at high σ values generate spurious branches in addition to the original skeleton. This behavior tends to change the average deviation observed in the skeleton, which reduces at a high σ value. With a high σ value, there is a high chance of voxels farther from the surface being affected by noise which causes the generation of spurious branches. The second metric is either directly correlated with mean deviation or spurious branches generation. Either the change in the path of the skeleton or the addition of spurious branches requires more skeleton nodes to represent the same skeleton

structure, increasing the number of skeleton nodes between the original and noisy skeleton. Figures 3.9 and 3.10 conclude that the surface roughness degradation model mainly changes the path of the original skeleton.

With the surface protuberances degradation model, three sets of experiments were conducted. The first experiment adds surface protuberances with a smaller diameter of 8 voxels to the surface of the cylinder phantom. In the second, protuberances with a diameter of 10 voxels were added to the surface of the phantom. The last scenario uses protuberances with a significantly larger diameter of 14 voxels added to the surface of the phantom. Figures 3.11, 3.12, and 3.13 outline the behavior of the morphological thinning method when small, medium, and large protuberances are added to the surface as noise. Likewise, figures 3.14, 3.15, and 3.16 outline the behavior with the distance field based skeletonization method. In each figure, window 'a' represents the average deviation metric, window 'b' represents the miss/add nodes metric and window 'c' represents the number of spurious branches generated.

When smaller protuberances with a diameter of 8 voxels are added on the surface, both the morphological thinning and distance field-based skeletonization methods tend to create a small number of spurious branches. Between the two algorithms, the distance field based skeletonization algorithm is more robust and shows no spurious branches when less than 50% of the surface area is occupied. However, with medium to large protuberances on the surface we see that the increase in noise directly correlates to spurious branch generation. The miss/add skeleton nodes and spurious branch metrics both show that the increase in the protuberances increases the spurious branches, and the number of skeleton nodes

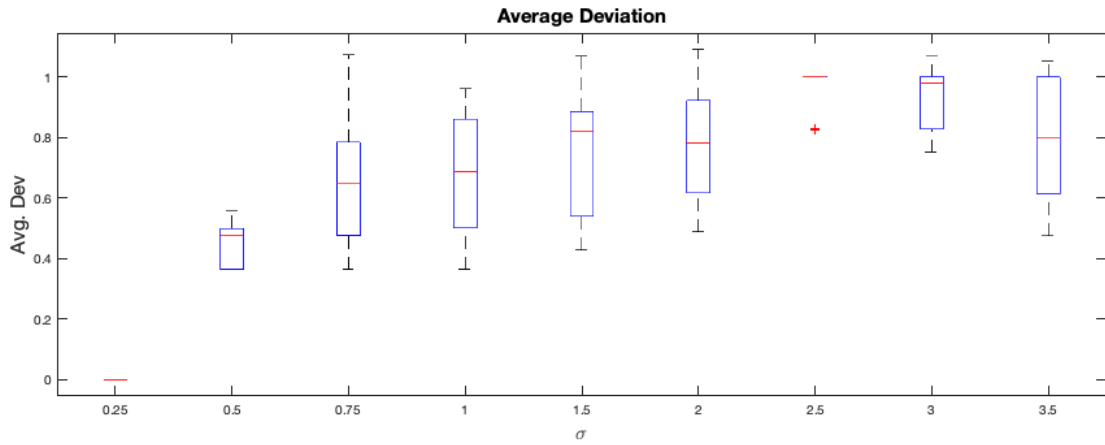
added to the original skeleton also increases. For the medium protuberance, when the total percentage of spheres used to add protuberances is increased beyond 75%, multiple spheres overlap, leading to an increase in the mean deviation metric observed. When multiple spheres are overlapping, it is creating a texture on the surface instead of the just protuberances, which is the reason for the change in the average deviation observed in the original skeleton.

3.5 Discussion

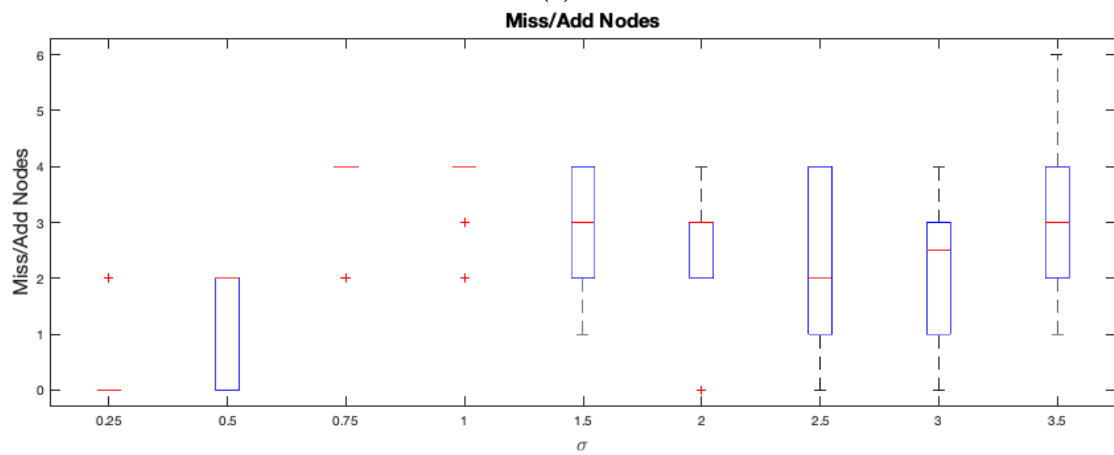
Section 3.4 showed how both morphological thinning and distance field based skeletonization algorithms perform under two types of noise conditions. With the surface roughness degradation model, the noise mainly changes the path of the original skeleton. In contrast, with the surface protuberances degradation model the generation of spurious branches is mainly observed with an increase in the noise. Both algorithms perform better, but the distance field method shows better performance than the morphological thinning method. Currently, the gradient vector flow estimation [53] with the distance transform field method is very time-consuming.

In the future, more work is required to produce a more efficient implementation to reduce the time load of the distance field based skeletonization method. Evaluating the skeletonization methods with more complex shapes like a toroid is required to analyze further and evaluate the skeletonization algorithms' performance. With the increase in the complexity of the shape, we need to consider other metrics which provides information such as how much of the original volume can

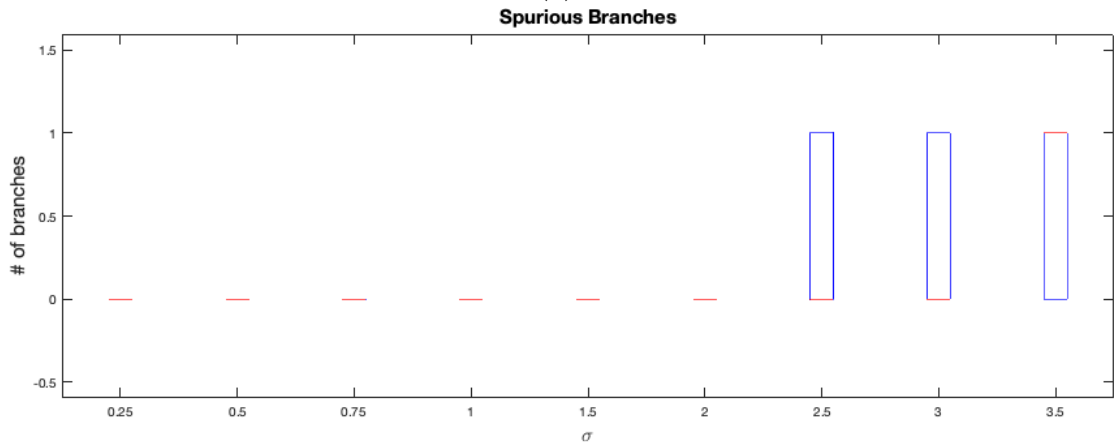
be recovered from the skeleton, how much of the corners are preserved, how thick is the skeleton, and whether the skeleton extracted is really along the center. Also, geometric entropy information needs to be estimated to correlate the original and a noisy skeleton. Other metrics which provide a piece of quantitative information on the preservation of the topography of the 3D object need to be defined.



(a)



(b)



(c)

Figure 3.9: Evaluation of morphological thinning based skeletonization method with surface roughness degradation model. Box and whisker plot showing the (a) average deviation, (b) missing/added nodes, and (c) spurious branches.

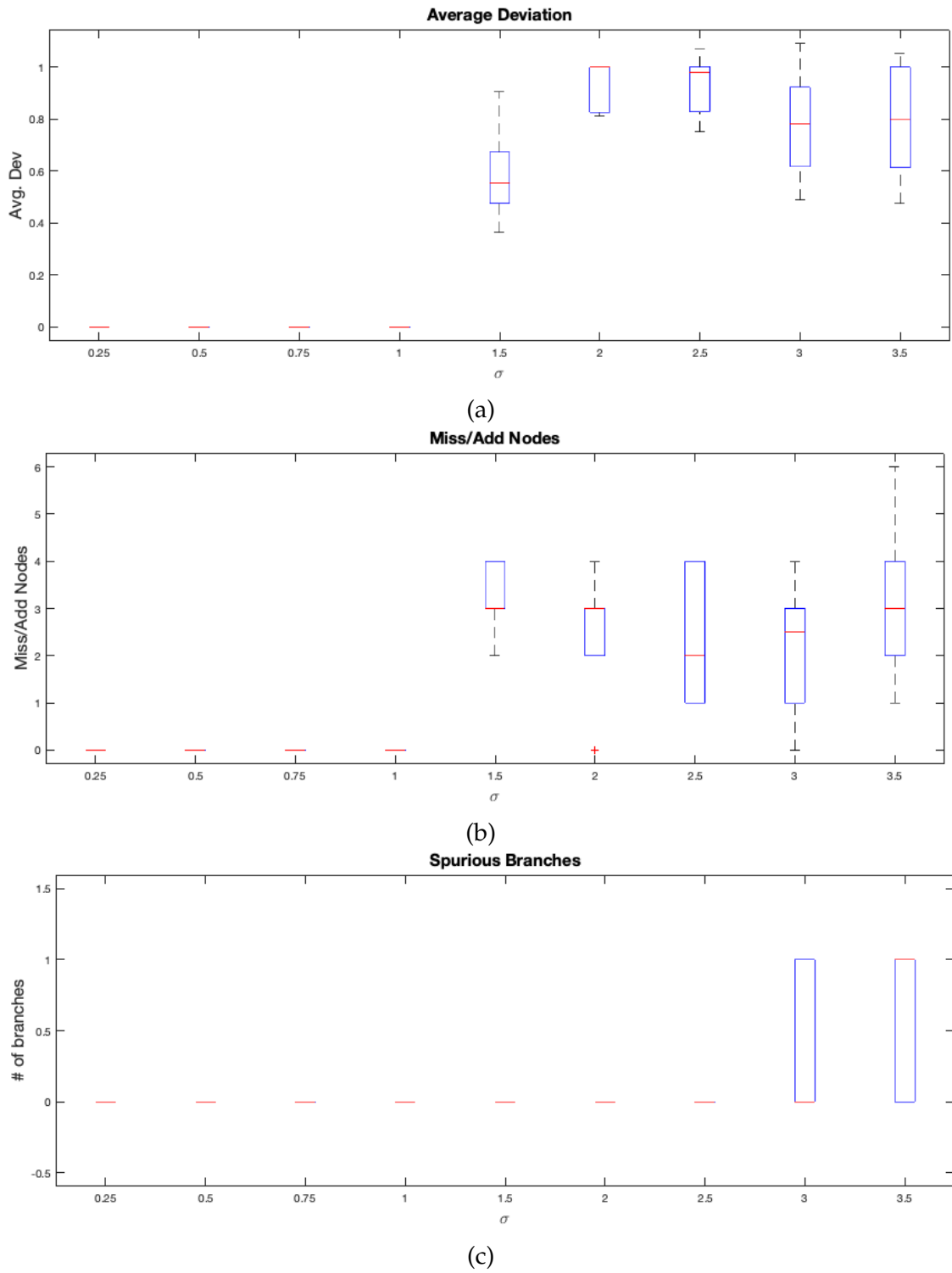
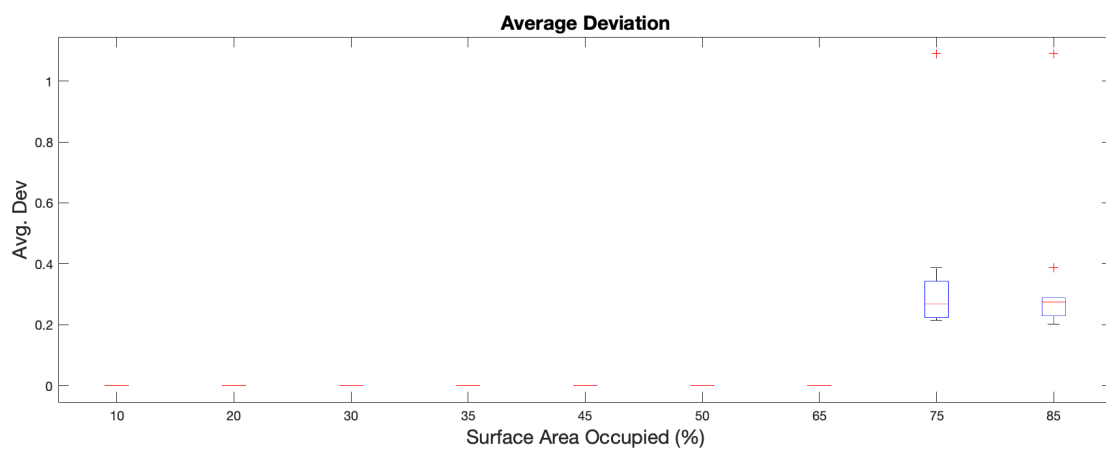
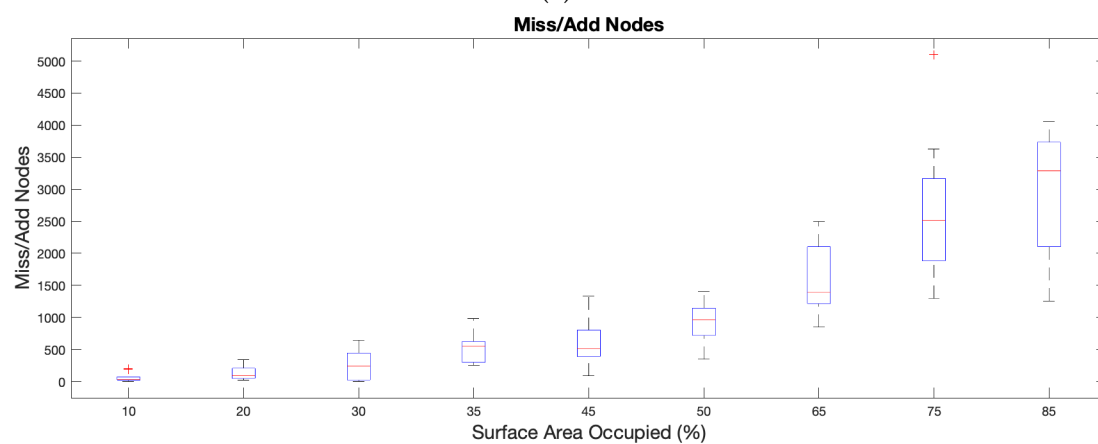


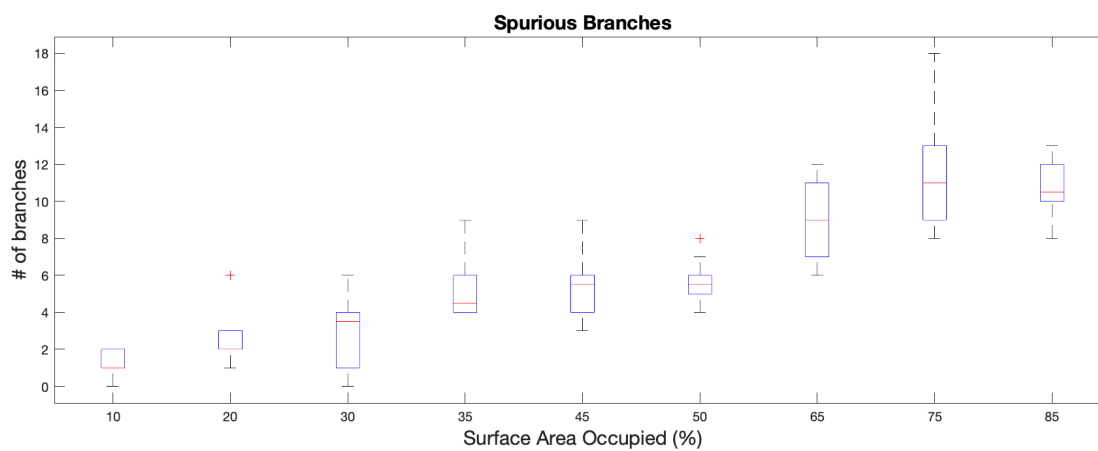
Figure 3.10: Evaluation of distance field based skeletonization method with surface roughness degradation model. Box and whisker plot showing the (a) average deviation, (b) missing/added nodes, and (c) spurious branches.



(a)



(b)



(c)

Figure 3.11: Evaluation of morphological thinning based skeletonization method with protuberances of diameter 8 voxels. Box and whisker plot showing the (a) average deviation, (b) missing/added nodes, and (c) spurious branches.

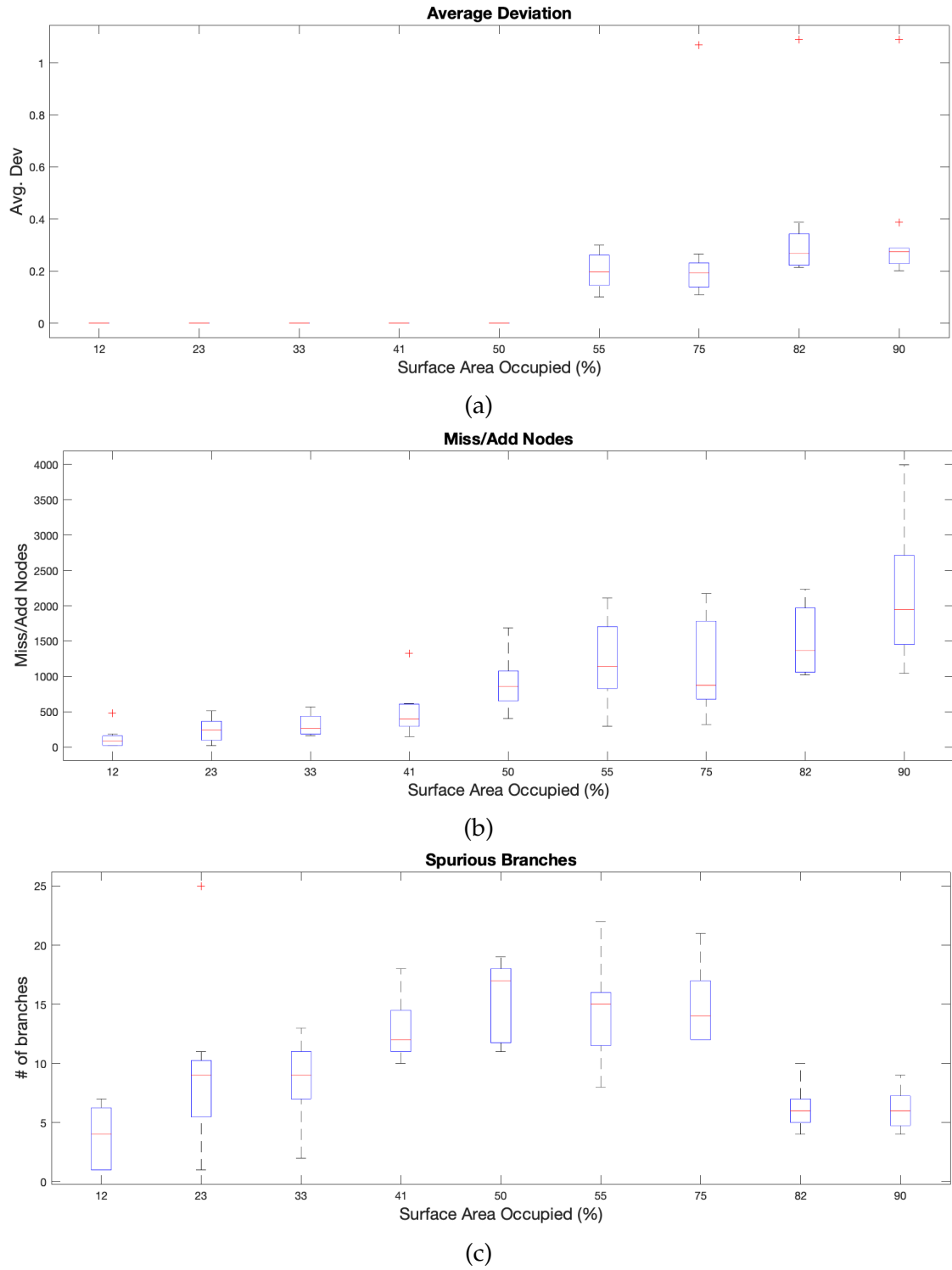


Figure 3.12: Evaluation of morphological thinning based skeletonization method with protuberances of diameter 10 voxels. Box and whisker plot showing the (a) average deviation, (b) missing/added nodes, and (c) spurious branches.

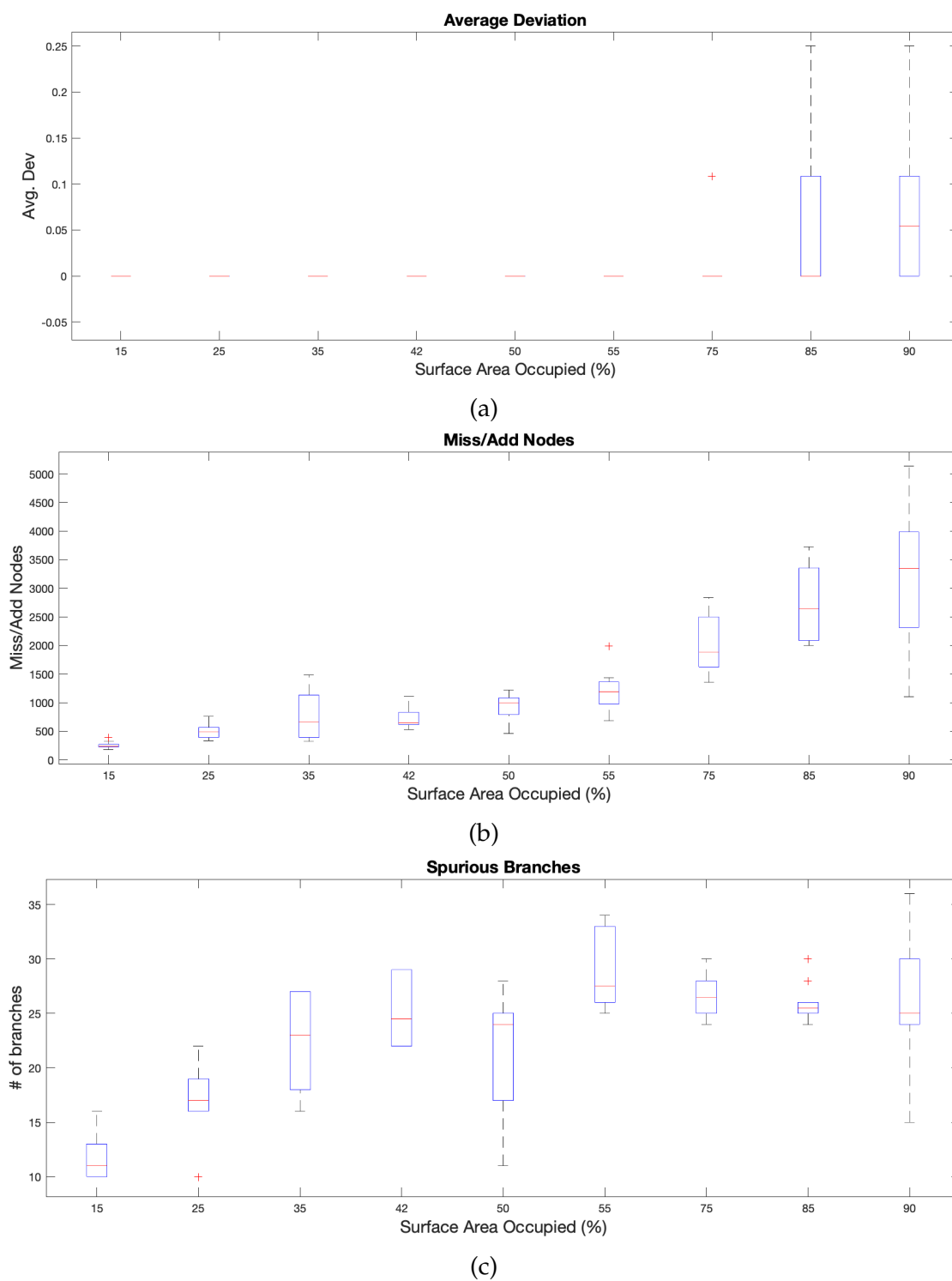


Figure 3.13: Evaluation of morphological thinning based skeletonization method with protuberances of diameter 14 voxels. Box and whisker plot showing the (a) average deviation, (b) missing/added nodes, and (c) spurious branches.

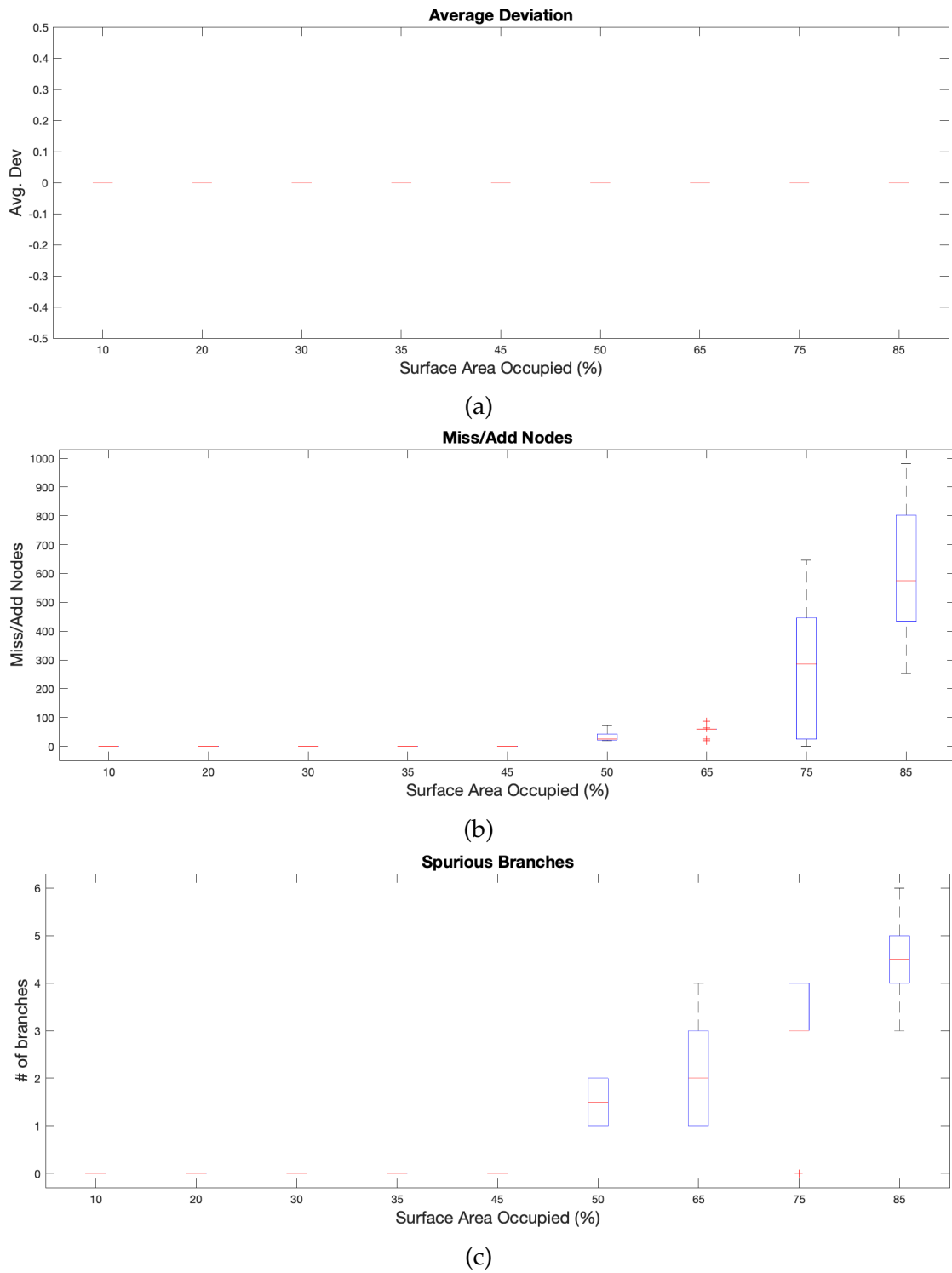


Figure 3.14: Evaluation of distance field based skeletonization method with protuberances of diameter 8 voxels. Box and whisker plot showing the (a) average deviation, (b) missing/added nodes, and (c) spurious branches.

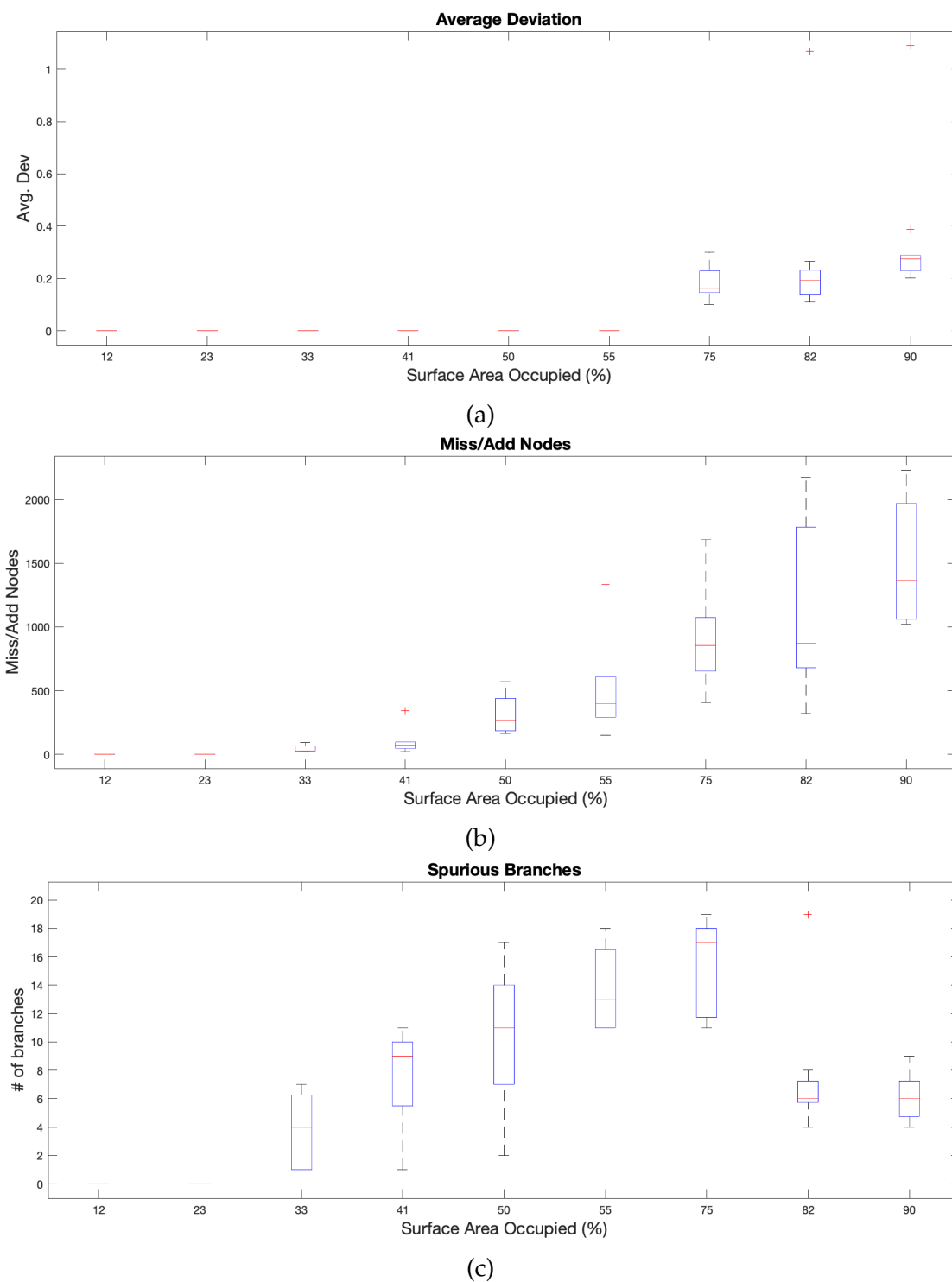


Figure 3.15: Evaluation of distance field based skeletonization method with protuberances of diameter 10 voxels. Box and whisker plot showing the (a) average deviation, (b) missing/added nodes, and (c) spurious branches.

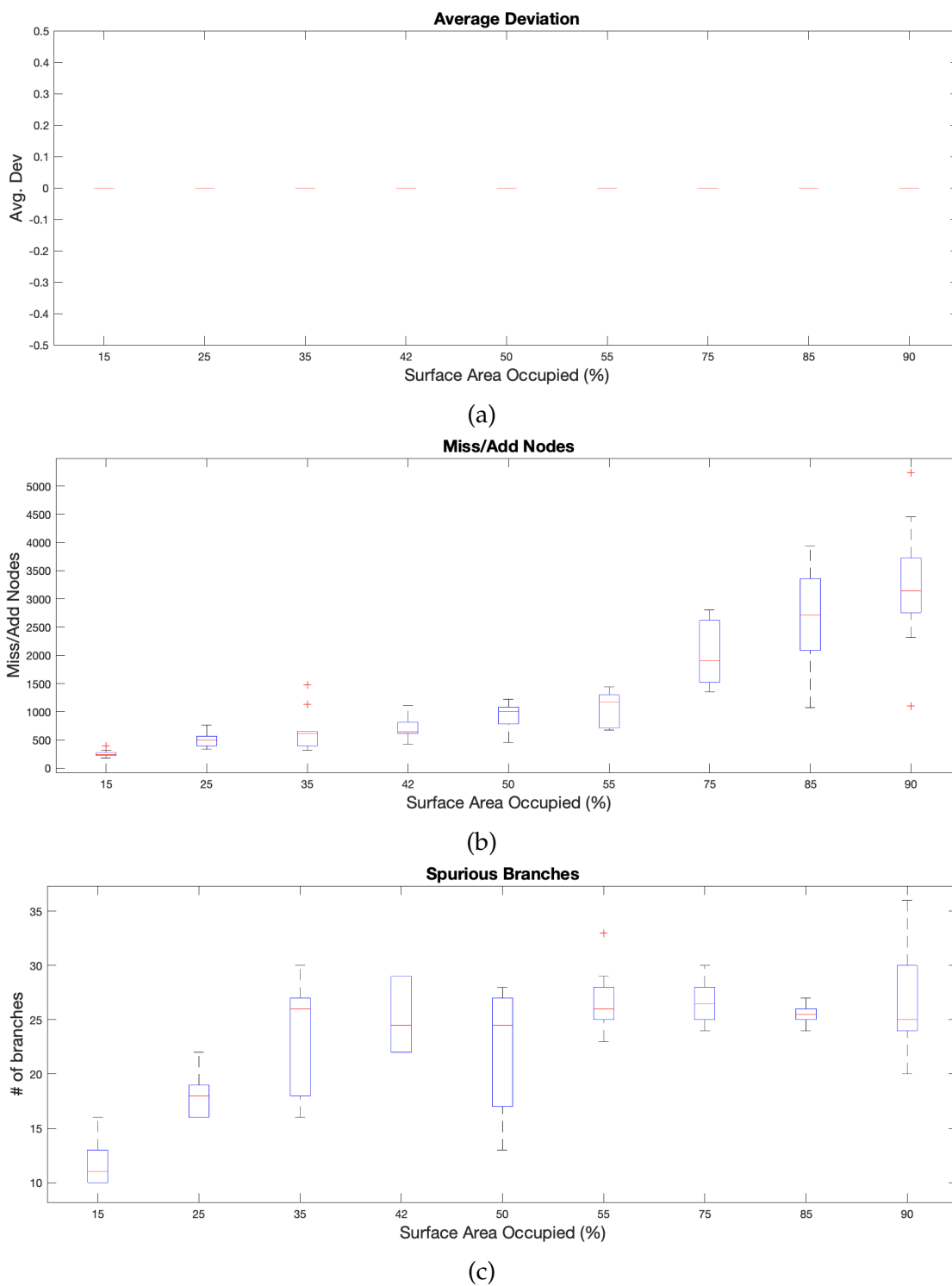


Figure 3.16: Evaluation of distance field based skeletonization method with protuberances of diameter 14 voxels. Box and whisker plot showing the (a) average deviation, (b) missing/added nodes, and (c) spurious branches.

CHAPTER 4

ANATOMICAL TISSUE CHARACTERIZATION IN CORN STOVER BALES WITH 3D IMAGE ANALYSIS TECHNIQUES

As stated in chapter 1 BETO's current technological focus is on developing the next-generation biofuels. The next-generation biofuels rely on non-food (terrestrial cellulosic and algae-based) resources. Because of its abundance and the availability of collection infrastructure, corn stover is one of the primary crop residues adapted to produce biofuels, mainly bioethanol. As discussed in chapter 2 different tissue fractions in the corn stover bale: cobs, stalks, leaves, and husks have a variable chemical composition and conversion properties. Likewise, unwanted materials like rocks, metal contaminants, and soil clumps in the bale can be detrimental to the conversion efficiency and the equipment. Thus determining the volumetric content information of the different tissue fractions present in the corn stover bale during preprocessing helps optimize the conversion process and estimate the biofuel yield from a given bale. This chapter presents the 3D image analysis techniques that provide quantitative information on the contents of the corn stover bale utilizing X-ray tomographic data.

At the harvest, the baler packs the corn stover in bales, which are sent to the biorefinery. Here for the experiments, we prepared corn stover bales in the form of

a mini-round cylinder with a diameter of 12.70 cm and height of 15.24 cm (see figure 4.1b). The X-ray CT scans for the bales were acquired using a North Star Imaging (NSI) CT 3D X-ray system at the Idaho National Laboratory. Figure 4.1 shows the geometric setup used for imaging the corn stover bales. Figure 4.1a is the detector and 4.1c shows the X-ray source. Figure 4.1b shows the corn stover bale in the middle. For the experiments, scanning was performed with an X-ray tube peak accelerating voltage of 150 kVp and corresponding tube current-time settings at $60\text{ }\mu\text{A}$. The NSI CT system is configured to use 720 X-ray projections in the complete 360-degree range to reconstruct the 2D cross-sectional slices of the 3D object. The NSI CT system outputs the 2D cross-sectional slices. Multiple 2D cross-sectional slices are stacked together to provide a 3D reconstruction of the bale.

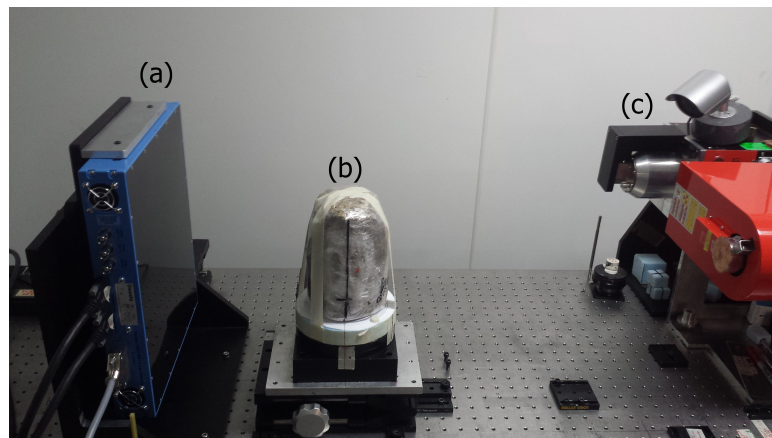


Figure 4.1: CT setup used to extract the radiographs of corn stover bale with (a) detector (b) mini-round corn stover bale (c) X-ray Source.

After acquiring the X-ray reconstructions, several image analysis techniques are applied to extract the corn stover content information. Figure 4.2 shows the workflow diagram of the different stages we propose to use for volumetric content estimation of different anatomical fractions in the corn stover bale. After acquiring the 2D cross-sectional slices, we preprocess the 2D cross-sectional slices to remove

the noise and simplify the data for easy segmentation in the later stages. The next step involves detecting and extracting the volume information of rocks and metal contaminants, followed by soil clumps present in the bale. Then in this chapter, we present an approach for corn cob segmentation and volume estimation using 3D shape descriptors called skeletons. The rest of the chapter discusses the various stages shown in figure 4.2 in detail.

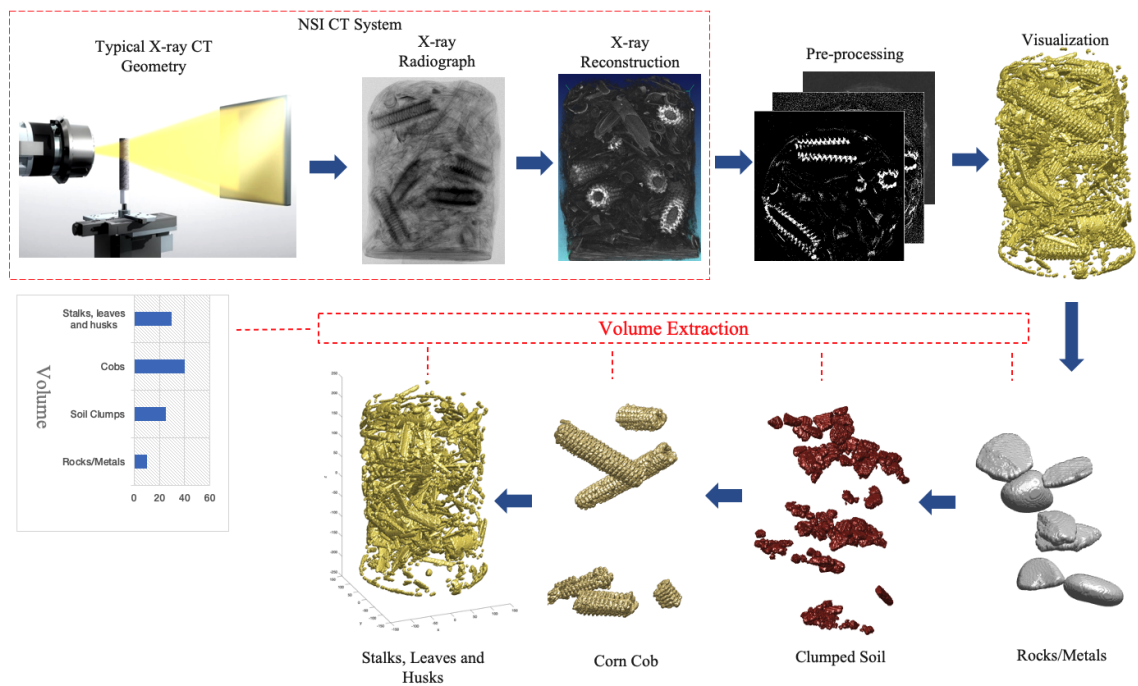


Figure 4.2: Work flow diagram representing the different stages of the tissue characterization in a corn stover bale.

4.1 Pre-processing

The intensity distribution in the raw reconstructed 2D cross-sectional slices from the NSI CT system is based on the incident energy and material absorption rate. The distribution cannot be directly used for classification as there is a lot

of information which cannot be directly linked for further processing of the data. In the preprocessing stage, the entire intensity distribution of the reconstructed 2D slices is modified to make further processing easier. Figure 4.3a shows a raw reconstructed 2D cross-sectional slice. Figure 4.4a shows the 3D reconstruction of the corn stover bale formed by stacking multiple 2D cross-sectional slices before preprocessing.

First, adaptive thresholding is applied to convert the 2D reconstructed images to a bi-level format. Figure 4.3b shows a 2D cross-sectional slice after thresholding. Figure 4.4b shows the 3D reconstruction of the corn stover bale after thresholding. A convolution filter is applied to remove isolated voxels, which can be observed in both figures 4.3b and 4.4b. Figures 4.3c and 4.4c shows the final reconstructions after preprocessing. The bi-level data is multiplied with the original data and later scaled back to 255 grayscale values to simplify the task of segmenting the rocks, metal contaminants, and soil clumps in the corn stover bale.

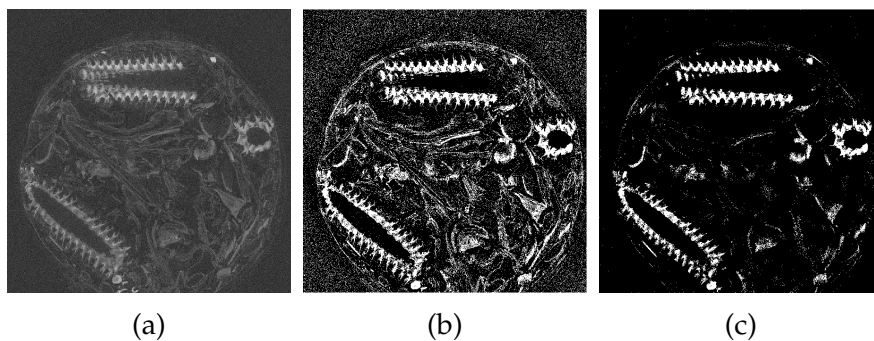


Figure 4.3: Example (a) raw 2D reconstructed slice, (b) reconstructed slice after thresholding, (c) reconstructed slice after preprocessing.

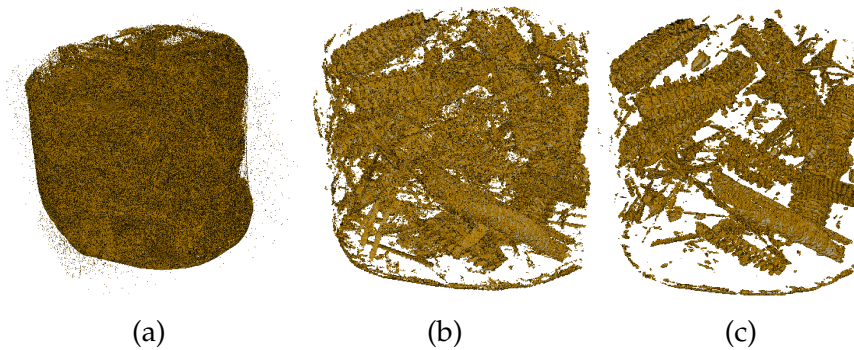


Figure 4.4: 3D reconstruction using (a) raw 2D reconstructed slices, (b) reconstructed slices after thresholding, (c) reconstructed slices after preprocessing.

4.2 Detection and Volume Estimation of Ash Content

After preprocessing, the first step is to extract information about the ash content. The term ash content refers to rocks and soil clumps present in the bale. These materials have high bulk density compared to corn stover. For example, rocks have a bulk density equivalent to 2.62 g/cm^3 , and soil clumps generally have a bulk density of 1.3 g/cm^3 . Whereas the corn stover materials have a bulk density equivalent to 0.15 g/cm^3 . Higher bulk density usually results in the higher absorption of the X-ray photons, which appear as higher intensity regions in the reconstructed data. This can be easily observed in figure 4.5b, where it shows the histogram of the intensity distribution of an example reconstructed slice (see figure 4.5a) with rocks, soil clumps, and corn stover materials. The histogram clearly shows the intensity difference between the rocks, soil clumps, and corn stover materials. In figure 4.5a, the respective region where rock is present is highlighted with a red circle, soil clumps location is highlighted with a blue circle, and the background shows the corn stover materials.

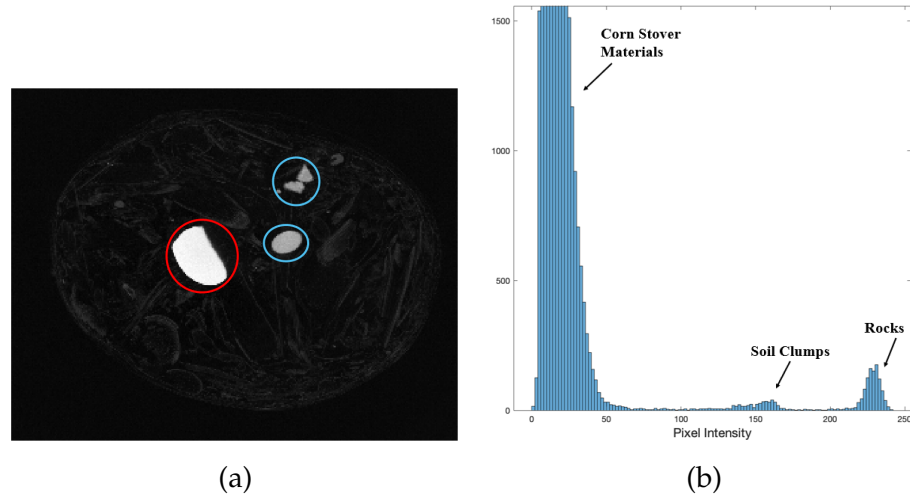


Figure 4.5: (a) 2D image of X-ray reconstructed data with rocks highlighted with red circle and soil clumps are highlighted with blue circle, and (b) histogram showing the intensity distribution of the 2D image.

The histogram clearly shows that the rocks and soil clumps are separated in intensity from corn stover materials. We applied a histogram-directed thresholding technique to segment the regions of rocks and soil clumps present in the bale from corn stover materials. After segmenting, the volume and position information is calculated by using a connected component algorithm. Two physical bale samples were created for analysis, one filled with rocks and the other with soil clumps. Figures 4.6a and 4.6b show the 3D reconstructions of the bales showing rocks and soil clumps present in the bales. Table 4.1 and 4.2 shows the volume accuracy and average position deviation observed for the test bales.

Table 4.1: Volume of rocks extracted from the test bale

Volume Accuracy (%)	Average Position Deviation (")
99.67	0.01

Table 4.2: Volume of soil clumps extracted from the test bale

Volume Accuracy (%)	Average Position Deviation (")
99.50	0.05

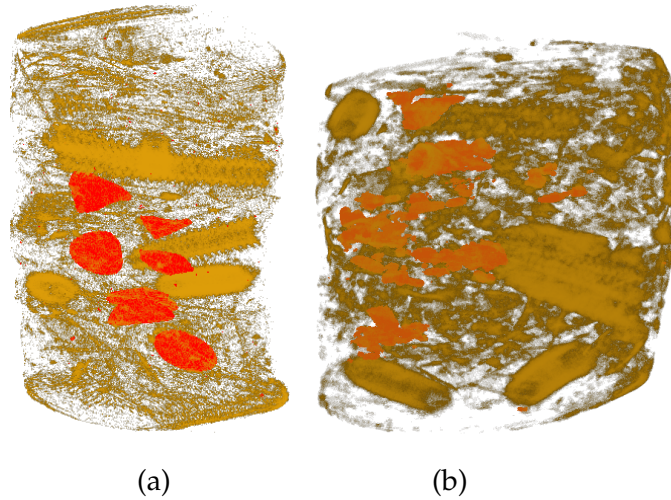


Figure 4.6: 3D reconstruction of the bale with (a) rocks, (b) soil clumps where contaminants are shown in alternate colors.

4.3 Detection and Volume Estimation of Corn Cobs

After high bulk density rocks and soil clumps are detected, and their respective volume is estimated, the next step involves detection and volume estimation of corn cobs present in the bale. This section focuses on extracting the corn cob volume using 3D shape analysis. Because the corn stover materials are organic, moisture content can increase the bulk density, changing the overall attenuation of the X-ray photons. This affects the intensity distribution observed in the 2D cross-sectional slices. So, using a raw intensity distribution to classify different tissue fractions of the corn stover materials is not practical. Corn cob segmentation and volume estimation are achieved using 3D shape analysis with 3D skeletons in

this work.

3D skeletons provide shape information about an object, while preserving the topology of the object. The skeletons are represented with graphs, which includes node and edge information. The graphs generally provide a pairwise relationship between each node. Figure 4.7a shows an example corn cob. X-ray reconstruction showed the corn cobs are hollow in the center, which produces a cyclic loop in the skeleton (see figure 4.7b). From this, the corn cob detection problem is converted to a loop detection problem. The cyclic loops are detected by removing all the branches (see figure 4.7c) from the skeleton. The branches are detected using the degree of the nodes. A node connected to a branch will have only one connected edge. A node in a loop always has two connected edges, making the node's degree equal to 2.

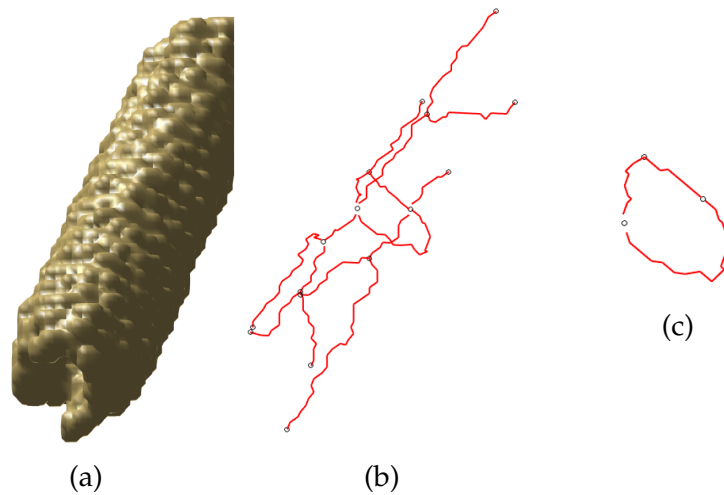


Figure 4.7: Example (a) corn cob, (b) skeleton of the corn cob represented with graphs, (c) cyclic loop extracted from the graph.

Loop detection cannot be the only parameter used to classify the corn cob, because other scenarios can form a cyclic loop leading to false detection. When

corn cobs are fully intact, looking from the centroid of the loop, there is an outer loop and inner loop. Figure 4.8 shows the cross-sectional slice extracted from the corn cob aligned with the loop, with an inner and outer circle. With the corn cob detection problem, the second stage of confirmation is done by detecting inner and outer loops. Usually, fully intact corn cobs resemble a cylinder. The volume of the corn cob can be roughly estimated by measuring their radius and height. The radius is estimated by calculating the distance from the center of mass of the loop to the outer boundary. A tracing algorithm is implemented to determine the cylindrical height. During the tracing, a regression plane is fitted to the cyclic loop. In each plane, a threshold determines the outer boundary, and the radius is noted. Then the plane is moved in both directions along the plane normal direction. At each step, the center of the mass is estimated, and the radius is noted. The tracing continues until the radius observed is greater than a given threshold. In the experiments the threshold is set to observe a 10% increase/decrease in the radius. The distance between these planes is used to determine the cylindrical height. Figure 4.9 shows a cob with the plane at its initial position and planes at the ends of the cob where the intersectional radius varied too much.

4.3.1 Results

This algorithm is tested on two mini-round bale sets. Figure 4.10 shows the 3D view of the two bales and the corn cobs extracted from them using this procedure. Table 4.3 shows the estimated volume of the extracted corn cobs and the deviation from the true volume for the two bale sets. Here true volume of the corn cob is estimated by manual inspection. From the table it can be clearly observed that

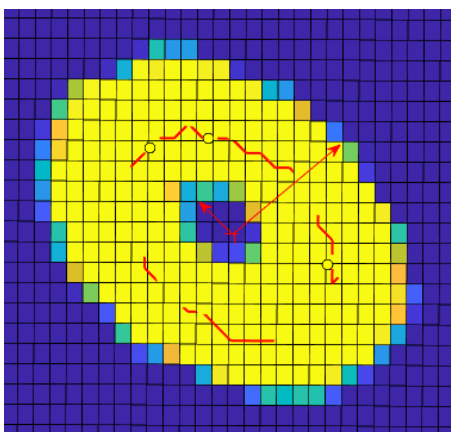


Figure 4.8: 2D cross-sectional image of cyclic loop with arrows pointing the two distances which we measure

bale # 2 provides better accuracy compared to bale # 1. This is mainly because one of the corn cobs present in bale # 1 is not exactly cylindrical in shape, which can be observed in figure 4.10b.

Table 4.3: Volume of corn cobs extracted from the test bales

	Total Volume	Deviation from True Volume
Bale Set # 1	18.07 cubic inch	2.50 cubic inch
Bale Set # 2	20.07 cubic inch	1.33 cubic inch

4.4 Discussion

This chapter presented several 3D image analysis strategies to extract the volume and position information of rocks, soil clumps, and corn cobs present in a corn stover bale. The results show that the tactics presented for segmentation and volume estimation provide adequate accuracy. Using skeletons to identify corn cobs offers a unique advantage as the developed technique efficiency doesn't change much in the presence of moisture content or ash content.

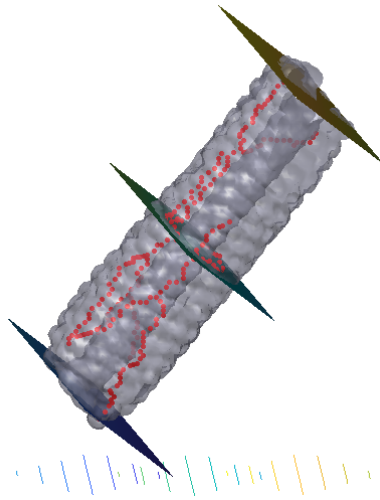


Figure 4.9: A corn cob with the plane at its initial position and planes at the ends of the cob where the intersectional radius decreased by more than 10%.

Further research is required to devise a more efficient and optimized detection model. There are a few limitations with the corn cob detection algorithm, as the algorithm doesn't provide accurate results when the shape of the corn cob is not intact. This can be observed for the bale shown in 4.10a-it's volume estimate was less accurate, but it can also be observed in 4.10b that one of the cobs is missing several kernels. Future research goals should include optimizing the model to differentiate between a loop formed with a corn cob and a fully intact corn stalk. The algorithm should be modified to detect the broken corn cobs by incorporating corn cob texture information. In the future, capturing the required information using morphological processing with different structuring elements should be explored.

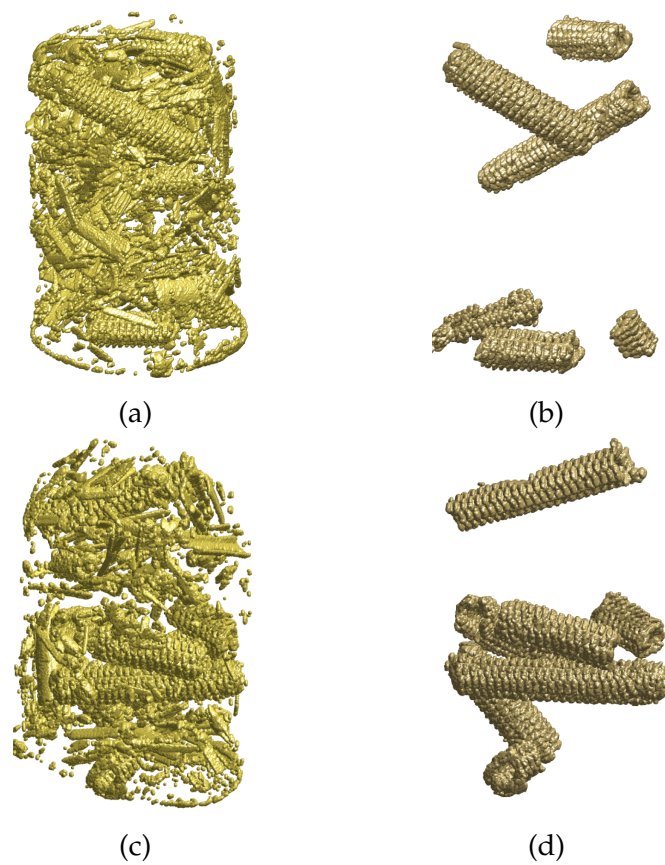


Figure 4.10: (a) baleset # 1, (b) corn cobs extracted from baleset #1, (c) baleset # 2 (d) corn cobs extracted from baleset #2. Note that one of the three cobs at the bottom of (b) has lost much of its material.

CHAPTER 5

THE SPARSE VIEW IMAGE RECONSTRUCTION PROBLEM

In the previous chapter, we presented 3D image analysis techniques to segment and estimate the volume of different tissue contents – rocks, soil clumps, and cobs – present in a corn stover bale. The results show that X-ray CT with image analysis techniques can provide the necessary information about the content of the corn stover bale with high precision. However, traditional X-ray CT algorithms require a large number (N) of projections acquired over a full angular range, i.e., $0 < \theta < 2\pi$, to reconstruct with adequate quality. Generally, the value for N varies with the application, but it is usually high. For example, the mini-round bale reconstruction shown in chapter 4 was created using 720 projections.

Though computational time to reconstruct using image reconstruction algorithms is largely insignificant, collecting a large number of projections will increase the acquisition time, limiting the practicality of using X-ray CT at the biorefinery. For commercial sustainability of the biorefinery, X-ray CT technology needs to reconstruct and provide the volumetric content information in real-time. So, it is essential to understand the performance of image reconstruction methods with limited projection data. This is known as the sparse view reconstruction problem.

Figure 5.1 shows the schematic illustration of data acquisition between a conventional CT framework and a sparse view CT framework. After acquiring X-ray projections, a mathematical reconstruction algorithm is applied to extract the cross-sectional slice information of the 3D object. These reconstruction algorithms are generally divided into two categories: analytical and iterative reconstruction methods. This chapter shows the performance of analytical reconstruction methods followed by a few selected iterative reconstruction methods in a sparse view framework.

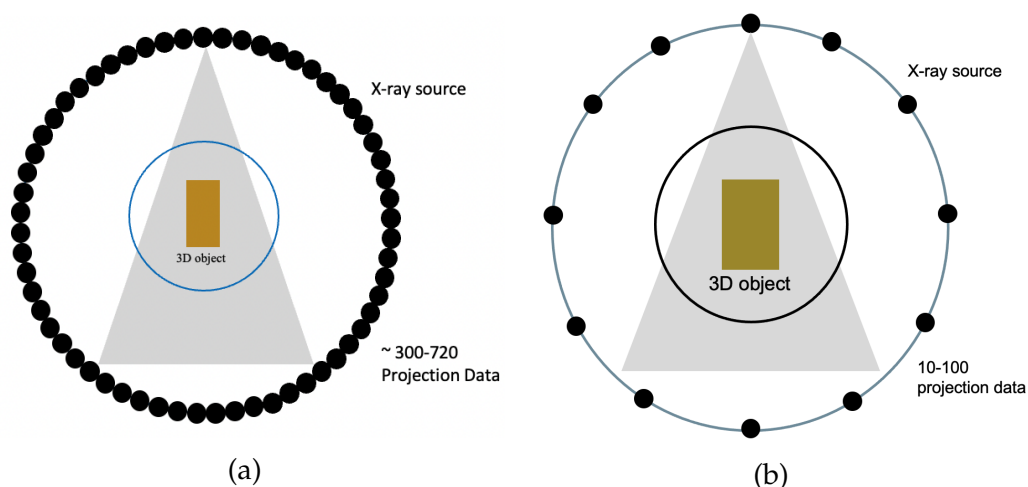


Figure 5.1: Schematic illustration of data acquisition in (a) conventional CT framework and (b) sparse view CT framework.

The performance of the reconstruction methods is evaluated in both qualitative and quantitative fashion using a 3D phantom. Figure 5.2a shows the 3D phantom used in this chapter for evaluation. Figure 5.2b shows the 2D cross-sectional slice taken from the 3D phantom used for qualitative analysis. For qualitative comparison, the variation in the reconstruction quality with the number of projections is demonstrated using a 2D cross-sectional slice. For quantitative comparison, the Pearson correlation coefficient and computational times of each method are

considered. The Pearson correlation coefficient provides a measure of linear correlation between the reconstructed and original image. The computation time shows the practicality of the reconstruction methods.

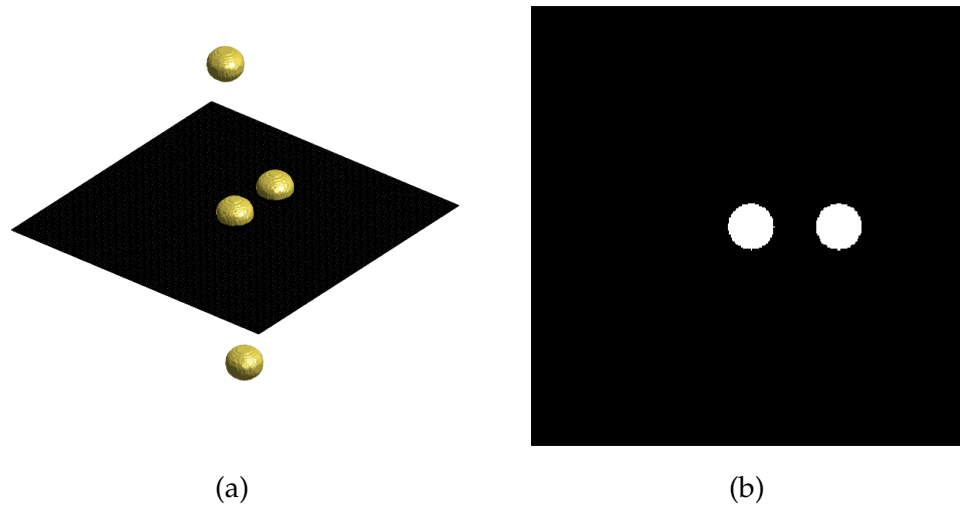


Figure 5.2: (a) Phantom used for the evaluation, (b) A 2D phantom used for qualitative analysis.

Not all applications require complex reconstruction methods. For example, we only need to know the quantity, approximate location and volume when detecting rocks, metal contaminants, and soil clumps present in the corn stover. In the second section of this chapter we propose a simple and computationally less intensive approach for such applications that uses only two X-ray projections. In this chapter, along with understanding the performance of reconstruction methods with limited projections, computation times of these image reconstruction methods and the two-projection method with different input sizes are studied to understand the variation in computation load with increase in input size.

To study the performance of image reconstruction methods in the sparse view framework, we use the tomographic iterative GPU-based reconstruction (TIGRE),

[56] toolbox. TIGRE is a MATLAB/Python-based CUDA toolbox, which supports both cone-beam and parallel-beam X-ray sources and supports flexible CT geometry (arbitrary axis of rotation, offsets, pixel sizes). In this work, the TIGRE toolbox with cone-beam computed tomography (CBCT) geometry is used to extract projections. Figure 5.3 shows the CBCT geometry. The TIGRE toolbox provides access to over ten iterative reconstruction methods in addition to classic analytical algorithms, like the filtered back-projection (FBP) algorithm and Feldkamp, Davis, and Kress (FDK) algorithm. All the experiments in this work are performed on a windows machine with 16 GB RAM and a 4 GB Nvidia GeForce graphic processor, with compute capability of 6.1.

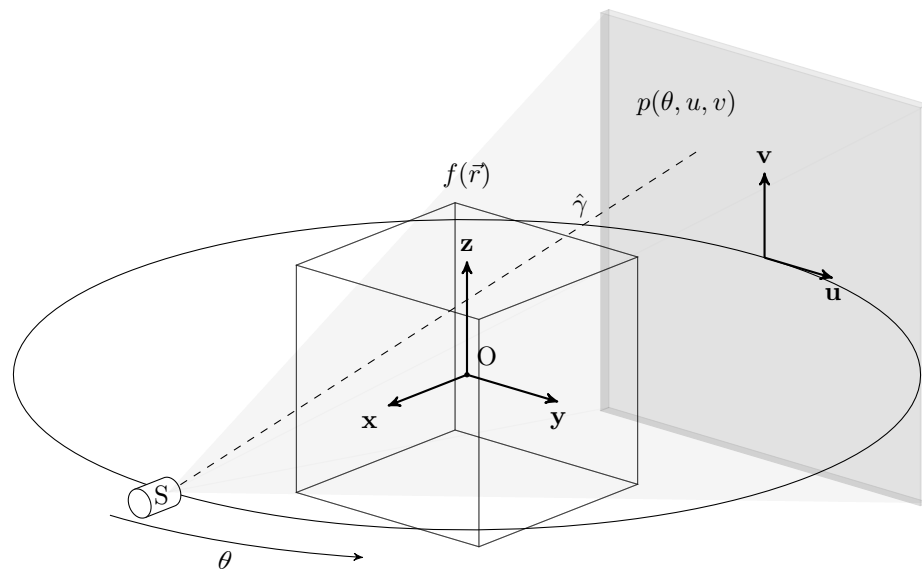


Figure 5.3: Geometry of CBCT [43]

5.1 Evaluation of Image Reconstruction Methods

5.1.1 Analytical Reconstruction Methods

The most widely used analytical reconstruction method across all CBCT modalities is the Feldkamp, Davis, and Kress (FDK) algorithm [57]. The popularity of the FDK algorithm is mainly because of its computational efficiency and numerical stability. However, when there are errors in the data or the amount of data is limited, the FDK algorithm often behaves poorly. This is because FDK provides an analytical approximation of straight path integrals in continuous spaces. To create a good quality reconstruction with fewer artifacts, many projections from different angles need to be acquired over a full angular range, i.e., $0 \leq \theta \leq 2\pi$.

Figure 5.4 shows FDK reconstructed images of the 2D phantom as the number of projections is varied. As the number of projections used for the reconstruction decreases, the streak artifacts become more predominant. The streak artifacts observed in the projections lower the quality of the reconstruction and would interfere with subsequent processing and evaluation.

Figure 5.5a shows the Pearson correlation coefficient comparing the true phantom and the reconstructed phantom versus the number of projections. The plot shows that the correlation between true and reconstructed phantom drops with the number of projections. A drastic drop can be observed after 100 projections. It can also be observed in figure 5.4 that the similarity between the two images is dropped and can be easily observed when the number of projections used for the reconstruction is less than 100. In practice FDK will require a large number of pro-

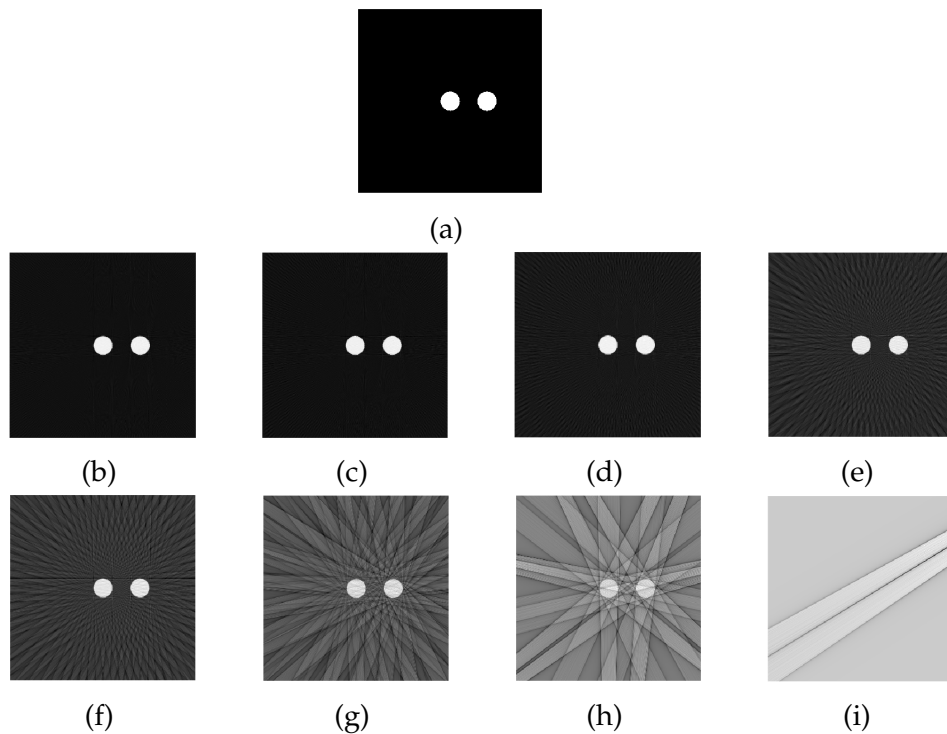


Figure 5.4: (a) A 2D phantom. 2D phantom reconstruction with FDK using (b) 359 projections, (c) 274 projections, (d) 179 projections, (e) 89 projections, (f) 71 projections, (g) 23 projections, (h) 11 projections, (i) 3 projections.

jections, around 100 projections, to reconstruct the 3D volume with required image quality. Figure 5.5b shows the computation time in seconds versus the number of projections. A decrease in the number of projections reduces the computational time. However, the acquisition time is directly proportional to the number of scans. So, FDK will not be a good choice to use for reconstruction at the biorefinery.

5.1.2 Iterative Reconstruction Methods

In contrast to analytical approximation, the image reconstruction problem can also be solved by optimizing a linear model. In the literature, these algorithms are referred to as iterative reconstruction methods. These algorithms are shown

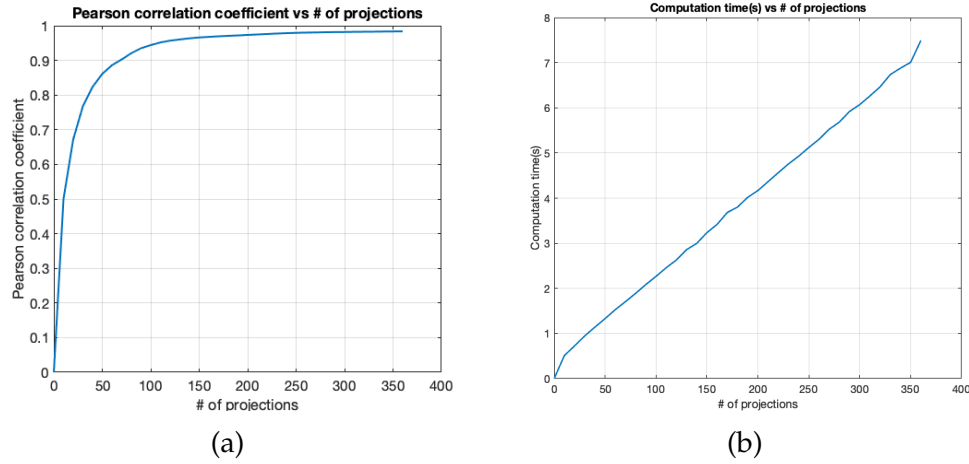


Figure 5.5: (a) Pearson correlation coefficient, (b) computation time in seconds versus number of projections for the FDK algorithm.

to improve the reconstruction quality, especially when the data is noisy and/or limited. Iterative reconstruction algorithms in CT generally solve a linearized model

$$Ax = b + \tilde{e}, \quad (5.1)$$

where $x \in \mathbb{R}^{N_{\text{voxels}}}$ is a vector representing the voxels of the 3D image, $b \in \mathbb{R}^{N_{\text{pixels}}}$ is a vector representing the measured pixels in the detector. Here, A is a linearized model matrix that describes the behavior of the CT system, and \tilde{e} represents the errors from measurements and other linearized errors from approximation. The problem in equation 5.1 can be minimized as

$$\hat{x} = \underset{x}{\operatorname{argmin}} \|Ax - b\|^2 + R(x), \quad (5.2)$$

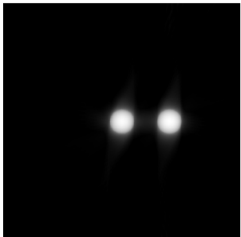
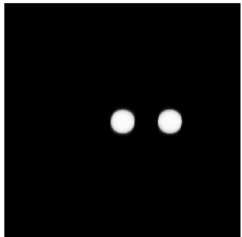
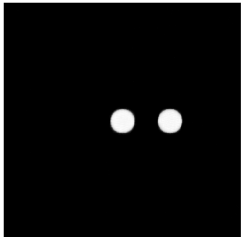
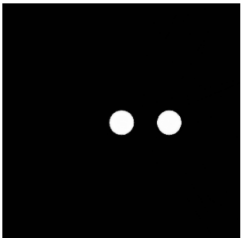
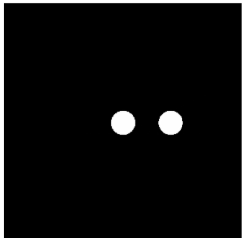
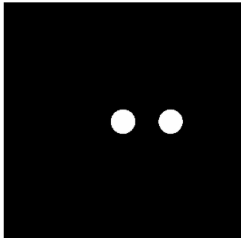
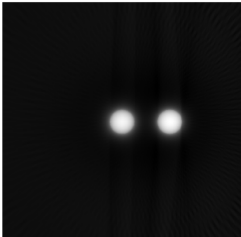
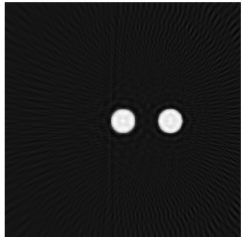
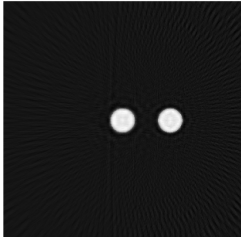
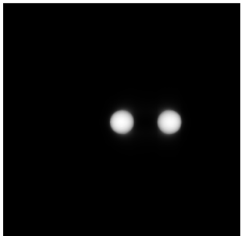
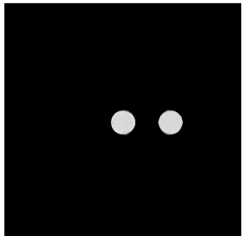
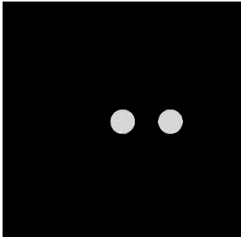
where $R(x)$ is the optional regularization function. Numerous iterative reconstruction methods exist in the literature, using different methodologies to solve equation 5.2. In this work, we consider the ordered subset-simultaneous algebraic

reconstruction technique (OS-SART), the simultaneous algebraic reconstruction technique - total variation (SART-TV), the conjugate gradient least squares (CGLS) method, and the maximum likelihood expected maximization (MLEM) method [58, 59, 60]. These methods were selected to represent a broad range of iterative reconstruction methods. The OS-SART represents the algebraic reconstruction techniques. Sometimes solving with a regularization function can provide better results than just solving the data constraint. SART-TV represents the set of reconstruction algorithms that optimize through a regularization function. Then we have CGLS, which as the name suggests optimizes the function based on the least-squares problem using the conjugate gradient method. At last, MLEM represents the statistical iterative reconstruction methods.

The reconstruction quality with iterative methods relies on two parameters, the number of projections and the number of iterations. We evaluate the performance of the iterative reconstruction algorithms OS-SART, SART-TV, CGLS, and MLEM under three cases: one with a moderately higher number of projections (71 projections, Table 5.1), the second with a significantly lower number of projections (11 projections, Table 5.2), and the last, reconstruction with only two projections (Table 5.3). For each scenario, reconstruction is calculated with 5, 30, and 50 iterations. Here, we mainly focused on the performance of iterative reconstruction methods when the number of projections is less than 100, because as observed in section 5.1.1, the FDK algorithm behaves poorly only after reducing to 100 projections. Tables 5.1, 5.2, and 5.3 show the reconstruction quality of the iterative reconstruction algorithms OS-SART, SART-TV, CGLS, and MLEM algorithms for a phantom. From the results, it can be concluded that all algorithms provide a

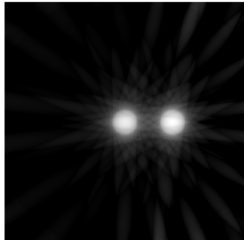


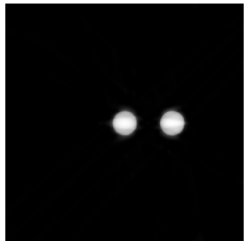
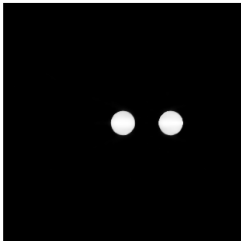
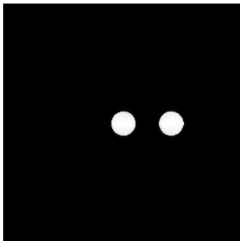
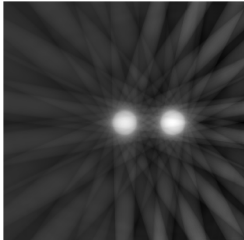
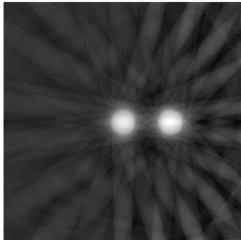
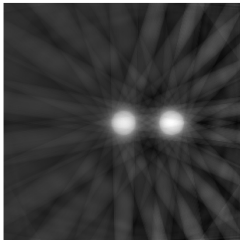
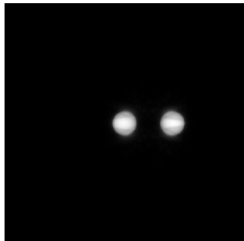
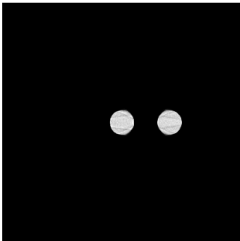
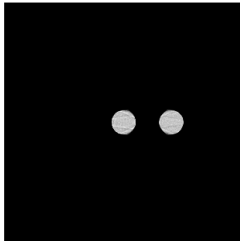
satisfactory image quality when an adequate number of projections are available for reconstruction. However, for OS-SART and CGLS with a drop in the number of projections the reconstruction quality also drops and requires more iterations to increase reconstruction quality. Only the SART-TV and MLEM algorithms show a satisfactory quality even with a lower number of projections and iterations.

Table 5.1: Reconstructed images based on iterative reconstruction methods using 71 projections

Algorithm	5 iterations	30 iterations	50 iterations
OS-SART			
SART-TV			
CGLS			
MLEM			

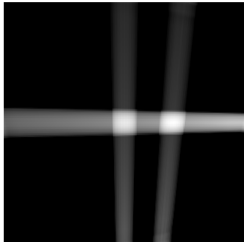
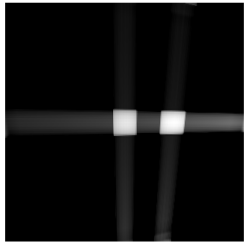
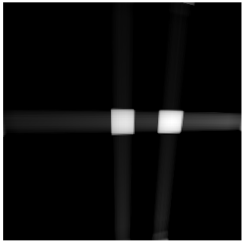
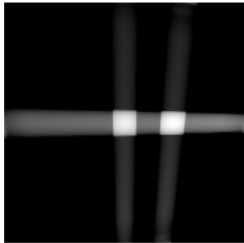
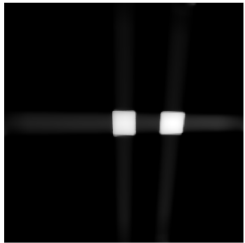
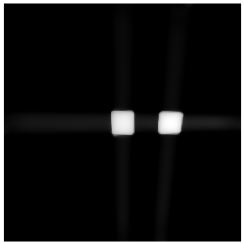
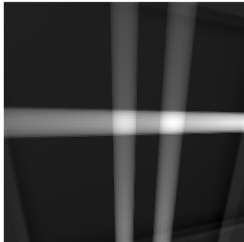
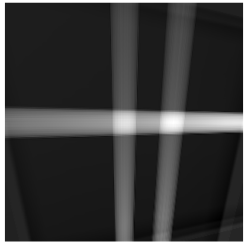
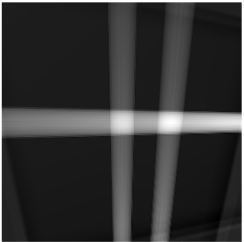

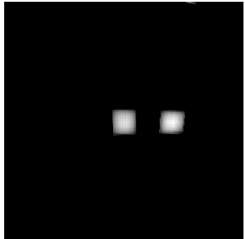
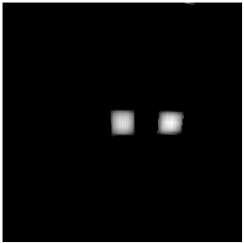
To present the performance of iterative reconstruction methods quantitatively,

Table 5.2: Reconstructed images based on iterative reconstruction methods using 11 projections

Algorithm	5 iterations	30 iterations	50 iterations
OS-SART			
SART-TV			
CGLS			
MLEM			

we use the Pearson correlation coefficient and computation times. Figures 5.6a, 5.7a, and 5.8a show the Pearson correlation coefficient for the iterative reconstruction methods versus the number of iterations utilizing 71, 11, and 2 X-ray projections. The correlation plots show that all algorithms perform well when the number of projections is high, provided the reconstruction algorithms are allowed to run for a sufficient number of iterations to optimize the reconstruction quality.

Table 5.3: Reconstructed images based on iterative reconstruction methods using 2 projections

Algorithm	5 iterations	30 iterations	50 iterations
OS-SART			
SART-TV			
CGLS			
MLEM			

Here the SART-TV algorithm offers better quality with fewer iterations compared to the MLEM, OS-SART, and CGLS algorithms. A similar trend can be observed from table 5.1 that the SART-TV provides a higher reconstruction quality at 5 iterations compared to other algorithms.

When the number of projections drops further, MLEM offers better reconstruc-

tion quality with fewer iterations than other algorithms. This can be observed in figures 5.7a and 5.8a where MLEM reaches an optimum correlation value quicker than other algorithms. SART-TV trails MLEM, but requires more iterations to achieve the optimum results. The OS-SART algorithm tends to provide a high reconstruction quality, but it requires more iterations to increase the reconstruction quality. CGLS reaches an optimum value and doesn't improve any further even with an increase in the number of iterations.

Moreover, the practicality of the algorithm does not just rely on the reconstruction quality, computation time also play a crucial role. Figures 5.6b, 5.7b, and 5.8b show the computation times of the iterative algorithms under study versus the number of iterations. From the plots, it is observed that an increase in the number of iterations increases the computation times. Between MLEM and SART-TV, MLEM is more applicable for practice as it provides high reconstruction quality with lower time complexity. The computation time of the SART-TV algorithm is significantly greater than the other algorithms.

The evaluation shows that the iterative algorithms are capable of reconstructing the 3D image with high quality in the sparse view framework. However, with fewer projections, the iterative algorithms require more iterations to achieve good quality, increasing overall computational time. The MLEM algorithm is more practical to use at the biorefinery for complex reconstruction problems. Since MLEM is a statistical reconstruction method, prior knowledge can be included using probabilistic models to achieve better reconstruction quality.

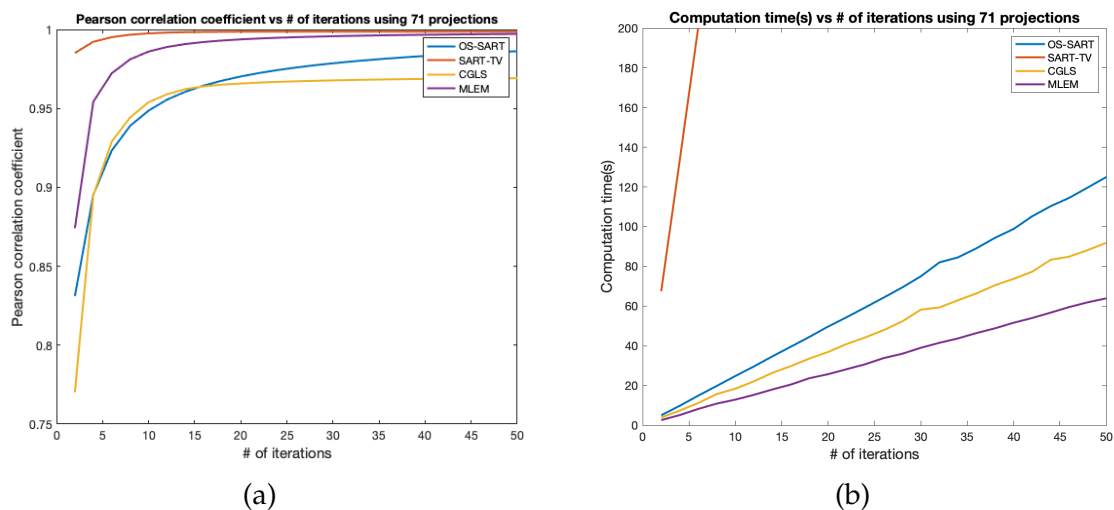


Figure 5.6: (a) Pearson correlation coefficient, (b) computation time in seconds versus number of iterations for OS-SART, SART-TV, CGLS, MLEM algorithms using 71 projections.

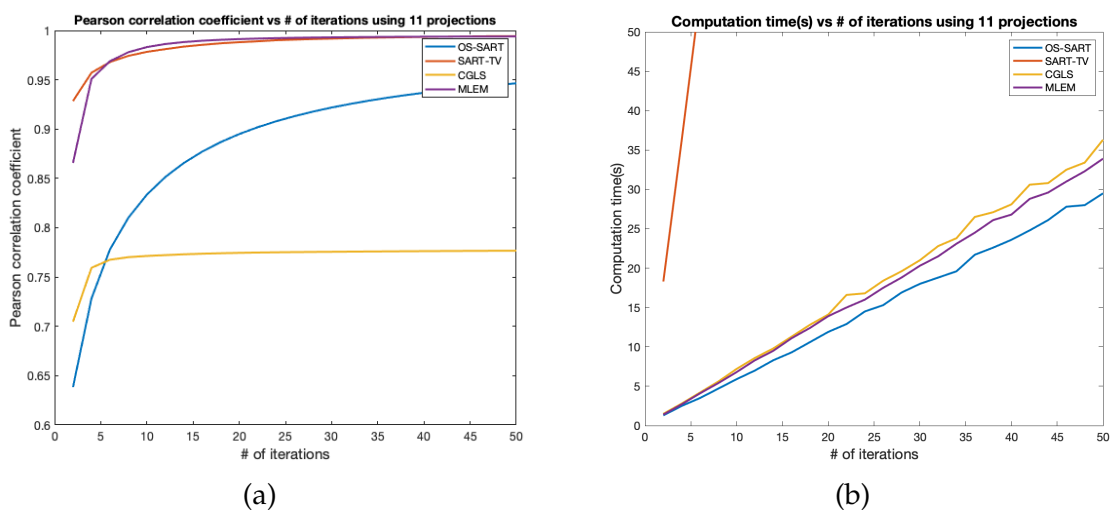


Figure 5.7: (a) Pearson correlation coefficient, (b) computation time in seconds versus number of iterations for OS-SART, SART-TV, CGLS, MLEM algorithms using 11 projections.

5.2 Two-Projection Method

Not all applications require complex reconstruction methods to reconstruct the 3D volume from X-ray projections. For example, for rocks, metal contaminants,

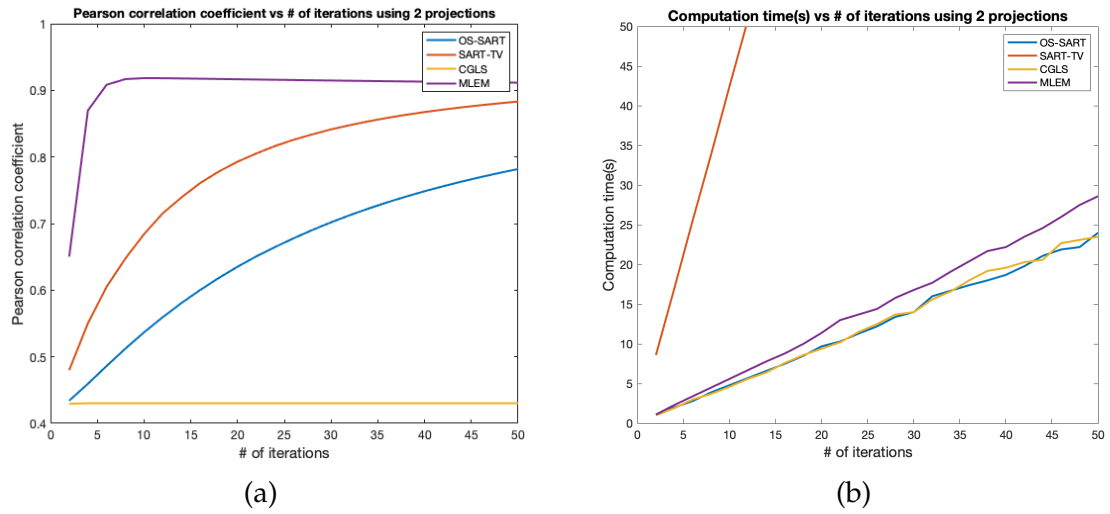


Figure 5.8: (a) Pearson correlation coefficient, (b) computation time in seconds versus number of iterations for OS-SART, SART-TV, CGLS, MLEM algorithms using 2 projections.

and soil clump detection, one only needs to know approximate location and volume of the content; it is not required to know all the fine shape details. For such applications, we propose a mathematical approach in this section that uses two X-ray projections to reconstruct the 3D volume with high precision.

Figure 5.9 describes the complete architecture of the two-projection method. The entire process can be divided into two phases. First, both projections are extrapolated back into 3D space by elongating the “on” pixels in the projection along the tomographic angle until the 3D volume is equivalent to the detector dimensions (see figure 5.9c). The two volumes extrapolated from projections are aligned together (see figure 5.9d), and their intersection is calculated (see figure 5.9e). The intersected volume represents the volume of materials like rocks and metal contaminants present in a corn stover bale. For all the experiments in this work, the detector dimensions are set to 512 x 512. The reconstructed volume will

be $512 \times 512 \times 512$, which will reduce the complexity in the later stages.

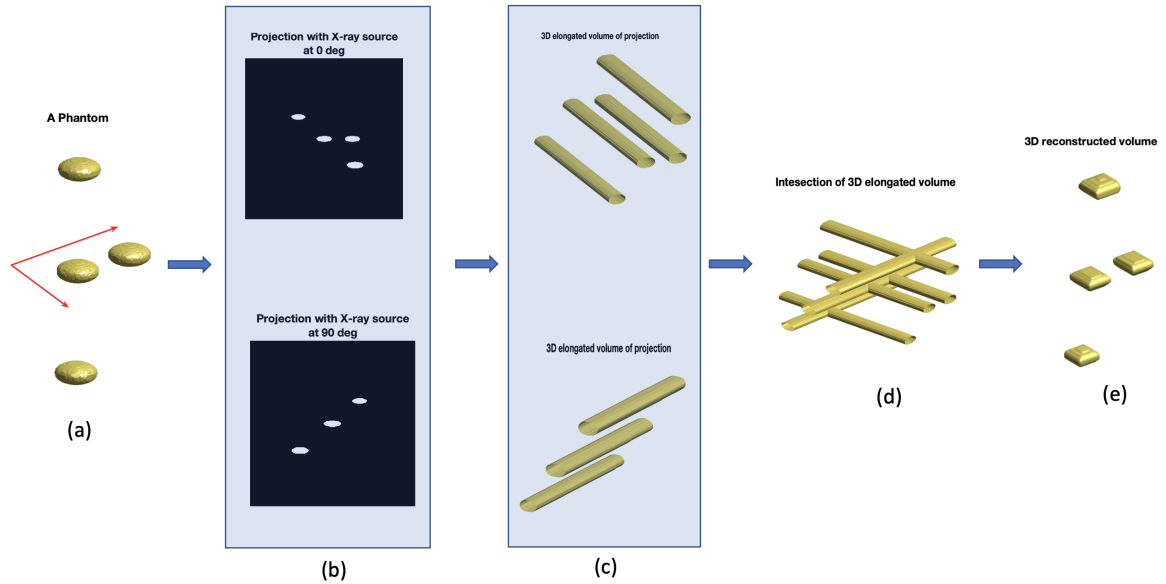


Figure 5.9: Architecture of the two-projection method. (a) The phantom represented in 3D volume, (b) the 2D X-ray projections taken at two tomographic angles, (c) the extrapolated volume for each projection back in 3D, (d) the aligned extrapolated volumes, (e) the intersection of the two aligned volumes.

Analysis with a Phantom

Earlier, we discussed the challenges associated with analytical and iterative reconstruction methods when using fewer X-ray projections. This section will provide a detailed quantitative and qualitative analysis of the two-projection method using a phantom (see figure 5.2a). Several experiments were conducted to evaluate the two-projection method. Here maximum position deviation and volume accuracy are considered for the quantitative analysis.

In our experiments, first we will evaluate the technique on the simple phantom by considering a 90-degree angular separation between two X-ray sources. Then

we change the angular separation between the two X-ray sources to 135, 75, 60, 45, 30, and 15 degrees to observe the impact on the two-projection method performance with an increase/decrease in the angular separation. The angle between two projections can be arbitrary. In our experiments, one projection is always set to the tomographic origin (0 degrees).

As stated previously, we first start with a 90-degree separation with, $\theta_0 = 0$ deg and $\theta_1 = 90$ deg. Figure 5.10a shows the 2D cross-section slice from the rock phantom shown in figure 5.2a. Figure 5.10b shows the 2D-cross sectional slice from the reconstructed phantom when using two projections with 90-degree separation. The figure shows that the two-projection method can reconstruct the objects of interest without any streak artifact. Since only two projections with 90-degree separation are used, the estimate takes on a square instead of a circular shape, where the sides of the square are the diameter of the circle. The volume estimates from the two-projection method are always greater than the true volume. The discrepancy is mainly because the circle always can be inscribed in the reconstructed square, and the angle between the two X-ray sources and the X-ray acquisition geometry configuration determine how much area is outside the circle.

Table 5.4 shows the quantitative results for the estimated rock phantom, shown in figure 5.9a. Figure 5.9e shows the reconstructed volume using the two-projection method with 90-degree separation. The two-projection method with 90-degree separation provides a volume estimate with 375.5% accuracy and shows a position deviation of around 0.018 inches. The 0.018 position deviation is insignificant when part of a reconstructed 7inch x 7inch x 12inch rectangular volume.

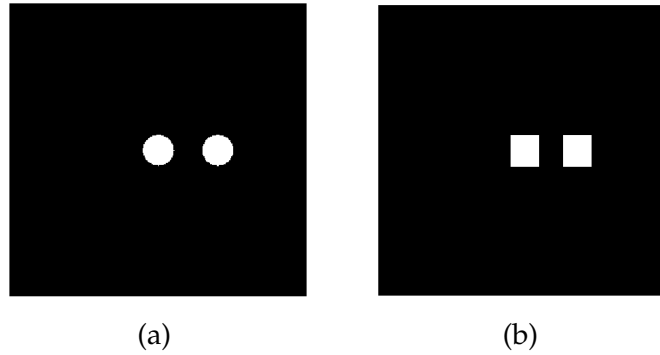


Figure 5.10: (a) 2D cross-section slice from the rock phantom, (b) Estimated 2D cross-section slice from the rock phantom with 90-degree separation.

Table 5.4: Quantitative analysis with simple phantom with angle separation 90-degree

True Volume	Estimated Volume	Volume Accuracy (%)	Average Position Deviation (")
148672	558336	375.5	0.018

Figure 5.11 shows a circle that is enclosed by the reconstructed square. The figure shows the discrepancy between the area of the circle and the reconstructed square. The area of the circle with diameter d is

$$Area_{circle} = \frac{\pi d^2}{4}. \quad (5.3)$$

Since the area of the square is d^2 , we know

$$Area_{circle} = \frac{\pi}{4} * Area_{square}. \quad (5.4)$$

The $\frac{\pi}{4}$ represents a scaling factor which can be used to correct the area estimate when the angle separation between two X-ray sources is 90 degrees.

In the real world, we may not always be able to use the 0 and 90-degree pair,

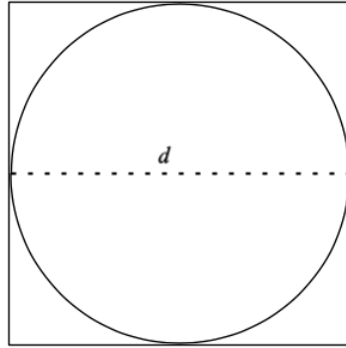


Figure 5.11: Reconstructed square encloses the object circle.

because the camera acquisition system at the biorefinery may have other geometrical constraints. We explored the problem by changing the angle between two projections to 135, 75, 60, 45, 30, and 15 degrees. Figure 5.12 shows the reconstructed 2D cross-sections of a circle when the angular separation is greater/less than 90-degrees. When the angle separation between the two X-ray sources is not 90 degrees, the reconstruction becomes a rhombus instead of a square. The scaling factor shown in equation 5.4 needs to be adjusted to include the angle to correct for the error in these cases. Here we generalize the problem and equation 5.4 by considering the area of the rhombus. Figure 5.13 shows the rhombus representing the reconstruction of the circle with angle separation $\theta = |\theta_1 - \theta_2|$ and side length l . Using trigonometric rules we can see that the diameter of the circle and side of the rhombus are related by

$$\cos(90 - \theta) = \frac{d}{l}. \quad (5.5)$$

The area of the rhombus can be calculated using the side and the angle using

$$Area_{rhombus} = l^2 \sin(\theta). \quad (5.6)$$

From equation 5.5 $l = \frac{d}{\cos(90-\theta)}$. Since $\cos(90-\theta) = \sin(\theta)$, the area of the rhombus shown in equation 5.6 can be represented as

$$Area_{rhombus} = \left(\frac{d}{\sin(\theta)} \right)^2 \sin(\theta). \quad (5.7)$$

The calculated area of the circle will still be $\frac{\pi d^2}{4}$, so

$$Area_{circle} = Area_{rhombus} * \frac{\pi \sin(\theta)}{4}. \quad (5.8)$$

This information can be used to create an offset factor to correct for the method when reconstructing a rhombus instead of a circle.

The assumptions used to this point treat the X-rays as if they were parallel, but in reality we are using a CBCT configuration. The size of the object on the detector will be larger than the size of the physical object. The offset factor calculated from equation 5.4 will not be enough to correct the estimated volume. Figure 5.14 shows the X-ray geometry configuration in 2D where the circle with diameter d is projected on to the detector. Here d_1 represents the distance from the source to the detector, d_2 represents the distance from the source to the center of the object, and d_p represents the size of the object in the projection. Using similar triangles we observe that,

$$\frac{d_1}{d_2} = \frac{d_p}{d}. \quad (5.9)$$

The side of the rhombus in equation 5.7 is really d_p not d , so since $d_p = \frac{d_1}{d_2} * d$, the area of the rhombus is

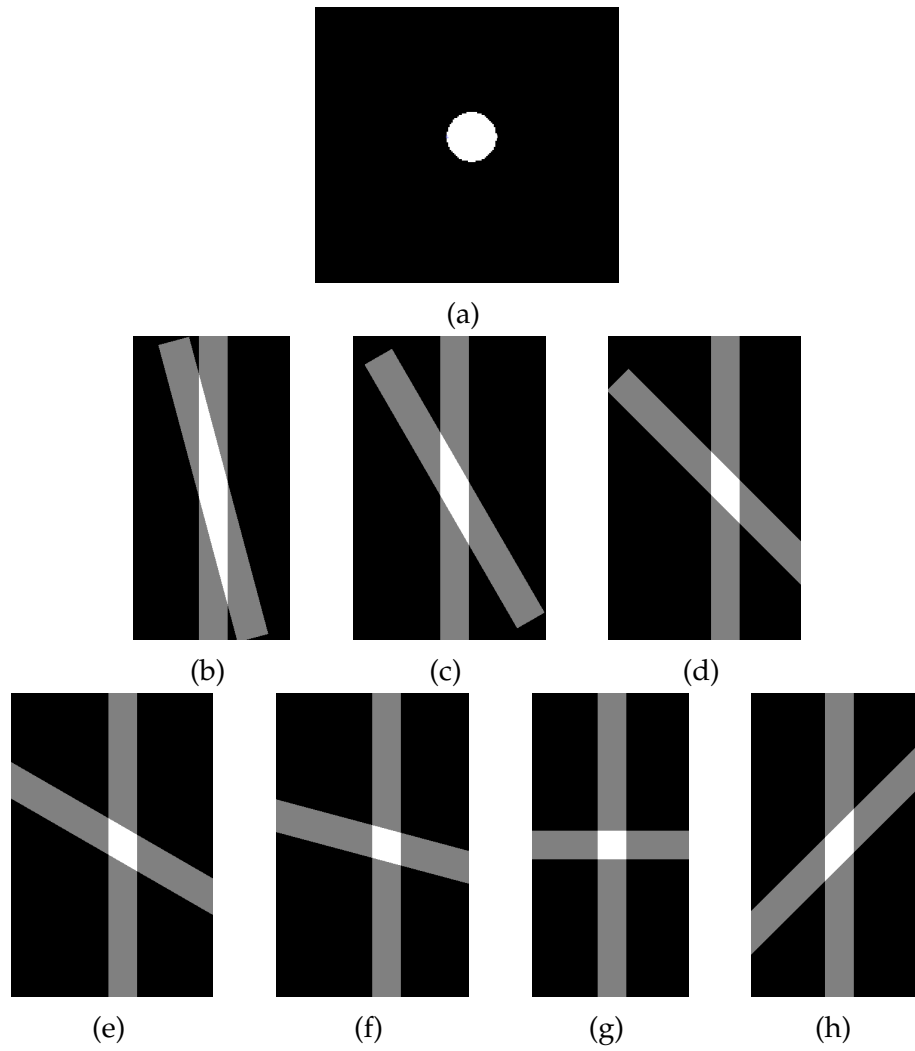


Figure 5.12: (a) 2D Phantom. Projections with (b) 15 degree, (c) 30 degree, (d) 45 degree, (e) 60 degree, (f) 90 degree, and (f) 135 degree separation.

$$Area_{rhombus} = \left(\frac{d_1}{d_2}\right)^2 \left(\frac{d}{\sin(\theta)}\right)^2 \sin(\theta). \quad (5.10)$$

The calculated area of the circle will still be be $\frac{\pi d^2}{4}$, so

$$Area_{circle} = Area_{rhombus} * \left(\frac{d_2}{d_1}\right)^2 * \frac{\pi \sin(\theta)}{4}. \quad (5.11)$$

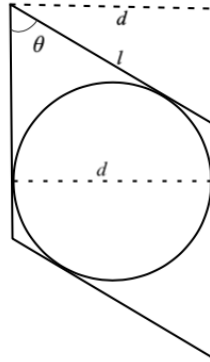


Figure 5.13: Circle inscribed in a rhombus.

When extending from 2D area to 3D volume the height of the rhomboid also needs to be taken into consideration producing

$$Volume_{circle} = Volume_{rhombus} * \left(\frac{d_2}{d_1}\right)^3 * \frac{\pi \sin(\theta)}{4}. \quad (5.12)$$

This information can be used to calculate a scaling factor value that will correct for the X-ray geometry configuration used in the experiment.

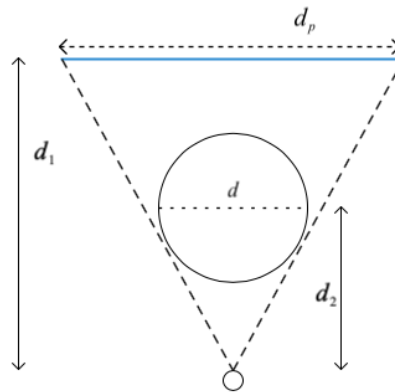


Figure 5.14: Fan beam X-ray acquisition geometry.

Table 5.5 shows the offset factor from equation 5.12 at various angle separations when $d_1 = 805.48 \text{ mm}$ and $d_2 = 539.69 \text{ mm}$. Here the d_1 and d_2 are directly taken

from the X-ray configuration used for scanning, which works for an object at the center of the bale. We ran the experiment for these angles. Table 5.6 shows the measured reconstructed volume, and the corrected volume after applying equation 5.12. Most of the estimates are within 6% error. The overestimates observed in the table are mainly from excessive border voxels being counted. When there are multiple objects, the d_2 value will vary. For each object of interest, the algorithm must first estimate the position and adjust the d_2 value by estimating the distance from the center of the entire body to the source. The estimated d_2 values help to calculate the offset factor for a given object.

For narrow-angle separations, the rhombuses are long and narrow. Without proper padding, the ends can get chopped. Figure 5.15 shows the reconstructed volume with the cut-off ends when the angle separation is 15 degrees. Proper care should be taken while padding the volume to avoid any such errors.

Table 5.5: Offset factor at each angular separation

Angle	Volume Offset factor
135	0.1914
90	0.2707
75	0.2615
60	0.2345
45	0.1914
30	0.1354
15	0.0701

5.3 Computation Times

Currently, all the experiments in this work were conducted with fixed dimensions and for a mini-round bale. However, at a biorefinery we will be working

Table 5.6: Quantitative analysis with simple phantom with volume: 148672 voxels

Angle Separation	Measured Volume	Corrected Volume	Volume Accuracy (%)
135	558336	151141	106.3
90	604386	158046	101.6
75	673854	158018	106.2
60	822224	157373	105.8
45	1167160	158033	106.3
30	2176704	152586	102.6
15	822224	157373	105.8

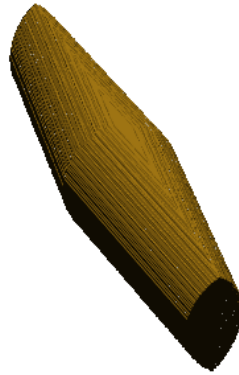


Figure 5.15: Reconstructed volume of a sphere with 15 degree separation without proper padding.

with larger bales of size $3' \times 3' \times 4'$. This increases the resultant dimensions of the input data, which the reconstruction algorithms need to process. The resulting computation time will change with an increase in the dimensions of the input size. Synthetic samples with different input dimensions were taken to study the time complexity of the reconstruction algorithms. The two-projection method in section 5.2 was run on a CPU, whereas the other reconstruction methods described in section 5.1 were run on GPUs. Figure 5.16 shows the time complexity plot. Where the x-axis represents the dimensions of the input volume (size \times size \times

size). Even with the CPU/GPU difference, the two-projection method was significantly faster. However when the input data size is greater than $512 \times 512 \times 512$, the two-projection method's computational complexity increases drastically. This is mainly because the algorithm implemented uses a MATLAB built-in function called "repmat" to elongate the volume. In the future, the time complexity with large data sizes need to be reduced by avoiding the usage of built-in MATLAB functions. The time complexity of the MLEM shows that the algorithm is suitable for complex reconstruction problems at the biorefinery.

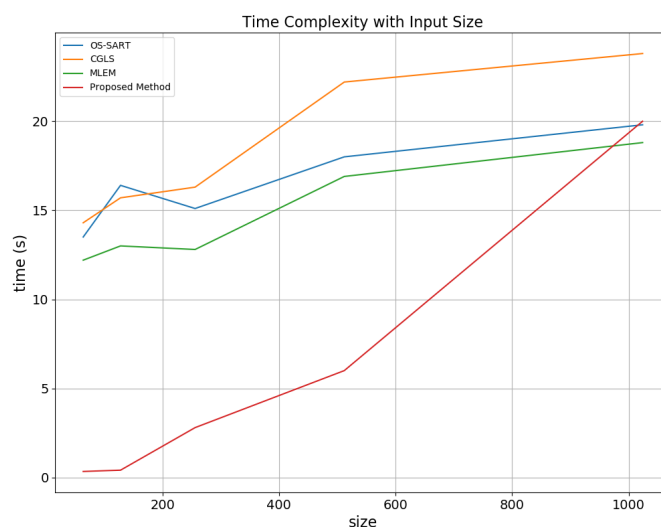


Figure 5.16: Time complexity with increase in input dimensions for OS-SART, CGLS, MLEM & the proposed two projection method.

5.4 Discussion

This chapter presented the performance of reconstruction methods when the number of projections is smaller than used in commercial CT imagery. The it-

erative reconstruction methods like MLEM and SART-TV provide an acceptable reconstruction quality with fewer projections. However, the SART-TV algorithm requires a large computation time. From this work, we can conclude that the MLEM method will be suitable for reconstruction algorithms for the complex reconstruction problems where we reconstruct the corn cobs or stalks volume from the bale, which will be discussed in chapter 6.

The proposed two-projection method runs quicker and provides a high-quality reconstruction, suitable for simple problems like volume and position estimation of rocks, metal contaminants, and soil clumps present in the bale. There are two kinds of errors which will be observed in the reconstructed volume with two projection method. First, false phantoms and second intersection of two volumes. Since only two projections are used when multiple objects are in the same neighborhood they can create false phantoms. The other possible error occurs when two objects are in a very close neighborhood and the projections taken couldn't tell the difference, it is reconstructed as a single object. In the future, these need to be addressed by accounting for the intensity value observed in the projections.

In all the experiments, the pixel pitch of the detector and the size of each voxel are made equal, i.e., 1 mm . Future studies should evaluate the performance when the pixel pitch of the detector and size of each voxel are not equal. Similarly, we need to study how the criteria for volume correction change with the different X-ray geometry configurations. Here, the X-ray geometry configuration has the entire bale in the X-ray source's Field of View (FOV), and the object is projected onto a detector that is larger than the dimensions of the bale. For example d_p shown in figure 5.14 is always greater than d . Future study needs to focus on un-

derstanding what role the X-ray geometry configuration plays in the offset factor. Also, the program needs to be optimized to reduce the time complexity when the input data size is large.

CHAPTER 6

NUMERICAL EVALUATION OF TISSUE CHARACTERIZATION IN A CORN STOVER BALE WITH 3D IMAGE ANALYSIS TECHNIQUES IN A SPARSE VIEW FRAMEWORK

In the previous chapter, we reviewed the performance of several image reconstruction methods with limited projections. We also proposed and provided an evaluation of the two-projection method. The two-projection method and the statistical reconstruction method (MLEM) have shown very high performance with lower time complexity. However, in the previous chapter the performance of the image reconstruction methods was evaluated using a simple phantom. This chapter shows the application of these methods to categorize and provide volumetric estimates of different tissues fractions present in a corn stover bale.

This chapter aims to produce the 3D volume using only a few X-ray projections, then reconstruct different tissue fractions of the bale and classify them accordingly. This chapter also discusses the strategies associated with extracting different tissue fractions. Firstly, we show the application of the two-projection method to segment the higher density materials – rocks, metal contaminants, and soil clumps– present

in the corn stover bale. Secondly, we show the performance of the statistical reconstruction method, MLEM, to reconstruct mainly the corn cobs and stalk nodes present in the bale.

6.1 Detection of Rocks and Metal Contaminants in a Corn Stover Bale

As mentioned in section 4.2, rocks and other metal contaminants in a corn stover bale are detrimental to conversion and production when left unattended. If necessary precautions are not taken, these rocks and other metal contaminants can cause significant damage to the grinding equipment, which can significantly increase equipment wear and downtime. Sparks could be generated in the grinder causing fire hazards [25]. Knowledge about the quantity of this foreign matter and its location within a bale can be used to determine whether the bale should be rejected in part or in whole.

As already stated in section 4.2, rocks or any other metal contaminants have a very high bulk density (2.62 g/cm^3) compared to corn stover biomass (0.15 g/cm^3). High bulk density generally relates to more X-ray photon absorption, which results in higher attenuation. In the X-ray projections, higher attenuation regions are usually represented with high-intensity values. Because of the significant difference between the bulk densities, it is easy to segment the rocks and metal contaminants from corn stover biomass by applying the thresholding technique on the acquired X-ray projections. Thresholding is the most straightforward segmentation technique where each pixel intensity below a given threshold value is represented

with 0, and the rest is represented with 1. Figure 6.1a shows the X-ray projection through a mini-round cylindrical corn stover bale with a diameter of 12.70 *cm* and height of 15.24 *cm*. Synthetic rocks which resemble the shape of pebbles are added to the bale. These rocks are represented with a high pixel intensity value in figure 6.1a. Figure 6.1b shows the same X-ray projection after segmenting the rocks using a simple global thresholding technique.

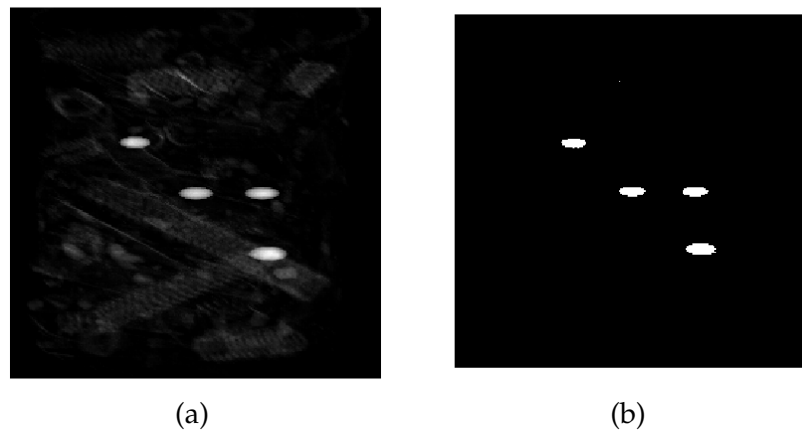


Figure 6.1: An X-ray projection through a corn stover bale showing the four rocks (a) before thresholding, and (b) after thresholding.

After thresholding, the two-projection method presented in section 5.2 is used to reconstruct the 3D volume of the synthetic rocks in the corn stover bale. Figure 6.2 shows the architecture of the rocks and metal contaminants detection problem described in this chapter. The intersected volume shown in figure 6.2e provides the volume estimate for the rocks and other metal contaminants.

In this work, two kinds of synthetic rock samples, smooth pebbles and rough gravel, are considered to test the two-projection method performance. Figures 6.3a and 6.3b show an example of the smooth pebble and rough gravel data used in this work. Smooth pebble rocks are created by considering the shape of an

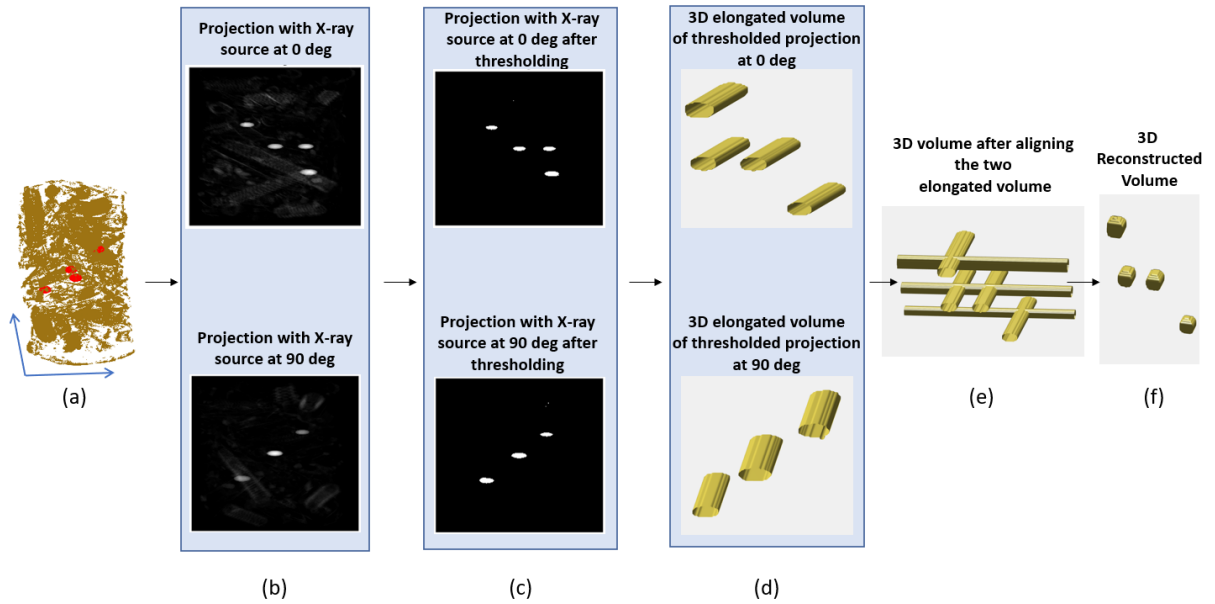


Figure 6.2: Architecture of the rocks and metal contamination detection in a sparse view framework using two-projection method where (a) shows the synthetic rock sample represented in 3D volume with red color, (b) shows the 2D X-ray projections taken at two tomographic angles, (c) shows the rocks segmented using thresholding, (d) shows the volume extrapolated into 3D, (e) shows the aligned extrapolated volumes, (f) shows the intersection of the two aligned volumes.

ellipsoid with random axis length. The rough gravel shapes are created using the convex hull command in the MATLAB with random points. For the experiments, the corn stover bale sample shown in previous chapters is used. These rocks were added synthetically into the corn stover bale. Fifteen cases with randomly chosen locations and volumes are created for smooth pebbles and rough gravel. Table 6.1 and 6.2 shows the performance of the two-projection method with synthetic smooth pebble data and rough gravel data. The results show that the two-projection method could reconstruct and estimate the volume of the rocks with high precision. Similar to what was observed in chapter 5, the reconstructed volume with the two projection method is overestimated. The error observed here

is greater than what we observed in chapter 5 mainly because the sides of the rhombus are considered for a spherical phantom. In these experiments it is not the case, so we observe a larger error. In table 6.1 we see that for 30 and 15 degree separation we see an underestimate this is mainly because the some of the rocks volume has been cut-off during the reconstruction process.

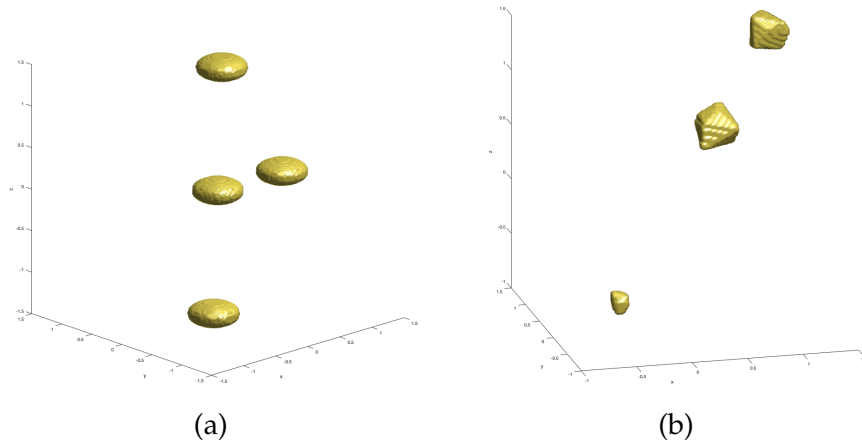


Figure 6.3: (a) Smooth pebble rock sample and (b) Rough gravel rock sample

Table 6.1: Quantitative analysis with synthetic smooth pebble data

Angle Separation	Volume Accuracy (%)	Average Position Deviation (")
135	108.90	0.018
90	103.20	0.017
75	107.80	0.017
60	107.35	0.017
45	108.90	0.018
30	98.90	0.018
15	97.35	0.017

After evaluating the two-projection method performance with synthetic rock data, a real rock contaminated mini-round bale was constructed. In this experiment, we took a few rock samples from a garden and added them to a mini corn stover bale. Figure 6.4 shows the 3D volume representation of the corn stover

Table 6.2: Quantitative analysis with synthetic rough gravel data

Angle Separation	Volume Accuracy (%)	Average Position Deviation (")
135	104.30	0.018
90	105.80	0.017
75	110.90	0.017
60	110.35	0.018
45	104.90	0.018
30	110.25	0.018
15	112.15	0.018

with the rocks represented with red color. Table 6.3 shows the performance of the two-projection method with the real dataset. The results show that with the two-projection method, we were able to reconstruct and estimate the volume of rocks and other metal contaminants with high precision. Similarly, the metal contaminants if present in the bale would have high bulk density, which results in high attenuation, so the work shown in this section can be expanded to detection of metal contaminants as well. The metal contaminants found in the bales are mainly from broken farm equipment such as bale spears and hitch parts.

Table 6.3: Quantitative analysis with a real rock sample

Angle Separation	Volume Accuracy (%)	Average Position Deviation (")
135	105.30	0.018
90	101.60	0.017
75	106.21	0.017
60	106.42	0.017
45	105.30	0.018
30	104.23	0.018
15	98.90	0.018

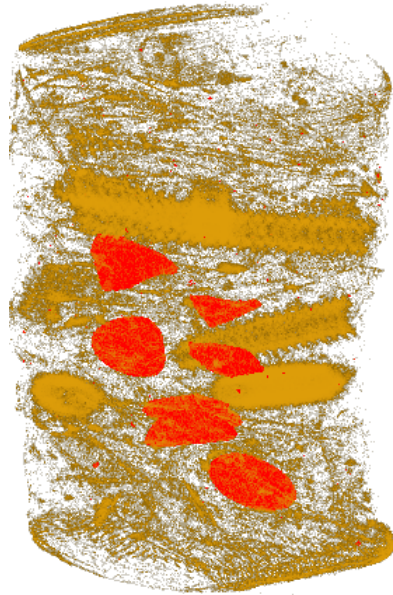


Figure 6.4: A 3D corn stover bale volume with rocks represented with a color red.

6.2 Detection of Soil Clumps in a Corn Stover Bale

After extracting the rocks and metal contaminants present in the bale, the next higher density materials are soil clumps. Soil clumps present in a corn stover bale have a bulk density of 1.23 g/cm^3 which is still greater than biomass (0.15 g/cm^3). In the acquired X-ray projections, after segmenting the rocks and metal contaminants, a thresholding technique is applied again to segment the soil clumps from the corn stover biomass. After the segmentation is done, the next step is to apply the two-projection method discussed in section 5.2.

To test the performance of the two-projection method for soil clump detection, a soil contaminated corn stover bale was prepared and X-ray projections were acquired. Figure 6.5 shows the 3D representation of the soil contaminated corn

stover bale. Since the soil clumps are very close to each other, several regions were combined and shown as one single region. So the total fraction of the estimated volume is estimated by using the number of on voxels information present the bale that represent the soil clumps with the the total number of on voxels, it is estimated that the soil clumps cover approximately 0.32% of the total volume. Table 6.4 shows the estimated volume fraction at each degree separation.

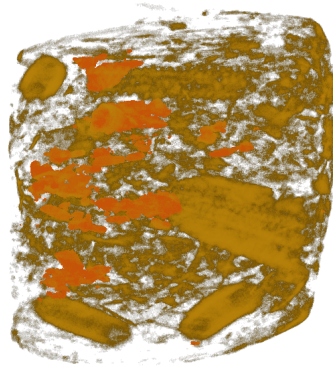


Figure 6.5: A 3D corn stover bale volume with soil clumps represented with orange color.

Table 6.4: Quantitative analysis with clumped soil sample covering 0.32% of the total volume

Angle Separation	Estimated Volume Fraction
135	0.43%
90	0.40%
75	0.43%
60	0.45%
45	0.43%
30	0.41%
15	0.31%

6.3 Detection of various Corn Stover Fractions

After the extraction of rocks and soil clumps, the bale composition is left with the corn stover fractions like cobs, stalks, leaves, and husks. Like rocks and soil clumps, corn stover fractions can also be classified into three groups based on the intensity profiles. The first group is mainly comprised of corn cobs and stalk nodes, making it a two-class classification problem. The second group comprises upper stalks and lower stalks. The latter is primarily occupied with what looks like isolated particles, but they are mainly leaves and husks. Since husks and leaves are very thin, in the pre-processed reconstructed data, they mostly look like dust (small components) in the reconstructed volume.

In this work, the statistical reconstruction method, MLEM, is applied to reconstruct the 3D volume from X-ray projections, as the two-projection method will not be able to provide high enough quality. As shown in section 5.1.2 among the iterative reconstruction methods, the MLEM algorithm provided better performance in terms of reconstruction quality and computational time. The MLEM is a statistical reconstruction algorithm which has future capability to incorporate the prior knowledge information to further increase the performance and application. Figure 6.6 shows the 3D volume reconstructed with the MLEM algorithm run with 3 and 5 projections at 5, 10, 30, and 100 iterations. After observing the reconstructed slices, we observed that using 5 projections with 10 iterations provides adequate quality to be able to perform classification. Once that is done, we can apply the techniques proposed in chapter 4 to locate and segment the corn cobs. A simple connected components approach could also be applied to extract the information

about the different regions.

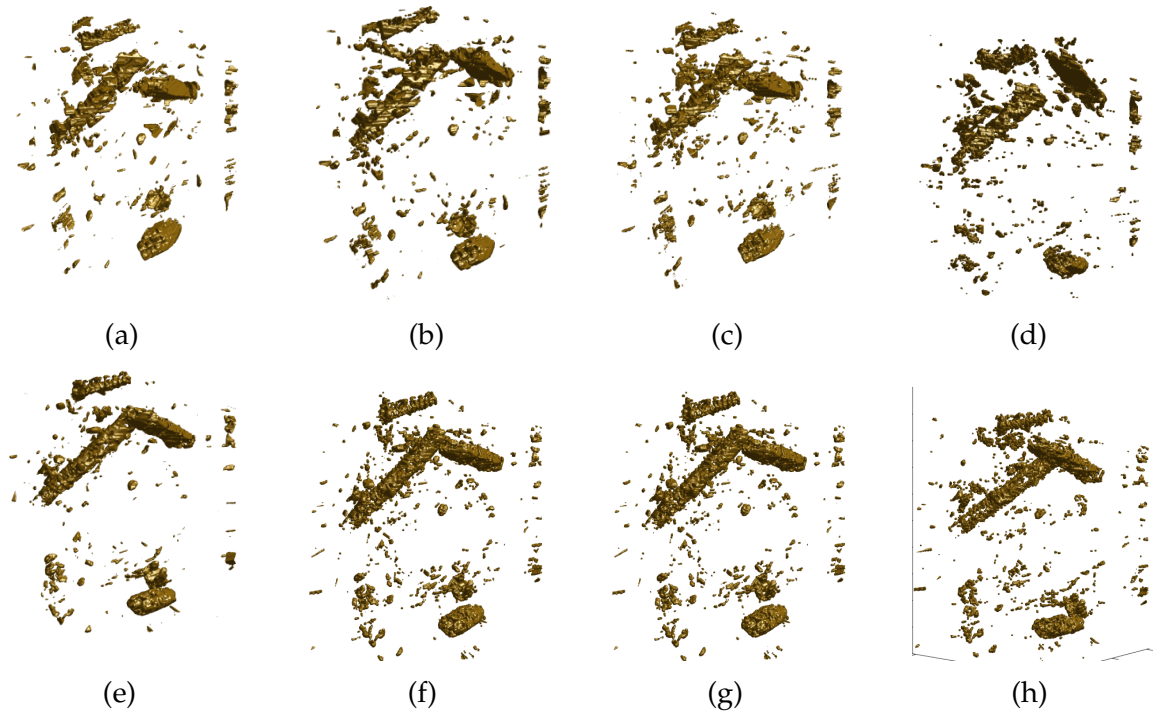


Figure 6.6: MLEM based reconstruction using 3 projections with (a) 5 iterations, (b) 10 iterations, (c) 30 iterations, and (d) 100 iterations, and reconstruction using 5 projections with (e) 5 iterations, (f) 10 iterations, (g) 30 iterations, and (h) 100 iterations.

After the corn cob and stalk node extraction, we are left with upper stalks and lower stalks. Since stalks are closely packed, the segmentation between them in the sparse view framework will become more complex. Which is not solved by the work of this dissertation. Figures 6.7 and 6.8 show the next two intensity profiles in the projections after corn cob and stalk node volume extraction. Figure 6.9 presents the different segmented regions of corn fractions in the bale.



Figure 6.7: A 3D volume of upper and lower stalks after corn cob and stalk node extraction.

6.4 Discussion

This chapter presented several strategies to extract and calculate the volume of various corn stover content like rocks, soil clumps, cobs and stalk nodes using limited X-ray projections. In this work, five X-ray projections evenly distributed are used to reconstruct the 3D volume from the projections. The results show that strategies devised in this chapter provide information about the corn stover contents with high precision.

However, there are limitations with this work, for example added moisture can increase the bulk density of the corn stover materials. Increase in bulk density will increase photon absorption which leads to more attenuation. Since the entire process depends on intensity profiles, that could lead to some error. In the future, the algorithm needs to be adapted to consider the moisture change. Similarly,

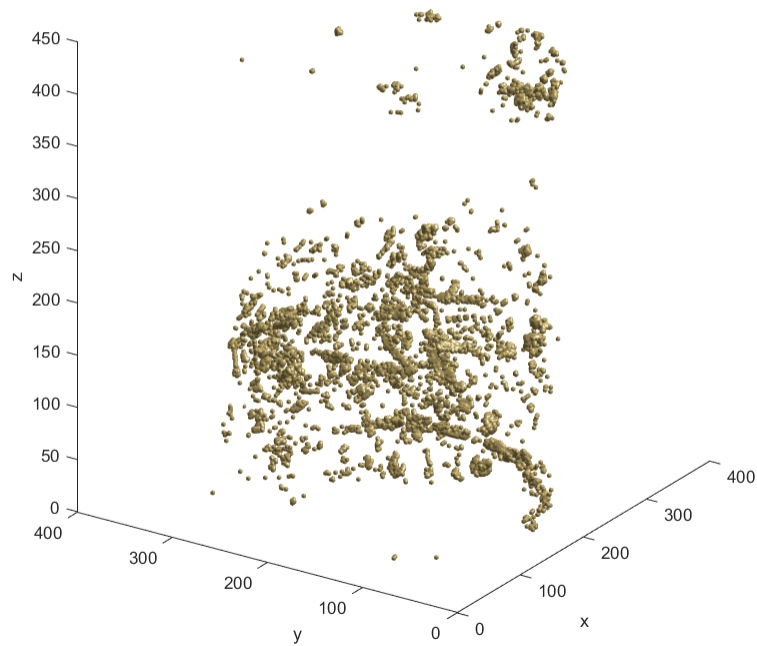


Figure 6.8: A 3D volume of leaves and husks appear as isolated voxels.

the current approach is not capable of classifying between upper stalks and lower stalks. However, using the yield monitor and knowledge about the content of cobs could provide some information. For instance when there is more cob content, the stalks will be mainly upper stalks because of how the bales are packed. In the future we need to consider this as well. Similarly, cob kernels are shown as high density materials.

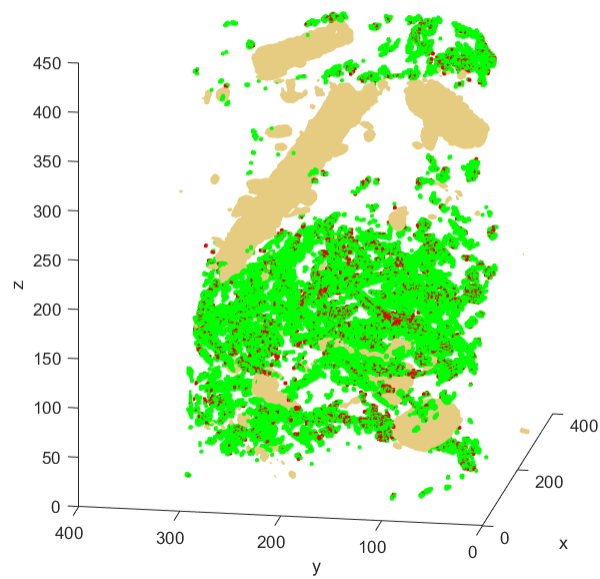


Figure 6.9: A 3D volume representation of a corn stover bale with brown color representing cobs and stalk nodes, green color for upper stalks and lower stalks, and red color represents the leaves and husks.

CHAPTER 7

ASSESSING THE FRAMEWORK FOR X-RAY TOMOGRAPHY AT A COMMERCIAL SCALE BIOREFINERY

In the previous three chapters, we presented several tissue characterization methods for studying the quality of corn stover bales. Chapter 4 provided a detailed description of 3D segmentation algorithms that utilize image analysis techniques like thresholding, and 3D skeletonization to segment and estimate the volume of different content present in a corn stover bale. Additionally, chapter 5 provided a detailed description of the sparse view reconstruction problem and the performance of several image reconstruction methods with few X-ray projections. The results in chapter 6 show that X-ray tomography with 3D image analysis in a sparse view framework can provide the necessary information about the contents of the corn stover bale with high precision.

All the experiments in the previous chapters used a mini-round bale with a diameter of 5" and a height of 6". However, at a commercial biorefinery, we will need to work with bales of dimensions 3' x 4' x 8'. To evaluate the performance of using X-ray tomographic techniques at the biorefinery, it is essential to identify and study the behavior of X-ray photon absorption parameters, such as the linear attenuation coefficient (μ), and bulk density (ρ). Similarly, it is also essential to

identify and study the parameters that change the elemental composition of the bale, which play a significant role in the X-ray photon transmission and interaction through the bale.

The linear attenuation coefficient, μ , is an important parameter that characterizes how easily an X-ray beam can penetrate a layer of the material. The μ depends on the chemical composition of the material and the incident photon energy. The overall X-ray attenuation through the material is also proportional to the bulk density (ρ) as described by Beer-Lambert's law. This chapter looks more specifically at the change in energy absorption parameters with moisture content (MC) and soil content (SC). These two factors change the overall chemical composition and the bulk density, affecting the X-ray photon attenuation through the bale.

This chapter starts by reviewing the behavior of parameters, μ and ρ , with a change in MC and SC of the bale. Next, the feedstock supply chain at the biorefinery is examined. Then we identify the locations within the feedstock supply chain where X-ray tomography can be integrated and define the achievable goals. In the end, we will examine the behavior of X-ray transmissivity through the corn stover bale with a change in moisture and soil content at the defined energy range. In this study, we consider three MC values of 15%, 25%, and 35%, and four SC values of 5%, 10%, 15%, and 20%. These specific conditions help to study the behavior of the linear attenuation coefficient and X-ray transmissivity for realistic conditions of the bale.

7.1 Beer-Lambert's Law and X-ray Photon Absorption Parameter Estimation

A brief introduction to the Beer-Lambert law and the procedure to calculate the photon absorption parameters, like linear attenuation coefficient, and bulk density are described in this section.

7.1.1 Beer-Lambert's Law

When a X-ray beam passes through a material of thickness t , the photons are transmitted according to Beer-Lambert's law [61]. This process is expressed as

$$I = I_0 * e^{-(\mu t)}, \quad (7.1)$$

where I_0 is the X-ray intensity at the X-ray source, I represents the observed intensity at the detector after attenuation when passed through the material with thickness t and linear attenuation coefficient μ (cm^{-1}). The linear attenuation coefficient cannot be computed directly, so the linear attenuation coefficient is described as

$$\mu = (\mu/\rho) \rho, \quad (7.2)$$

where μ/ρ (cm^2/g) represents the mass attenuation coefficient and ρ represents the bulk density. With this and defining x to represent the mass thickness as the mass per unit volume, $x = \rho * t$. With this, equation 7.1 can be rewritten as

$$I = I_0 * e^{-(\mu/\rho)x}. \quad (7.3)$$

A derivation of equation 7.1 is found in section 2.2, which provides a comprehensive background on X-ray tomography. Discussion in this chapter uses monoenergetic photons passing through a single path, however most of the mathematics in this chapter can be easily applied to other geometries like Cone Beam CT, Helical CT, and Dual Energy CT. The underlying conclusions will remain the same.

In X-ray tomography, the fractional transmitted intensity I/I_0 is used as a measure of how many rays pass through the object [42]. In this chapter, the fractional transmitted intensity value is used to evaluate the performance of the X-ray tomography with variations in moisture and soil content. The transmitted intensity calculated from equation 7.3 is,

$$I/I_0 = e^{-(\mu/\rho)x}. \quad (7.4)$$

Here I , I_0 , and x are measured values. The parameter ρ depends on the baler's operational settings and the material composition, and μ depends on the material composition and the incident energy I_0 . Since ρ and μ are dependent on the material composition, it is essential to study the factors like MC and SC which influence these parameters.

7.1.2 Bulk Density

Bulk density, also called packing density, is defined as mass per unit volume. To estimate the bulk density of a corn stover bale, we refer to the work published

by Glassner et al. [62]. In [62], Glassner et al. stated that the John Deere balers aim to acquire 550 kg (1,200 lbs) of dry weight for big 4' x 4' x 8' square bales. The authors estimate that the bales have a bulk density of 9.375 lbs/cc.ft (0.15 g/cm³). In this work, 0.15 g/cm³ is used as a reference to represent dry matter bulk density of corn stover bale that is free from moisture and soil contamination.

Since moisture or soil contamination affect the bulk density of the bale, it is essential to know how the moisture content and soil content affect the bulk density of the bale. The term "soil content" used in the chapter usually refers to the weight fraction of soil present in a bale. For example, 10% soil content means 10% of the dry matter weight is from the mass of the soil. However, the moisture content in a bale is expressed in two forms, wet basis, and dry basis [63]. Wet basis moisture content (designated M_w) refers to the percentage equivalent of the ratio of the weight of water (W_w) to the total weight of the material (W_t) [63]. In contrast, the dry basis (designated M_d in this chapter) provides the percentage equivalent of the ratio of the weight of water (W_w) to the weight of the dry matter (W_d) [63]. The wet basis and dry basis moisture contents are

$$M_w = \left(\frac{W_w}{W_t} \right) * 100 = \left(\frac{W_w}{W_w + W_d} \right) * 100, \quad (7.5)$$

$$M_d = \left(\frac{W_w}{W_d} \right) * 100. \quad (7.6)$$

In this chapter, we will use the term "moisture content" to refer to the wet basis moisture content. To estimate the weight of the water in a bale, the wet basis moisture content needs to be converted to dry basis moisture content. It is calculated using:

$$M_d = \left(\frac{M_w}{100 - M_w} \right) * 100. \quad (7.7)$$

The individual weights of the water (W_{water}), soil (W_{soil}), and stover (W_{stover}) are calculated from the dry matter weight using,

$$W_{water} = M_d * W_d = M_d * \rho_d * Volume, \quad (7.8)$$

$$W_{soil} = SC * W_d = SC * \rho_d * Volume, \quad (7.9)$$

$$W_{stover} = \rho_d * Volume. \quad (7.10)$$

Once the individual weights of water, soil, and stover are calculated, the effective bulk density is calculated using

$$\rho_{eff} = \frac{W_{water} + W_{soil} + W_{stover}}{Volume_{bale}}. \quad (7.11)$$

7.1.3 Linear Attenuation

The linear attenuation coefficient, μ , depends on the composition of the material, which can be calculated from the mass attenuation coefficient value using equation 7.2. The total mass attenuation coefficient μ/ρ for materials composed of multiple elements is equivalent to a weighted sum of the $(\mu/\rho)_i$ values of each constituent element [64]:

$$\mu/\rho = \sum_i w_i (\mu/\rho)_i \quad (7.12)$$

where w_i is the fraction by weight of the i^{th} atomic constituent. In this work, two standard reference databases were used to calculate the mass attenuation coeffi-

cient values of the corn stover. Firstly, the Phyllis database [65] is used to determine mass fractions of each element present in the corn stover. Phyllis is a database containing information on the composition of biomass, macro-and micro-algae, feedstocks for biogas production, biochar, and torrefied biomass. Table 7.1 shows the elemental mass fraction information of the corn stover biomass.

Table 7.1: Elemental mass composition of corn stover

Elements	Mass %
Oxygen (O)	0.4231
Silicon (Si)	0.0131
Carbon (C)	0.4789
Calcium (Ca)	0.0032
Potassium (K)	0.0089
Sodium (Na)	0.0001
Magnesium (Mg)	0.0019
Sulfur (S)	0.0011
Phosphorus (P)	0.0010
Chlorine (Cl)	0.0027
Aluminium (Al)	0.0005
Hydrogen (H)	0.0587
Nitrogen (N)	0.0068

Elemental mass fractions of moisture and soil content are estimated by taking the chemical composition of each into account. For moisture, the chemical formula used is H_2O . Individual weight fractions are calculated by considering the atomic weight of the element with the number of atoms. Table 7.2 shows the elemental mass composition information used to represent moisture content.

Table 7.2: Elemental mass composition of moisture content

Elements	Mass %
Oxygen (O)	0.8881
Hydrogen (H)	0.1119

In [66], according to Krupenikov et al. the significant elements of soil are conventionally expressed as oxides; on this basis, 60–70% is silica (SiO_2) and 13–16% alumina (Al_2O_3). The paper also stated that there are substantial amounts of iron (5–6%) and silicate calcium (about 2%) [66]. Using the mixture rule, the elemental composition of the soil is calculated. Table 7.3 shows the elemental mass composition information used to represent soil content present in the bale.

Table 7.3: Elemental mass composition of soil content

Elements	Mass %
Oxygen (O)	0.4722
Silicon (Si)	0.3269
Iron (Fe)	0.0419
Calcium (Ca)	0.0143
Aluminium (Al)	0.0846

Next, the X-Ray Attenuation and Absorption for Materials of Dosimetric Interest (XAAMDI) database [64] from the National Institute of Standards and Technology (NIST) is used to obtain the mass attenuation coefficient value of each atomic element at a given energy. To account for the characteristics peak, for any given peak voltage, the mass attenuation coefficient value is calculated at two-thirds of the peak voltage. Once the total mass attenuation coefficient is calculated using equation 7.12, the linear attenuation coefficient is estimated by taking the product of the mass attenuation coefficient and the bulk density (equation 7.2).

7.2 Bulk Density Behavior with Moisture and Soil Content

Section 7.1.2 explained the procedure to calculate the bulk density of a corn stover bale. In this section, we try to understand how the moisture and soil content

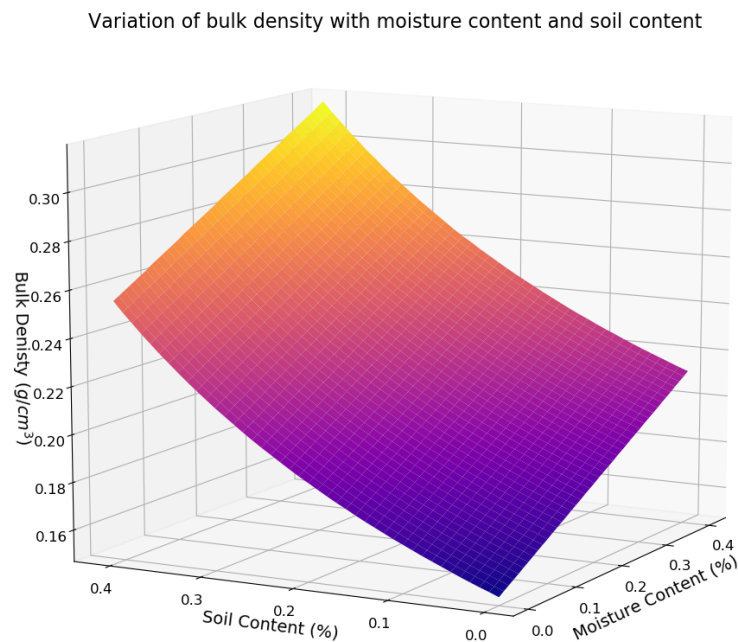


Figure 7.1: A 2D surface plot showing the change in bulk density of a bale with respect to change in moisture content and soil content. Higher quantities of soil & moisture increases the bulk density.

change the bulk density of the bale. Figure 7.1 is a surface model that shows the variation in bulk density with an increase in soil and moisture content. The x-axis represents the soil content, the y-axis represents the moisture content, and the z-axis represents the bulk density of the bale in g/cm^3 .

Additionally, figures 7.2a and 7.2b show the average variation of bulk density with increase in moisture content and soil content respectively. Figure 7.2a shows that there is a linear relationship between soil content and bulk density. Every 10% increase in soil content increases the bulk density by a factor of 0.015. Similarly, Figure 7.2b shows that the moisture content shows an exponential relationship to

bulk density.

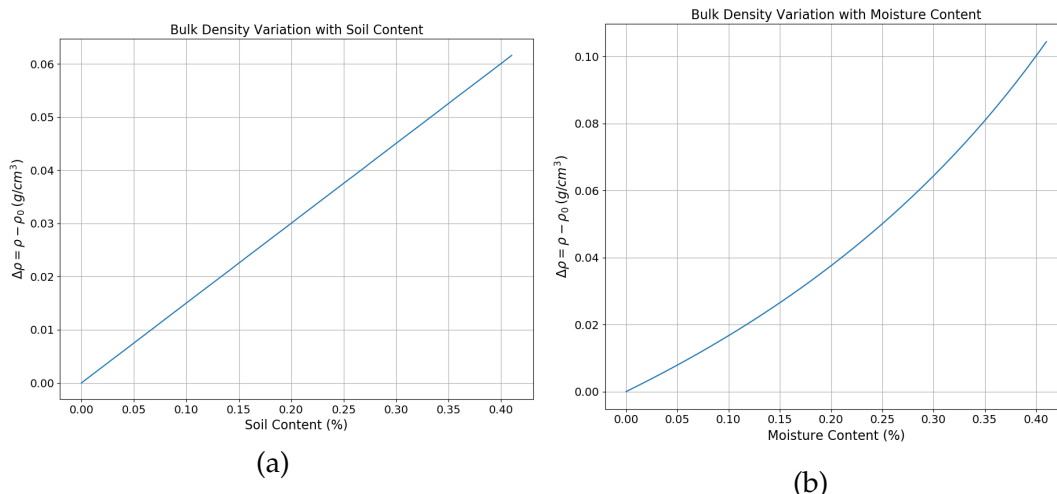


Figure 7.2: Variation of bulk density with (a) soil content, (b) moisture content.

7.3 Linear Attenuation Behavior with Moisture and Soil Content

Section 7.1.3 showed the procedure to calculate the linear attenuation coefficient of a corn stover bale by considering the elemental composition of the corn stover, soil, and moisture accordingly. This section demonstrates how the moisture and soil content changes the linear attenuation coefficient. Figures 7.3, 7.4 and 7.5 show the linear attenuation coefficient values of corn stover samples with moisture contents 15%, 25% and 35%. Each figure shows the linear attenuation coefficient values at various soil content ranging from 5%, 10%, 15% and 20%. The moisture levels are taken from the work published by Smith et al. in [67], which stated that the moisture observed in the bales is as low as 15% and as high as 35%. The 25% moisture content is used to represent a moderately moist sample. Similarly, Bonner et al. in [24] stated that the mean ash content ranges from 11.5%

to 28.2%, depending on operational choice. However, the ash content estimated in the work [24] includes both soil derived ash content and ash content because of the inherent inorganics. To account only for the soil derived ash content, soil content is set at 5%, 10%, 15% and 20% to represent low, moderate to high soil contamination. Limiting the study to these specific conditions helps to observe the linear attenuation coefficient values for realistic conditions of the bale. From figures 7.3, 7.4, and 7.5 it can be observed that both an increase in soil or moisture content increases the linear attenuation coefficient. However, the change or shift is not drastic, and the linear attenuation coefficient increases by 0.001 for every 5% increase in soil content. A similar trend is observed with moisture content, where a drop of 0.003 is observed from low to moderate moisture and a drop of 0.004 is observed is from moderate to high moisture levels. The attenuation resembles bulk density behavior where after moderate moisture levels the bulk density showed an exponential increase. The results only conclude that with an increase in moisture or soil content, the amount of attenuation observed will increase.

7.4 Integration of X-ray Tomography into the Feedstock Supply Chain of the Biorefinery

In section 7.2 and 7.3, it is shown that an increase in moisture or soil content increase the bulk density and linear attenuation coefficient of the bale. To determine whether X-ray tomographic techniques developed in this dissertation can be applied at the biorefinery, we need to identify another vital photon absorption parameter, the thickness of the material. Typically, the baler packs the corn stover

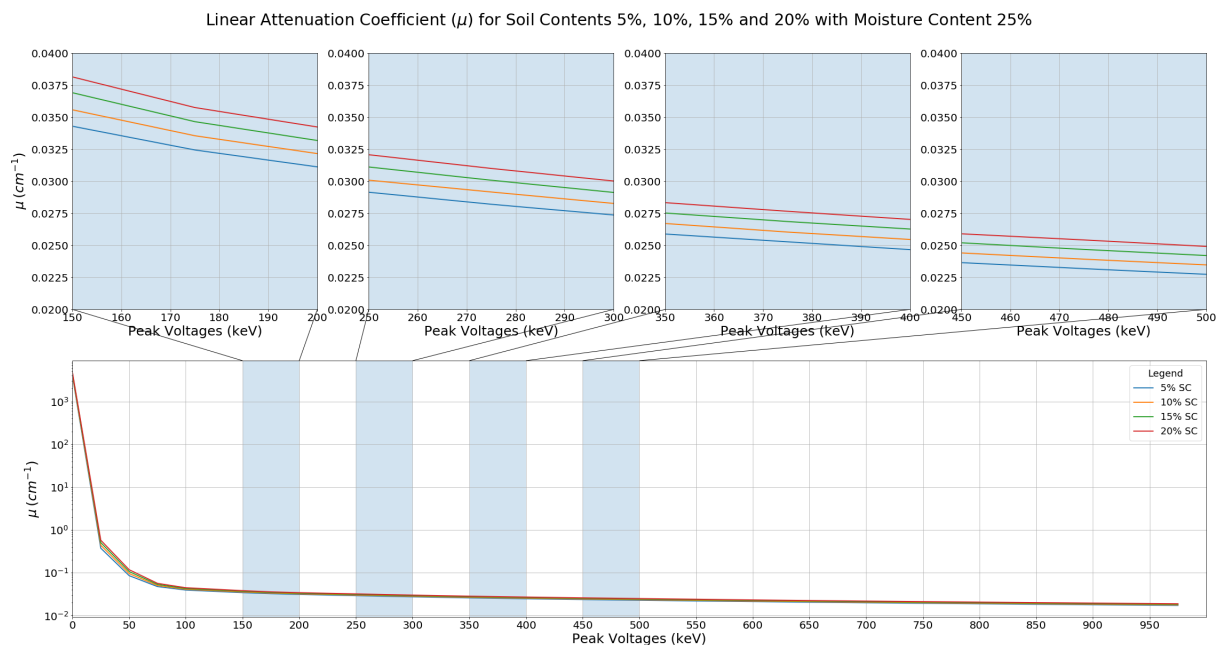


Figure 7.4: Linear attenuation coefficient with 25% moisture content and soil contents 5%, 10%, 15% and 20% versus peak voltage.

the bale. The rest of this section focuses on defining the achievable goals, detector resolution and defining the ideal energy ranges that would need to be used at the biorefinery if these techniques were to be used.

Similar to the linear attenuation coefficient discussion, in this section, we will limit the study to moisture contents of 15%, 25%, and 35% and soil contents of 5%, 10%, 15% and 20%. The moisture contents used in the study represent a dry to high moisture sample, and similarly soil content represents a low to high soil contaminated samples. Bales with moisture contents greater than 35% and soil contamination greater than 20% are not preferred at the biorefinery, so it is not necessary to study effects at higher levels.

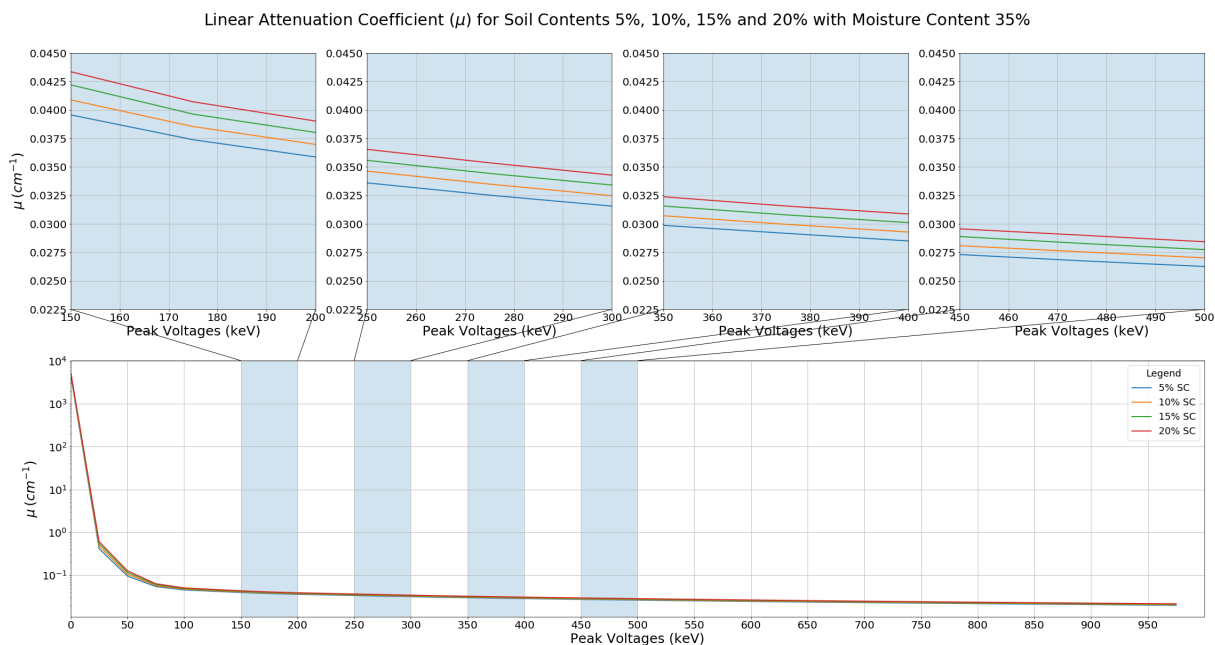


Figure 7.5: Linear attenuation coefficient with 35% moisture content and soil contents 5%, 10%, 15% and 20% versus peak voltage.

7.4.1 Scanning the Truck Load

The first possible place where a CT scanner could be used would be to scan the input feedstock directly on the truck as the transport arrives at the biorefinery. Generally, the trailers carrying corn stover bales have two stacks of bales arranged in a given row. Each bale has a dimension equivalent to 3' x 4' x 8', so the X-ray beam should transmit through a 6' bale thickness to reach the detector. Figures 7.7, 7.8 and 7.9 show the fractional transmitted intensity (I/I_0) with moisture contents at 15%, 25%, and 35% respectively. Each figure shows I/I_0 at different soil contents varying from 5%, 10%, 15%, and 20%.

The I/I_0 plots show that the detector receives less than 3% of the incident energy at peak voltage less than 500kV. However, at higher peak voltages in terms

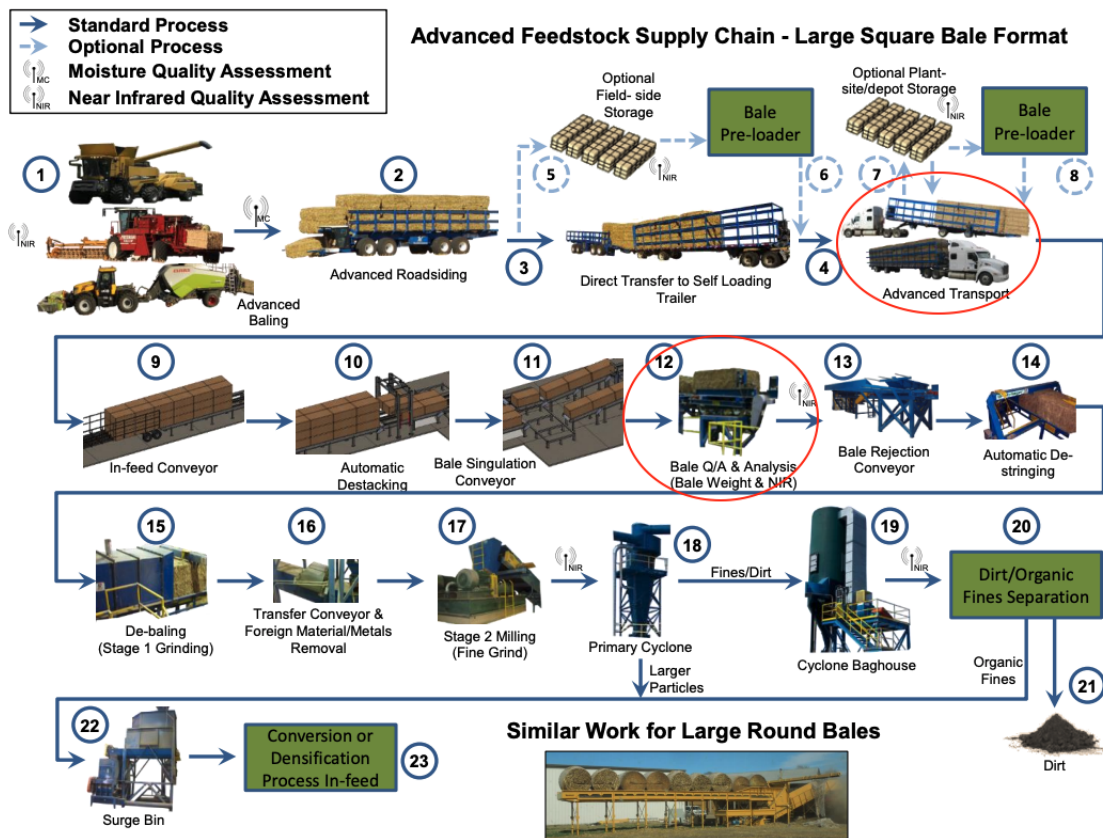


Figure 7.6: Advanced feedstock supply chain at a biorefinery [68]. At stages 4 and 12 (circled) techniques developed in this work can be applied.

of 1 MV, it received a maximum of 5%. For example, for a bale with 15% MC and 5% SC with incident peak voltage between 350-400 kV the detector receives a maximum of 2% of the initial peak voltage. The plots show that the I/I_0 drops by 0.2% for every 5% increase between low to moderate soil contents (5% to 15%). Moreover, from moderate to high soil contents (15% to 20%), a drop of 0.1% is observed. A similar trend is observed with moisture contents, where the I/I_0 value drops by a factor of 0.8% between low to moderate moist samples and a factor of 0.5% between moderate to high moist samples. With a 16-bit detector knowing a 0.2% change between levels will require $2^{16} * 0.0002 = 13$ bits. These 13 bits should

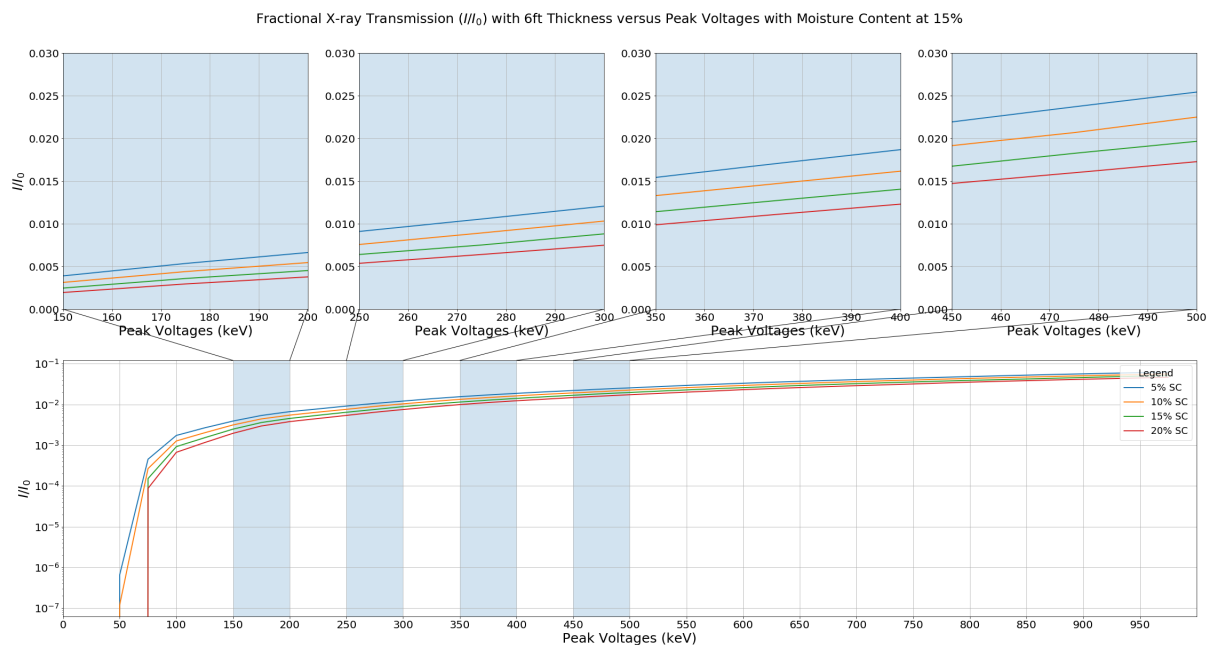


Figure 7.7: Fractional X-ray transmission (I/I_0) with 15% moisture content and soil contents 5%, 10%, 15% and 20% with 6ft thickness of the material versus peak voltage.

represent the full voltage received at the detector. It will not provide sufficient contrast between most organic contents of the bale. Therefore, the application of X-ray tomography to scan a truckload has limited applications.

When scanning a truck load, imaging techniques with CT can be used to detect high attenuation regions, such as big rocks and high moisture regions. Rocks or clumped soil [24] have bulk densities 2.67 and 1.66, respectively. In the presence of these high density materials significantly fewer photons will reach the detector, thus leaving a blind spot, or dark region in the reconstructed image denoting the presence of these object. Using the two-projection reconstruction method described in section 5.2, we can take two projections, threshold the images to isolate the rocks and high moisture areas, and produce a 3D image that includes blobs

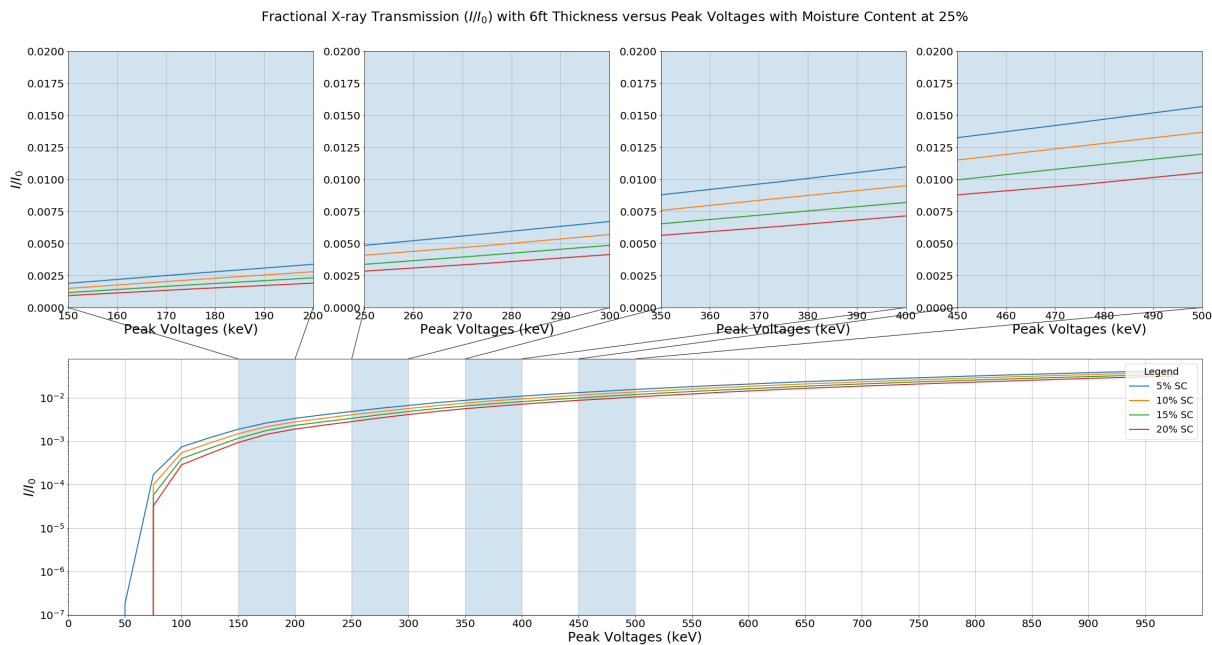


Figure 7.8: Fractional X-ray transmission (I/I_0) with 25% moisture content and soil contents 5%, 10%, 15% and 20% with 6ft thickness of the material versus peak voltage.

representing these objects. From this 3D volume we can then estimate the volume information and location of the rocks and high moisture regions. 3D shape analysis can be used to distinguish rocks and soil clumps from high moisture regions. High moisture regions will look more distributed, whereas rocks and soil have a specific convex structure. To account for rocks and soil clumps [24] a linear array detector with a pixel pitch of a quarter to half an inch can be used. The term pixel pitch refers to the dimensions of each pixel in the detector.

7.4.2 Scanning a Single Bale

For Q/A analysis of the feedstock, the CT scanner will need to scan a single bale. Here the X-ray beam should transmit through 3' bale thickness and reach the

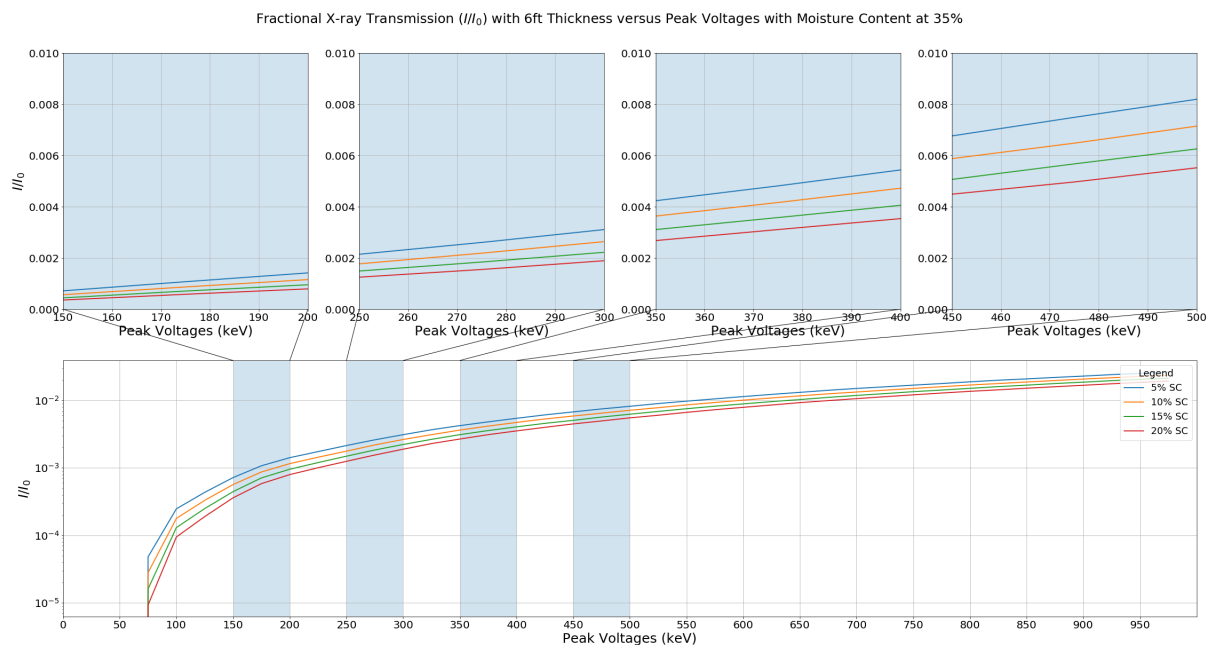


Figure 7.9: Fractional X-ray transmission (I/I_0) with 35% moisture content and soil contents 5%, 10%, 15% and 20% with 6ft thickness of the material versus peak voltage.

detector. Figures 7.10, 7.11 and 7.12 show the fractional transmitted intensity (I/I_0) with moisture contents at 15%, 25%, and 35%, respectively. Each figure shows I/I_0 at different soil contents varying from 5%, 10%, 15%, and 20%.

In the plots between 350-400 kV, the I/I_0 value ranges from 14% to 4% with the change in moisture and soil content change. At peak voltages greater than 300keV, the plots show that for dry to moderate samples, I/I_0 drops by 1% for every 5% increase in soil content. A similar trend is observed with the high moisture sample, but the drop observed is only 0.4%. Analysis of moisture content shows that low (15%) to moderate (25%) moisture samples show a drop of 3%, and moderate (25%) to very moist samples (35%) show a drop 2%. At the biorefinery, high moisture samples will be rejected, so we can neglect the soil content change in that situation.

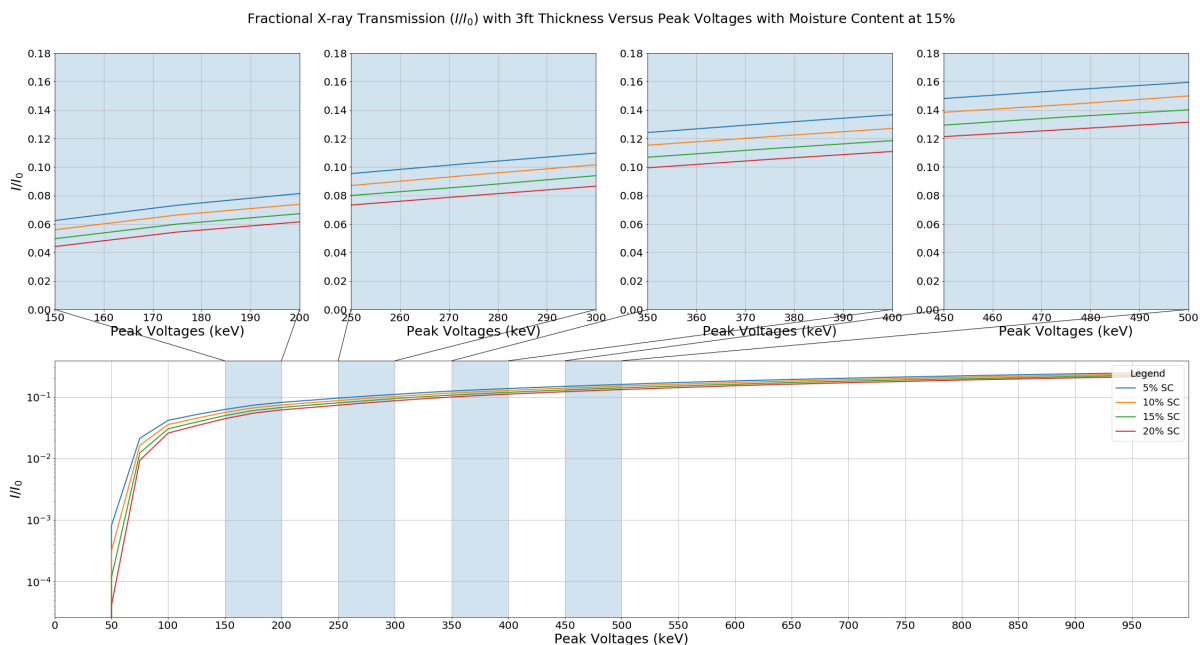


Figure 7.10: Fractional X-ray transmission (I/I_0) with 15% moisture content and soil contents 5%, 10%, 15% and 20% with 3ft thickness of the material versus peak voltage.

In the dry to moderate samples, the minimum drop observed between soil contents is 1%. With a 16-bit detector accounting for the 1% change, we will have $2^{16} * 0.01 \approx 655$ levels and assuming only 60% of the bits are available will return $655 * 0.6 \approx 400$. Thus the complete voltage range at the detector can be represented with 400 grayscale values. With 400 grayscale values we should have enough contrast to classify the different content of the bale. We therefore conclude that it is possible to scan a single bale at the biorefinery and produce a 3D volume representation of the bale with enough details to analyze using techniques in chapters 4 and 6 to segment and estimate the volume of different contents of the corn stover bale – rocks, soil clumps, and cobs – with peak voltage between 350-400 keV. To account for the dimensions of each corn stover component [69], a

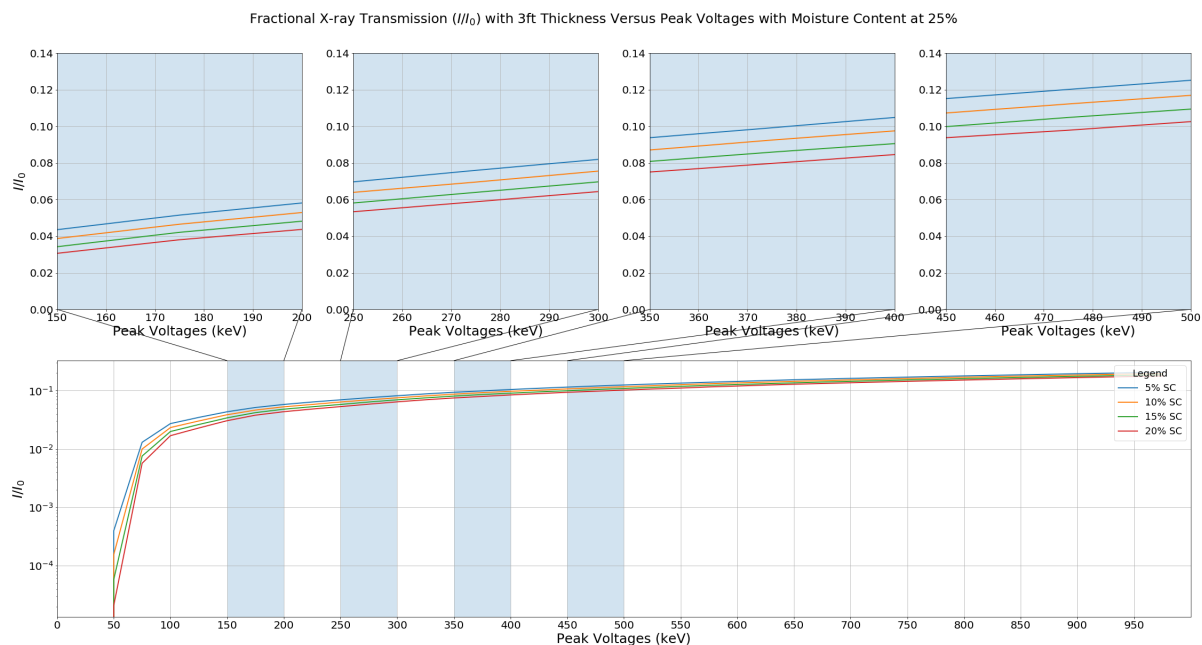


Figure 7.11: Fractional X-ray transmission (I/I_0) with 25% moisture content and soil contents 5%, 10%, 15% and 20% with 3ft thickness of the material versus peak voltage.

flat panel detector with a pixel pitch of 1 cm can be used for the application. The term pixel pitch refers to the dimensions of each pixel in the detector.

7.5 Discussion

In the previous chapters many techniques were provided to locate and estimate the volume of rocks, soil clumps and cobs present in a minibale. In this chapter, we have considered the challenges and theoretical performance of using X-ray tomography at a commercial-scale biorefinery. Based on the linear attenuation coefficient and bulk density behavior with moisture content and soil content, the expected image details can be determined. The chapter emphasizes the two locations

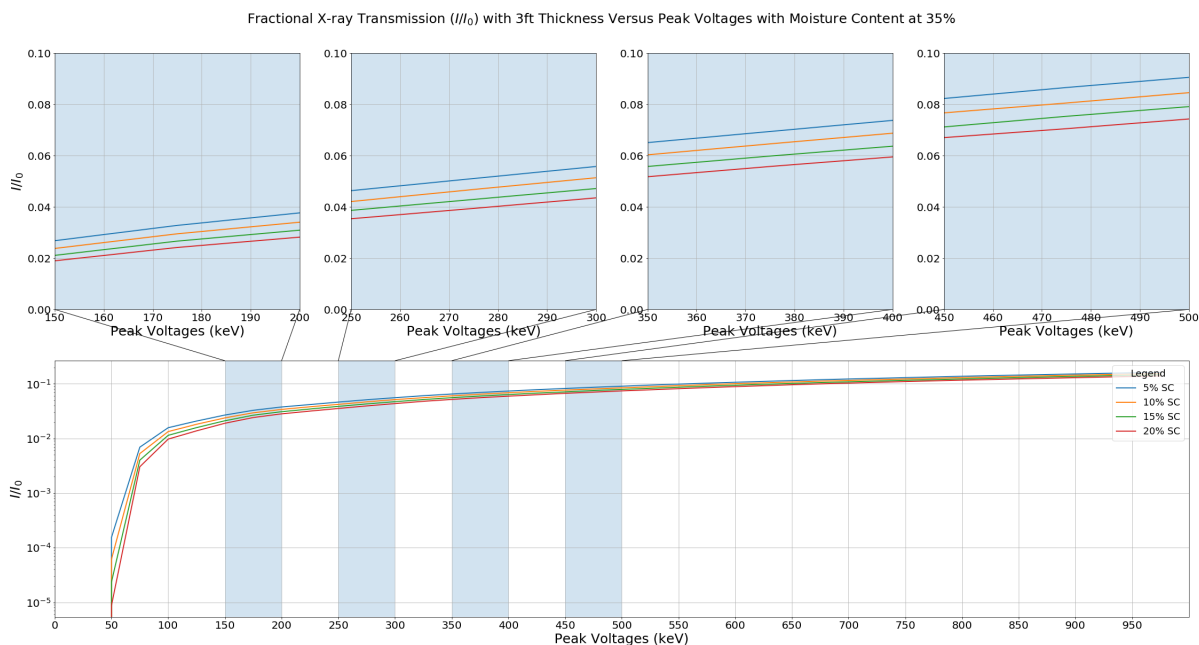


Figure 7.12: Fractional X-ray transmission (I/I_0) with 35% moisture content and soil contents 5%, 10%, 15% and 20% with 3ft thickness of the material versus peak voltage.

within the feedstock supply where X-ray tomographic techniques presented in this dissertation can be applied. Furthermore, the chapter also provided a detailed description of strategies associated with classification, technical specifications associated with X-ray tomography integration into the feedstock supply chain of the biorefinery.

Since the work is based mainly on theoretical calculations, there are limitations. Several issues need to be addressed before applying X-ray tomography to a commercial-scale biorefinery. In this work, the bulk density showed an exponential relationship with moisture content. The absorption rate and characteristics of corn stover materials at several moisture concentrations need to be accounted for to get practical bulk density information. Likewise, electrical noise, quantization

errors, and other sources of image artifacts in the reconstructed image need to be studied. Similarly, the importance of motion compensation while scanning the bale may need to be considered if the stover is to be scanned without temporarily halting the process.

CHAPTER 8

CONCLUSION AND FUTURE DIRECTIONS

Biofuels present a promising and sustainable pathway to reduce the fossil-based fuel demand. The sustainability of the biofuels depends on the biorefineries ability to examine the incoming biomass feedstock in a fast and non-destructive fashion and provide a quality assessment. Thus, prior knowledge about the volumetric content of different anatomical fractions in the corn stover bale during the pre-processing or screening stage can help optimize the conversion process and achieve a high yield. The current capabilities are very time-consuming and labor-intensive. In this dissertation, we attempt to develop a sensing framework using X-ray tomography to study the quality of the biomass feedstock at a commercial-scale biorefinery. This dissertation presents the reconstruction algorithms and 3D image analysis strategies we developed and implemented to provide a volumetric estimate of the contents of a corn stover bale. This chapter presents a generalized discussion of the research problems solved in the dissertation, followed by a discussion of the future directions with the tissue characterization with X-ray tomography. Here is the summary of research problems solved and our contributions through this dissertation:

1. **The quantitative comparison of 3D skeletonization algorithms using sur-**

face degradation models. The implementations of 3D skeletonization algorithms presented in the dissertation are easy to use. These tools provide access to skeletonization algorithms for researchers to use and adapt for their application easily. Having the implementations in MATLAB and Python helps reach a broad group of researchers in different programming environments. 3D skeletons are widely used in many applications. However, the underlying concepts vary with the algorithms making it hard for the researchers to decide which algorithm to use. The evaluation metrics and the surface degradation models presented with the skeletonization algorithms help to study the topology and efficiency of the skeleton to represent a 3D object. The skeletonization algorithms presented in the dissertation represent only a subset of commonly known techniques, from morphological thinning to Euclidean distance field-based skeletons commonly seen in the literature. In the future, we will extend the quantitative comparison to other known skeletonization algorithms.

- 2. The 3D image analysis strategies to segment and estimate the volumetric content of different tissue fractions in a corn stover bale in a conventional CT framework.** The strategies implemented and the algorithms developed to characterize the various contents of the bale in the conventional CT framework provide very high accuracy. The histogram-directed thresholding strategy presented in chapter 4 segments the rocks and soil clumps very effectively. The algorithm we developed to characterize the corn cobs with the help of 3D skeletons makes them robust to changes, like an increase in density with increased moisture content or ash content, causing a difference

in the intensity value observed in the reconstruction. In most situations, the corn cobs retain their shape and texture, making the developed algorithm very effective. Currently, the segmentation using skeletonization requires a significant computation power which needs to be addressed in the future.

3. **The 3D image analysis strategies to segment and estimate the different tissue fractions of the corn stover bale in a sparse view framework.** Acquisition time is directly correlated with the number of projections acquired for a given bale. Many projections are required to reconstruct the 3D volume in a conventional framework, which drastically increases the acquisition time. For a real-time quality analysis, the acquisition time should be minimal. Where the overall idea is to complete the acquisition and analysis under 2 minutes to be precise 90 seconds. We experimented by reducing the number of projections to understand how different reconstruction algorithms behave in a sparse view framework. Our work concluded that the statistical reconstruction method, MLEM is more suitable for applications where complex information needs to be extracted. We also developed a simple and less computationally intensive two projection method that provided high precision volumetric and position estimates. Using these reconstruction algorithms, we detected the rocks, soil clumps, and corn cobs using very few X-ray projections with high accuracy. This knowledge during pre-processing provides a significant load of information and fills a big technological gap with the quality assessment work at a biorefinery.
4. **The demonstration of the applicability of using X-ray tomography at a commercial-scale biorefinery.** We showed that we could extract the volu-

metric content information of the corn stover bale with decent accuracy using few X-ray projections. All the experiments we conducted were on a mini round cylindrical bale with a diameter of 12.70 and a height of 15.24 cm. At a commercial-scale biorefinery the bales are in the form of rectangular bales with dimensions $4' \times 4' \times 8'$ or $3' \times 4' \times 8'$. To understand the applicability of X-ray tomography at the commercial-scale biorefinery. We tried to evaluate how the X-ray energy conditions change when the bale dimensions are increased. Several experiments were conducted. The conclusion from that analysis is that X-ray tomography can be applied at two places at the biorefinery. One is scanning the truckload, and the other is scanning the single bale. When scanning the single bale, if an X-ray source with average photon energy between 350-400 *keV* is used, the reconstructed 3D volume of the bale will have enough contrast, and we can extend the techniques developed in this dissertation to work with single bale. However with the truckload scenario, we saw that X-ray tomography has limited applications. The energy reaching the detector after passing through the bale is very small. It doesn't provide enough contrast to be able to segment different tissue fractions. We concluded that the applications of X-ray tomography could be limited to the important needs of detecting big rocks and moisture content estimation by incorporating 3D shape analysis.

Future Directions

As is common with any research, the future work possibilities span a broader, more extended research focus than the work itself. Next I present areas for future

work.

Currently, the skeletonization algorithms run on CPUs. Implementing 3D skeletonization algorithms on GPUs can significantly improve the computational times. Having a computationally faster algorithm will further benefit a wider audience working with large datasets.

We need to evaluate the performance of the implemented skeletonization methods with more complex shapes like a toroid. Other metrics need to be defined which can tell information about how much of the original volume can be recovered from the skeleton, how much shape corners are preserved, how thick the skeleton is, and whether the skeleton extracted is really along the center. Also, geometric entropy information needs to be estimated to correlate the original and a noisy skeleton.

Currently, there are a few limitations with the corn cob detection algorithm presented in chapter 4. The algorithm doesn't provide accurate results when the shape of the corn cob is not intact. The algorithm should be modified to detect the broken corn cobs by incorporating corn cob texture information. Future research goals should include optimizing the model to differentiate between a loop formed with a corn cob and a fully intact corn stalk. In the future, capturing information using morphological processing with different structuring elements should be explored.

The tissue characterization methods, especially corn stover fractions in the sparse view framework, rely on segmenting the regions in the projections based on the intensity. An increase in the moisture or ash content can change the overall X-ray

photon attenuation, which in turn can change the intensity profile of the voxels. In future work we need to implement a moisture content detection method. Currently, the NIR can estimate the correct moisture content value, but it is sampling intensive. In chapter 7, we observed that an increase in moisture content increases the attenuation. We can define the regions of interest using the intensity profiles and then use the NIR to calculate the actual moisture content value. The MC information can be used as an offset factor for the given region of interest.

It would also be helpful to be able to distinguish between upper stalks and lower stalks. The reconstruction quality is not high enough to estimate or separate the upper stalks from lower stalks when using fewer projections. In the future, using the yield monitor information and the composition of corn cob knowledge, we could estimate the possible composition of the upper stalks from lower stalks.

While developing algorithms in the sparse view framework, the pixel pitch of the detector and the size of each voxel are made equal, i.e., 1 *mm*. Future studies should evaluate the performance when the pixel pitch of the detector and the size of each voxel are not equal. Similarly, we need to study how the criteria for the volume correction factor presented in chapter 5 change with the different X-ray geometry configurations. The X-ray geometry configuration used here has the entire bale in the X-ray source's Field of View (FOV) in all the experiments, because the dimensions of the detector are larger than the dimensions of the bale. Future study needs to focus on understanding what role the X-ray geometry configuration plays in the offset factor. Also, the two projection method needs to be optimized to reduce the time complexity when the input data size is large.

In chapter 7, the work presented is mainly based on theoretical calculations, so there are limitations. Several other issues need to be addressed before applying X-ray tomography to a commercial-scale biorefinery. In the future, the absorption rate and characteristics of corn stover materials at several moisture concentrations need to be studied to get more realistic bulk density information. Likewise, electrical noise, quantization errors, and other sources of image artifacts in the reconstructed image need to be studied. Similarly, the importance of motion compensation while scanning the bale may need to be considered if the stover is to be scanned without temporarily halting the process.

The work in chapter 7 only considered a homogeneous sample. The future study should include a heterogeneous sample and assess the change in behavior of X-ray photon attenuation with an increase in MC or SC or both. The success of the biorefineries relies on accepting different types of feedstocks like other crop residues and forest residues. Different kinds of feedstocks have their complexities that need to be studied to adapt the techniques developed in this dissertation for other types of feedstocks.

REFERENCES

- [1] E. USDo, "Biomass basics: The facts about bioenergy," 2010.
- [2] U. E. I. Administration, "U.S. Energy Facts Explained," <https://www.eia.gov/energyexplained/us-energy-facts/>, [Online; Accessed 14-July-2021].
- [3] U. E. P. Agency, "Carbon pollution from transportation," 2021. [Online]. Available: <https://www.epa.gov/transportation-air-pollution-and-climate-change/carbon-pollution-transportation>
- [4] —, "Greenhouse gas emissions," 2021. [Online]. Available: <https://www.epa.gov/ghgemissions/sources-greenhouse-gas-emissions>
- [5] B. Metz, O. R. Davidson, P. R. Bosch, R. Dave, and L. A. Meyer, "Contribution of working group III to the fourth assessment report of the intergovernmental panel on climate change," 2007.
- [6] Z. Tong, P. Pullammanappallil, and A. A. Teixeira, "How ethanol is made from cellulosic biomass," *EDIS*, vol. 2012, no. 12, 2012.
- [7] O. of ENERGY EFFICIENCY RENEWABLE ENERGY, "Biofuel basics," 2021. [Online]. Available: <https://www.energy.gov/eere/bioenergy/biofuel-basics>
- [8] U. E. I. Administration, "Use of energy explained; energy use for transportation," 2021. [Online]. Available: <https://www.eia.gov/energyexplained/use-of-energy/transportation.php>
- [9] IEA, "Renewables 2019," 2019. [Online]. Available: <https://www.iea.org/reports/renewables-2019>
- [10] E. M. Hernandez and K. S. Ng, "Design of biorefinery systems for conversion of corn stover into biofuels using a biorefinery engineering framework," *Clean Technologies and Environmental Policy*, vol. 20, no. 7, pp. 1501–1514, 2018.

- [11] M. Kumar, Y. Goyal, A. Sarkar, and K. Gayen, "Comparative economic assessment of abe fermentation based on cellulosic and non-cellulosic feedstocks," *Applied Energy*, vol. 93, pp. 193–204, 2012.
- [12] U. E. P. Agency, "Economics of biofuels," 2021. [Online]. Available: <https://www.epa.gov/environmental-economics/economics-biofuels>
- [13] M. H. Langholtz, B. J. Stokes, and L. M. Eaton, "2016 billion-ton report: Advancing domestic resources for a thriving bioeconomy, volume 1: Economic availability of feedstock," *Oak Ridge National Laboratory, Oak Ridge, Tennessee, managed by UT-Battelle, LLC for the US Department of Energy*, vol. 2016, pp. 1–411, 2016.
- [14] C. Li, J. E. Aston, J. A. Lacey, V. S. Thompson, and D. N. Thompson, "Impact of feedstock quality and variation on biochemical and thermochemical conversion," *Renewable and Sustainable Energy Reviews*, vol. 65, pp. 525–536, 2016.
- [15] D. N. Thompson, T. Campbell, B. Bals, T. Runge, F. Teymouri, and L. P. Ovard, "Chemical preconversion: application of low-severity pretreatment chemistries for commoditization of lignocellulosic feedstock," *Biofuels*, vol. 4, no. 3, pp. 323–340, 2013.
- [16] W. W. Wilhelm, J. M. Johnson, D. L. Karlen, and D. T. Lightle, "Corn stover to sustain soil organic carbon further constrains biomass supply," 2007.
- [17] K. Siddiqi and S. Pizer, *Medial representations: mathematics, algorithms and applications*. Springer Science & Business Media, 2008, vol. 37.
- [18] R. R. Kancharla, W. A. Smith, J. L. Klinger, and E. B. Smith, "Anatomical fraction segmentation in the biomass bales," Idaho National Lab (INL), Idaho Falls, ID (United States), Tech. Rep., 2020.
- [19] T. Berchem, O. Roiseux, C. Vanderghem, A. Boisdenghien, G. Foucart, and A. Richel, "Corn stover as feedstock for the production of ethanol: chemical composition of different anatomical fractions and varieties," *Biofuels, Bioproducts and Biorefining*, vol. 11, no. 3, pp. 430–440, 2017.
- [20] R. J. Garlock, S. P. Chundawat, V. Balan, and B. E. Dale, "Optimizing harvest of corn stover fractions based on overall sugar yields following ammonia fiber expansion pretreatment and enzymatic hydrolysis," *Biotechnology for Biofuels*, vol. 2, no. 1, p. 29, 2009.
- [21] Z. Li, H. Zhai, Y. Zhang, and L. Yu, "Cell morphology and chemical characteristics of corn stover fractions," *Industrial Crops and Products*, vol. 37, no. 1, pp. 130–136, 2012.

- [22] K. Duguid, M. Montross, C. Radtke, C. Crofcheck, L. Wendt, and S. Shearer, "Effect of anatomical fractionation on the enzymatic hydrolysis of acid and alkaline pretreated corn stover," *Bioresource technology*, vol. 100, no. 21, pp. 5189–5195, 2009.
- [23] K. L. Kapil Arora, Mark Licht. (2020) Industrial corn stover harvest. Accessed Dec. 06, 2020. [Online]. Available: "<https://store.extension.iastate.edu/product/14073>"
- [24] I. J. Bonner, W. A. Smith, J. J. Einerson, and K. L. Kenney, "Impact of harvest equipment on ash variability of baled corn stover biomass for bioenergy," *BioEnergy research*, vol. 7, no. 3, pp. 845–855, 2014.
- [25] Q. A. Nguyen, "Communication of industry knowledge, best practices, and lessons learned in the space of cellulosic biofuels plant design, project development and execution and operations," Idaho National Lab (INL), Idaho Falls, ID (United States), Tech. Rep., 2020.
- [26] D. W. Templeton, C. J. Scarlata, J. B. Sluiter, and E. J. Wolfrum, "Compositional analysis of lignocellulosic feedstocks. 2. method uncertainties," *Journal of agricultural and food chemistry*, vol. 58, no. 16, pp. 9054–9062, 2010.
- [27] J. B. Sluiter, R. O. Ruiz, C. J. Scarlata, A. D. Sluiter, and D. W. Templeton, "Compositional analysis of lignocellulosic feedstocks. 1. review and description of methods," *Journal of agricultural and food chemistry*, vol. 58, no. 16, pp. 9043–9053, 2010.
- [28] A. Sluiter, B. Hames, R. Ruiz, C. Scarlata, J. Sluiter, D. Templeton, and D. Crocker, "Determination of structural carbohydrates and lignin in biomass," *Laboratory analytical procedure*, no. TP-510-42618, 2010.
- [29] B. R. Hames, S. R. Thomas, A. D. Sluiter, C. J. Roth, and D. W. Templeton, "Rapid biomass analysis," in *Biotechnology for Fuels and Chemicals*. Springer, 2003, pp. 5–16.
- [30] J. D. DeMartini, M. H. Studer, and C. E. Wyman, "Small-scale and automatable high-throughput compositional analysis of biomass," *Biotechnology and bioengineering*, vol. 108, no. 2, pp. 306–312, 2011.
- [31] L. E. Rodriguez-Saona, F. S. Fry, M. A. McLaughlin, and E. M. Calvey, "Rapid analysis of sugars in fruit juices by FT-NIR spectroscopy," *Carbohydrate Research*, vol. 336, no. 1, pp. 63–74, 2001.

- [32] B. Hames, S. Thomas, A. Sluiter, C. Roth, and D. Templeton, "Rapid biomass analysis: New tools for compositional analysis of corn stover feedstocks and process from ethanol production," in *24 th Biotechnology Symposium for Fuels and Chemicals*, 2002.
- [33] P. R. Griffiths and J. A. De Haseth, *Fourier transform infrared spectrometry*. John Wiley & Sons, 2007, vol. 171.
- [34] T. A. Lestander and C. Rhén, "Multivariate NIR spectroscopy models for moisture, ash and calorific content in biofuels using bi-orthogonal partial least squares regression," *Analyst*, vol. 130, no. 8, pp. 1182–1189, 2005.
- [35] P. D. Jensen, H. Hartmann, T. Böhm, M. Temmerman, F. Rabier, and M. Morsing, "Moisture content determination in solid biofuels by dielectric and NIR reflection methods," *Biomass and bioenergy*, vol. 30, no. 11, pp. 935–943, 2006.
- [36] R. Samuelsson, J. Burvall, and R. Jirjis, "Comparison of different methods for the determination of moisture content in biomass," *Biomass and Bioenergy*, vol. 30, no. 11, pp. 929–934, 2006.
- [37] J. Nyström and E. Dahlquist, "Methods for determination of moisture content in woodchips for power plants—a review," *Fuel*, vol. 83, no. 7-8, pp. 773–779, 2004.
- [38] C. Huang, L. Han, X. Liu, and Z. Yang, "Models predicting calorific value of straw from the ash content," *International Journal of Green Energy*, vol. 5, no. 6, pp. 533–539, 2008.
- [39] S. U. Patel, B. J. Kumar, Y. P. Badhe, B. Sharma, S. Saha, S. Biswas, A. Chaudhury, S. S. Tambe, and B. D. Kulkarni, "Estimation of gross calorific value of coals using artificial neural networks," *Fuel*, vol. 86, no. 3, pp. 334–344, 2007.
- [40] C. D. Everard, K. P. McDonnell, and C. C. Fagan, "Prediction of biomass gross calorific values using visible and near infrared spectroscopy," *Biomass and Bioenergy*, vol. 45, pp. 203–211, 2012.
- [41] M. A. Sanderson, F. Agblevor, M. Collins, and D. K. Johnson, "Compositional analysis of biomass feedstocks by near infrared reflectance spectroscopy," *Biomass and bioenergy*, vol. 11, no. 5, pp. 365–370, 1996.
- [42] A. Maier, S. Steidl, V. Christlein, and J. Hornegger, "Medical imaging systems: An introductory guide," 2018.
- [43] A. Biguri, "Iterative reconstruction and motion compensation in computed tomography on GPUs," Ph.D. dissertation, University of Bath, 2018.

- [44] H. K. Tuy, "An inversion formula for cone-beam reconstruction," *SIAM Journal on Applied Mathematics*, vol. 43, no. 3, pp. 546–552, 1983.
- [45] L. A. Flores, V. Vidal, P. Mayo, F. Rodenas, and G. Verdú, "Parallel CT image reconstruction based on GPUs," *Radiation Physics and Chemistry*, vol. 95, pp. 247–250, 2014.
- [46] A. Sobiecki, A. Jalba, and A. Telea, "Comparison of curve and surface skeletonization methods for voxel shapes," *Pattern Recognition Letters*, vol. 47, pp. 147–156, 2014.
- [47] A. Tagliasacchi, T. Delame, M. Spagnuolo, N. Amenta, and A. Telea, "3d skeletons: A state-of-the-art report," in *Computer Graphics Forum*, vol. 35, no. 2. Wiley Online Library, 2016, pp. 573–597.
- [48] H. Blum, *A transformation for extracting new descriptors of shape*. MIT press Cambridge, 1967, vol. 4.
- [49] T. K. Dey and W. Zhao, "Approximate medial axis as a voronoi subcomplex," in *Proceedings of the seventh ACM symposium on Solid modeling and applications*, 2002, pp. 356–366.
- [50] W. H. Hesselink and J. B. Roerdink, "Euclidean skeletons of digital image and volume data in linear time by the integer medial axis transform," *IEEE Transactions on Pattern Analysis and Machine Intelligence*, vol. 30, no. 12, pp. 2204–2217, 2008.
- [51] T.-C. Lee, R. L. Kashyap, and C.-N. Chu, "Building skeleton models via 3-d medial surface axis thinning algorithms," *CVGIP: Graphical Models and Image Processing*, vol. 56, no. 6, pp. 462–478, 1994.
- [52] L. J. Latecki, Q.-n. Li, X. Bai, and W.-y. Liu, "Skeletonization using SSM of the distance transform," in *2007 IEEE International Conference on Image Processing*, vol. 5. IEEE, 2007, pp. V–349.
- [53] C. Xu and J. L. Prince, "Snakes, shapes, and gradient vector flow," *IEEE Transactions on image processing*, vol. 7, no. 3, pp. 359–369, 1998.
- [54] C. McGillivray, C. Hale, and E. H. B. Smith, "Edge noise in document images," in *Proceedings of The Third Workshop on Analytics for Noisy Unstructured Text Data*, 2009, pp. 17–24.
- [55] P. Senin, "Dynamic time warping algorithm review," *Information and Computer Science Department University of Hawaii at Manoa Honolulu, USA*, vol. 855, no. 1-23, p. 40, 2008.

- [56] A. Biguri, M. Dosanjh, S. Hancock, and M. Soleimani, "Tigre: a MATLAB-GPU toolbox for CBCT image reconstruction," *Biomedical Physics & Engineering Express*, vol. 2, no. 5, p. 055010, 2016.
- [57] L. A. Feldkamp, L. C. Davis, and J. W. Kress, "Practical cone-beam algorithm," *Josa a*, vol. 1, no. 6, pp. 612–619, 1984.
- [58] A. H. Andersen and A. C. Kak, "Simultaneous algebraic reconstruction technique (SART): a superior implementation of the art algorithm," *Ultrasonic imaging*, vol. 6, no. 1, pp. 81–94, 1984.
- [59] G. Wang and M. Jiang, "Ordered-subset simultaneous algebraic reconstruction techniques (OS-SART)," *Journal of X-ray Science and Technology*, vol. 12, no. 3, pp. 169–177, 2004.
- [60] Y. Censor and T. Elfving, "Block-iterative algorithms with diagonally scaled oblique projections for the linear feasibility problem," *SIAM Journal on Matrix Analysis and Applications*, vol. 24, no. 1, pp. 40–58, 2002.
- [61] D. F. Swinehart, "The Beer-Lambert law," *Journal of chemical education*, vol. 39, no. 7, p. 333, 1962.
- [62] D. Glassner, J. R. Hettenhaus, and T. M. Schechinger, "Corn stover collection project," in *BioEnergy'98—Expanding Bioenergy Partnerships: Proceedings*, vol. 2. Citeseer, 1998, pp. 1100–1110.
- [63] C.E.Nyquist and R. Stroshine, "Moisture Content Determination and Measuring Techniques," <https://engineering.purdue.edu/~abe305/moisture/html/page1.htm>, [Online; accessed 14-July-2021].
- [64] J. Hubbell and S. Seltzer, "Tables of x-ray mass attenuation coefficients and mass energy-absorption coefficients (version 1.4).[online] available: <http://physics.nist.gov/xaamdi>. national institute of standards and technology, gaithersburg," *Originally published as NISTIR*, vol. 5632, 2004.
- [65] E. TNO, "Phyllis2, database for (treated) biomass, algae, feedstocks for biogas production and biochar," 2020.
- [66] I. A. Krupenikov, B. P. Boincean, and D. Dent, "Soil mineralogy and elemental composition," in *The Black Earth*. Springer, 2011, pp. 27–32.
- [67] W. A. Smith, I. J. Bonner, K. L. Kenney, and L. M. Wendt, "Practical considerations of moisture in baled biomass feedstocks," *Biofuels*, vol. 4, no. 1, pp. 95–110, 2013.

- [68] K. Comer, "Demonstration of an advanced supply chain for lower cost, higher quality biomass feedstock delivery," Project Peer Review, 2019.
- [69] D. Medic, M. Darr, A. Shah, and S. Rahn, "The effects of particle size, different corn stover components, and gas residence time on torrefaction of corn stover," *Energies*, vol. 5, no. 4, pp. 1199–1214, 2012.